Pharmacometric Modeling and Simulation in Special Populations

by

Jingcheng Xiao

A dissertation submitted in partial fulfillment
of the requirements for the degree of
Doctor of Philosophy
(Pharmaceutical Sciences)
in the University of Michigan
2022

Doctoral Committee:

Associate Professor Haojie Zhu, Chair
Assistant Professor Jie Liu
Professor David Smith
Professor Duxin Sun

Jingcheng Xiao

jcxiao@med.umich.edu

ORCID iD: 0000-0003-2502-5493

Dedication

This thesis work is dedicated to my dear parents, Zeping Xiao and Jun Jiang, who have always loved me unconditionally and given me tremendous support. This work is also dedicated to my fiancée, Ruiting Li, who has enlightened my world and always been my best supporter.

Acknowledgements

My first and deepest appreciation goes to my advisor, Dr. Haojie Zhu, this research would not be possible without your mentorship. Your knowledge across multiple disciplines, innovative ideas and optimism in research have greatly helped my graduate studies. You are not only an awesome mentor but also a good friend to work with. You are always kind and patient with every problem we have; you have a high standard for yourself but never push us. You have set the example for me in my life to be a gentle, wise, and optimistic person. Also, I greatly appreciate my dissertation committee members Dr. David Smith, Dr. Jie Liu and Dr. Duxin Sun. Your thoughtful guidance, detailed feedback and encouraging words are very important to me.

It's my great pleasure to be part of the Zhu Lab. I would like to express my sincere gratitude to Dr. Jian Shi, Dr. Xinwen Wang and Dr. Bing He for your great help and guidance in my research. Thank you, Dr. Lucy Her, Jiapeng Li, Dr. Logan Smith, Sunny Jung and Jingting Wang for helping me with experiments and sharing everyday lives with me.

Many thanks to my wonderful mentors and teachers: Dr. Peng Zou, Dr. Brian Maas, Dr. Jingxian Chen, Dr. Varsha Mehta, Dr. Tao Zhang and Dr. Guohua An, the knowledge you taught me tremendously inspired my research and broadened my horizon.

Thank you to my friends and colleagues: Richard Schutzman, Jennifer Diaz, Pornnoppadol Ghasidit, Xiao Liu, Marisa Aikins, Minzhi Yu, Dr. Hongxiang Hu, Dr. Xiaoqi Sun, Dr. Lu Zhang, Dr Yucheng Fan, Dr. Brian Thompson, Dr. Kai Wang, Dr. Katie Cavanagh, graduate school would have been unbearable without you, and I will cherish all the happy memory we had together. Special thanks go to my friends in the DOTA2 guild "Solid", who

have emotionally supported me through the dark moment during COVID, even though I will probably finish this dissertation earlier without you guys.

Last, but not least, my warm and heartfelt thanks go to my family for their love and support.

Table of Contents

Dedication ii

Acknowledgements iii

List of Tables ix

List of Figures xi

Abstract xiv

Chapter 1 Introduction 1

Chapter 2 Physiologically-Based Pharmacokinetic Modeling to Predict Methylphenidate Exposure Affected by Interplay Among Carboxylesterase 1 Pharmacogenetics, Drug-Drug Interactions, and Sex 4

2.1 Abstract 4

2.2 Introduction 5

2.3 Methods 7

2.3.1 Materials 7

2.3.2 Genotyping 8

2.3.3 dl-MPH Hydrolysis in Human Liver S9 Fractions (HLS9) 8

2.3.4 LC-MS/MS Assay 9

2.3.5 MPH PBPK Model Development and Simulation 10

2.3.6 Model performance evaluation 15

2.4 Results 15

2.4.1 The CES1 G143E Variant Impaired MPH Hydrolysis in the Human Liver 15

2.4.2 Performance of the PBPK Models for Predicting MPH Exposure in a Healthy Adult Population 16

2.4.3 Simulation of d-MPH Exposure in G143E Heterozygotes 18

2.4.4 MPH-ethanol DDI Prediction 20

2.4.5 Simulation of Sex Difference in d-MPH Exposure 20

2.4.6 Prediction of MPH-ethanol DDI in Different Sex 21

2.4.7 Simulation of the Effect on d-MPH PK of Interplay Among the G143E Variant, DDI, and Sex 21

2.5 Discussion 22

Chapter 3 Developing a SWATH Capillary LC-MS/MS Method for Simultaneous Therapeutic Drug Monitoring and Untargeted Metabolomics Analysis of Neonatal Plasma 26

3.1 Abstract 26

3.2 Introduction 27

3.3 Materials and Methods 29

3.3.1 Chemicals and materials 29

3.3.2 Calibrators and quality control (QC) samples 29

3.3.3 Sample preparation 31

3.3.4 SWATH data acquisition 31

3.3.5 Method validation 32

3.3.6 Data processing and statistical analysis 34

3.4 Results 36

3.4.1 Method validation 36

3.4.2 Untargeted metabolomics analysis 42

3.4.3 Application to clinical samples 44

3.5 Discussion 49

Chapter 4 Population PK/PD Study of Midazolam in the Neonatal Intensive Care Unit Patients 52

4.1 Abstract 52

4.2 Introduction 52

4.3 Materials and Methods 54
4.3.1 Patient and study designs 54
4.3.2 Midazolam and its metabolites concentration measurements 55
4.3.3 Midazolam PD response assessment 55
4.3.4 Data set 55
4.3.5 Population PK/PD model development 56
4.3.6 Covariates analysis 57
4.3.7 Model validation 58
4.4 Results 58
4.4.1 Study population 58
4.4.2 Population PK modeling 59
4.4.3 Population PD modeling 65
4.4.4 Model evaluation 66
4.5 Discussions 66
Chapter 5 Machine Learning Assisted Population PD Study of Midazolam in Neonatal Patients 71
5.1 Abstract 71
5.2 Introduction 71
5.3 Materials and Methods 74
5.3.1 Patients 74
5.3.2 Data processing 74
5.3.3 Model building 76
5.3.4 Model evaluation 77
5.4 Results 77
5.4.1 K Nearest Neighbor (KNN) classifier 77
5.4.2 Support vector machine (SVM) classifier 80

5.4.3 Decision Tree (DT) Classifier 81
5.4.4 Random Forest (RF) classifier..... 83
5.4.5 Naïve Bayes (NB) classifier 85
5.4.6 Neural Network (NN) Classifier 87
5.5 Discussion 88
Chapter 6 Conclusions and Future Directions 91
Bibliography 94

List of Tables

Table 2-1 Demographics of 102 human liver S9 samples 7

Table 2-2 Demographics of subjects in the clinical studies utilized for model verification..... 11

Table 2-3 Physicochemical and in vitro/in vivo parameters for d-MPH PBPK modeling..... 12

Table 2-4 PBPK model parameters of ethanol[3] 14

Table 2-5 Cmax and AUC of the observed and predicted d-MPH PK..... 18

Table 2-6 Fold changes of the observed and predicted d-MPH PK in different groups compared with control groups[a] 19

Table 3-1 Ionization parameters and retention times of the analytes and the internal standards . 30

Table 3-2 Analyte concentrations in the quality control samples..... 30

Table 3-3 Performance of calibration curves, LLOQ, LLOD, and typical plasma concentration ranges of the targeted compounds..... 30

Table 3-4 MS-DIAL software parameters used for untargeted metabolomics analysis..... 35

Table 3-5 Intra-batch precision and accuracy..... 40

Table 3-6 Inter-batch precision and accuracy..... 41

Table 3-7 Freeze and thaw stability, matrix effect, and extraction recovery..... 41

Table 3-8 Autosampler stability..... 41

Table 3-9 Concentrations of targeted drugs (ng/ml) measured in neonate plasma samples..... 45

Table 4-1 Demographic information of neonate patients 59

Table 4-2 Stepwise process of MDZ PK model development..... 62

Table 4-3 Parameter estimation of the MDZ population PK model..... 62

Table 4-4 Estimated PK parameters compared with other published models [116-119] 66

Table 5-1 Means and standard deviations of all numerical variables..... 74

Table 5-2 Neonatal Pain, Agitation, and Sedation Scale (N-PASS) [139]..... 76

List of Figures

Figure 2-1 Workflow of the d-MPH PBPK model development, qualification, and application.10

Figure 2-2 Effect of the CES1 genetic polymorphism G143E on MPH metabolism (hydrolysis) rate in 102 human liver S9 samples. The samples were categorized into two genotypes: G143E (rs71647871) heterozygote (G/A) and wild type (G/G). Horizontal bars indicate mean values in each group. Mann–Whitney U-test was utilized to test the differences in CES1 activity between the two genotypes. 16

Figure 2-3 Simulated and observed plasma concentration-time profiles of d-MPH in different populations, including (A) a single oral dose of 0.3 mg/kg dl-MPH (i.e., 0.15 mg/kg d-MPH) and 10 mg dl-MPH (i.e., 5 mg d-MPH) in healthy adult populations; (B) a single oral dose of 10mg dl-MPH in healthy adult CES1-G143E carriers and non-carriers; (C) a single oral dose of 0.3 mg/kg dl-MPH co-administrated with a single dose of 0.6 g/kg ethanol 0.5 hours after MPH dosing or additional does of ethanol (0.6 g/kg) every 6 hours in a healthy adult population; (D) a single oral dose of 0.3 mg/kg MPH in healthy males and females, in which simulations were conducted in a virtual female population with hepatic CES1 expression 20% higher than males; (E) a single oral dose of 0.6 g/kg ethanol was given 0.5 hours after oral administration of 0.3 mg/kg MPH in different sex, in which hepatic CES1 expression was set as 20% higher in females than males during the simulations; (F) Simulations of virtual male G143E subjects who received a single oral dose of 0.3 mg/kg dl-MPH and 0.6 g/kg ethanol 0.5 hours after the administration of MPH. The observed data were obtained from two MPH clinical studies[20, 22]. The colored shadow areas represent the 5th and 95th percentiles of the predicted mean values. The filled circles are observed mean values from the clinical study, and the solid lines represent the predicted mean plasma d-MPH concentrations. 17

Figure 3-1 Workflow of the SWATH capillary LC-MS/MS method for simultaneous therapeutic drug monitoring and untargeted metabolomics analysis 35

Figure 3-2 MS1 and selected MS2 chromatograms of the targeted analytes obtained from neonate samples 38

Figure 3-3 MS1 and selected MS2 chromatograms of the targeted analytes obtained from blank plasma spiked with the analytes at the concentrations of LLOQ..... 39

Figure 3-4 MS1 and MS2 chromatograms of the targeted analytes in the blank plasma 40

Figure 3-5 Distribution of the MS1 ion intensity of the annotated metabolites 43

Figure 3-6 Profiles of the untargeted metabolomic analysis method. (A) Classification and relative abundance of the annotated metabolites (B) Example of identified metabolites phenylalanine, left panel: overlapped MS1 and MS2 peaks; right panel: deconvoluted MS/MS spectrum from the plasma samples (blue) matched against database spectrum (red). (C) Example of identified metabolites LPC 18:0, left panel: overlapped MS1 and MS2 peaks; right panel: deconvoluted MS/MS spectrum from the plasma samples (blue) matched against database spectrum (red). (D) Distribution of RSD (%) of all the features in QC samples. The percentage of compound numbers within the corresponding %RSD range is represented by each column. 43

Figure 3-7 PCA score plot of the metabolic profiles of the QC and neonatal plasma samples. Black triangles represent four QC samples and red squares are the six neonatal samples 44

Figure 3-8 Metabolomics profiles of neonate samples. (A) PLS-DA score plot of the full-term and preterm neonates. Red dots represent the three full-term neonates, and blue triangles represent the three preterm neonates. (B) S-plot plot of the PLS-DA model. The variables that contributed most to the classification were in shaded areas. (C) Venn diagram of VIP (VIP>1, n=175), P-value ($P < 0.05$, $n = 106$), and fold change ($FC < 0.8$ or $FC > 1.2$, $n = 622$). (D) Heatmap of 19 potential differential metabolites between preterm and termed groups. 47

Figure 3-9 Loading plot of the PLS-DA model. The variables contributed most to the classification were in the shaded areas. 47

Figure 3-10 Violin plot of the 19 annotated plasma metabolites that differed between the preterm and termed neonates. Red circles are preterm subjects and blue triangles are termed subjects. The X axis is the normalized concentration level. 48

Figure 4-1 Schematic representation of the MDZ and metabolites structural model 60

Figure 4-2 Heatmap of correlations between potential covariates of the MDZ PK/PD model 61

Figure 4-3 Goodness-of-fit plots of MDZ observed data and model prediction The dashed line is the locally weighted scatterplot smoothing..... 63

Figure 4-4 Goodness-of-fit plots of 1-OH-MDZ observed data and model prediction The dashed line is the locally weighted scatterplot smoothing. 64

Figure 4-5 Goodness-of-fit plots of 4-OH-MDZ observed data and model prediction. The dashed line is the locally weighted scatterplot smoothing 65

Figure 4-6 Observed concentration of 4-OH-MDZ and 1-OH-MDZ.The Y-axis shows the concentration ratios of 4-OH-MDZ to 1-OH-MDZ, and the X-axis represents the postnatal ages of the patients. 68

Figure 5-1 Precision-Recall Curve of KNN classifier 78

Figure 5-2 Receiver Operating Characteristic Curve of KNN classifier 79

Figure 5-3 Permutation feature importance of KNN classifier 79

Figure 5-4 Precision-Recall Curve of SVM classifier 80
Figure 5-5 Receiver Operating Characteristic Curve of SVM classifier 81
Figure 5-6 Precision-Recall Curve of DT classifier 82
Figure 5-7 Receiver Operating Characteristic Curve of DT classifier 82
Figure 5-8 Precision-Recall Curve of RF classifier 84
Figure 5-9 Receiver Operating Characteristic Curve of RF classifier 84
Figure 5-10 Permutation feature importance of RF classifier 85
Figure 5-11 Precision-Recall Curve of NB classifier 86
Figure 5-12 Receiver Operating Characteristic Curve of NB classifier 86
Figure 5-13 Precision-Recall Curve of NN classifier 87
Figure 5-14 Receiver Operating Characteristic Curve of NN classifier 88

Abstract

Pharmacometrics modeling encompasses both pharmacokinetics (PK) and pharmacodynamics (PD) data to quantitatively describe the dose-exposure-response relationship. Pharmacometrics is widely utilized to facilitate drug development and optimize pharmacotherapy regimens in the clinic. Pharmacometrics approaches include the "top-down" population PK/PD modeling and "bottom-up" physiologically based pharmacokinetic (PBPK) modeling. Moreover, artificial intelligence (i.e., machine learning) has proven a powerful tool for pharmacometrics modeling. Pharmacometrics modeling and simulation are particularly useful in studying PK/PD in special populations, such as pediatrics and newborns, because of the practical and ethical challenges in performing conventional clinical trials in these special patient populations.

The first project of this dissertation research is to develop PBPK models to evaluate how altered carboxylesterase 1 (CES1) function could affect the exposure of methylphenidate (MPH). Various clinical scenarios that affect CES1 function, including different CES1 genotypes, drug-alcohol interactions, and different sex, were simulated regarding their impact on MPH PK. The models successfully predicted the exposure alteration of MPH caused by the G143E genetic variant, the ethanol-MPH drug-drug interaction, and sex. The study suggests that male G143E carriers who are alcohol consumers are at a higher risk of MPH overexposure.

Another commonly used pharmacometric method is population PK/PD modeling. The second project was to build a population PK/PD model to describe the PK and PD of midazolam (MDZ) in neonates treated at the Neonatal Intensive Care Unit (NICU). We developed a capillary LC-MS/MS metabolomics method using a SWATH-based data-independent acquisition

strategy for simultaneous targeted and untargeted metabolomics analysis of neonatal plasma samples. The method was successfully utilized to determine the global plasma metabolomics profiles and quantify the plasma concentrations of five drugs commonly used in NICU, including ampicillin, caffeine, fluconazole, vancomycin, and midazolam and its active metabolites. To describe MDZ PK/PD profiles, we developed a two-compartment population PK model for MDZ and its two metabolites, 1-hydroxymidazolam(1-OH-MDZ) and 4-hydroxymidazolam(4-OH-MDZ). Bodyweight, creatinine, and alanine transaminase (ALT) levels were incorporated into the population PK model as covariates to explain the interindividual variability. The prediction of MDZ, 1-OH-MDZ, and 4-OH-MDZ PK profiles by our model matched well with the observed clinical data via the visual prediction check of goodness-of-fit plots. A binary probability model was used as the PD model. No significant correlation was observed between MDZ PK and PD profiles.

Since the classic population PK/PD model had difficulty describing MDZ PD response in neonates, we further developed machine learning-based models to reveal the exposure-response relationship. We assessed six machine learning models (K Nearest Neighbor, Support Vector Machine, Decision Tree, Random Forest, Naïve Bayes, and Neural Network). Models were tested with a training dataset, and the final prediction performance of each model was evaluated using a testing dataset. The random forest classifier had the best prediction performance of the PD response for our current dataset, with the accuracy = 0.83, precision = 0.98, and area under the receiver operating characteristic curve = 0.81. Postmenstrual age, birth weight, and dosing weight were the top three most important features for the random forest classifier.

Chapter 1 Introduction

Pharmacometrics is defined as the science that quantifies drug, disease, and trial information to aid efficient drug development and regulatory decisions [1]. Pharmacometrics involves the analysis and interpretation of data produced in pre-clinical and clinical trials. Mathematical models are usually applied in pharmacometrics studies to describe the relationship between drug exposure and response. Different pharmacometrics models are chosen to fulfill different purposes. For example, population PK/PD modeling is a top-down approach aiming to obtain the system characteristics and population parameter estimation with the observed data. In contrast, the systems biology "bottom-up" approach (e.g., the physiologically based pharmacokinetic (PBPK) model) requires in-depth mechanistic knowledge of the system and allows integrating molecular level information at a cellular, tissue, or whole-body level to understand drug PK/PD from a mechanism perspective [2].

Drug metabolism is the in vivo metabolic breakdown of xenobiotics, usually through specialized enzymes. There are two phases of drug metabolism: DMEs like cytochrome P450 (CYP450) oxidases introduce polar or reactive groups into drugs during phase I metabolism, then in phase II these modified xenobiotics are conjugated to polar compounds by transferase enzymes, such as glutathione S-transferase, arylsulfatase and UDP-glucuronyl transferase [3]. Carboxylesterase 1 (CES1) is a major phase I DME, responsible for 80-95% of total hydrolytic activity in the liver [4]. CES1 is substrate-selective towards carboxyl esters with a large ethyl group and a small alcohol group [5] and metabolizes a wide range of substrates, including many clinically significant medications, environmental pollutants, and endogenous compounds. CES1

not only metabolizes an active drug into its inactive metabolites but can also activate prodrugs to their active forms by deesterification. In humans, CES1 is highly expressed in the liver and less abundant in other organs. The activity and expression of CES1 vary significantly among individuals/populations; many factors, including genotypes, sex, age, and inhibitors, could contribute to the interindividual variability in CES1 function. Here, we used a PBPK modeling approach to study the mechanism of CES1 inter-population differences and how these affect the CES1 substrate MPH exposure quantitatively.

The neonatal population is very different from other populations considering their fast changes in body size and composition, rapid maturation of physiologic processes, and unique disease status. It is challenging to study the drug PK/PD profiles in infants [6]. Due to the limited blood volume in neonates, conducting traditional rich-blood-sampling PK/PD studies in neonates is difficult; only sparse and unbalanced PK/PD data could be acquired from neonates. Also, the interindividual and intraindividual variability in drug exposure and response is extensive because of the fast growth and dynamic maturation changes in neonates [7, 8].
Population-based pharmacometrics modeling is a promising approach to overcome these barriers [9]. It can predict the PK/PD profiles at the population level while still considering the differences between individuals. Sparse and unbalanced data from this special population could be analyzed by population-based pharmacometrics modeling as long as the total sample size is adequate. In addition, different covariates could be incorporated into the basic population model to evaluate the influence of developmental changes on PK and PD in neonates.

In this project, we developed PBPK models to study the MPH exposure changes caused by the alteration of CES1 function. We also developed population PK/PD models and the

machine learning-based pharmacometrics models to investigate MDZ PK and PD in neonatal patients.

Chapter 2 Physiologically-Based Pharmacokinetic Modeling to Predict Methylphenidate Exposure Affected by Interplay Among Carboxylesterase 1 Pharmacogenetics, Drug-Drug Interactions, and Sex

2.1 Abstract

The pharmacokinetics (PK) of methylphenidate (MPH) differ significantly among individuals. Carboxylesterase 1 (CES1) is the primary enzyme metabolizing MPH, and its function is affected by genetic variants, drug-drug interaction (DDI), and sex. The object of this study is to evaluate CES1 pharmacogenetics as related to MPH metabolism using human liver samples and develop a physiologically-based pharmacokinetic (PBPK) modeling approach to investigate the influence of CES1 genotypes and other factors on MPH PK. The effect of the CES1 variant G143E (rs71647871) on MPH metabolism was studied utilizing 102 individual human liver S9 (HLS9) fraction samples. PBPK models were developed using the population-based PBPK software PK-Sim® by incorporating the HLS9 incubation data. The established models were applied to simulate MPH PK profiles under various clinical scenarios, including different genotypes, drug-alcohol interactions, and the difference between males and females. The HLS9 incubation study showed that subjects heterozygous for the CES1 variant G143E metabolized MPH at a rate of approximately 50% of that in non-carriers. The developed PBPK models successfully predicted the exposure alteration of MPH from the G143E genetic variant, ethanol-MPH DDI, and sex. Importantly, the study suggests that male G143E carriers who are alcohol consumers are at a higher risk of MPH overexposure. PBPK modeling provides a means

for better understanding the mechanisms underlying interindividual variability in MPH PK and PD and could be utilized to develop a safer and more effective MPH pharmacotherapy regimen.

2.2 Introduction

Attention-deficit/hyperactivity disorder (ADHD) is a chronic neurobiological behavioral disorder [10] that affects approximately 5-10% of children worldwide. Many ADHD patients exhibit continued symptoms into adulthood [11]. Methylphenidate (MPH) blocks the reuptake of dopamine and norepinephrine into presynaptic neurons [12, 13] and is the most commonly prescribed medication for ADHD treatment [14].

Most MPH products on the market are a racemic mixture consisting of equal amounts of the d- and l-enantiomers [15]. Since d-MPH is far more pharmacologically potent than l-MPH, plasma d-MPH is often used to represent MPH pharmacokinetics (PK) [16]. Both d- and l-MPH are exclusively metabolized (via de-esterification) by carboxylesterase 1 (CES1) to form the pharmacologically inactive metabolite, ritalinic acid [17]. Due to the extensive first-pass effect, the absolute oral bioavailability of MPH is low [18]; and over 80% of orally administrated dl-MPH is excreted as ritalinic acid in urine [19].

CES1 is the most abundant hydrolase in the human liver, contributing around 90% of hepatic hydrolytic activity; in addition to metabolizing MPH, it plays an essential role in hydrolyzing many other ester- and amide-containing drugs, xenobiotics, and endogenous compounds [20]. CES1 expression and activity vary markedly among individuals, resulting in interindividual variability in the PK and pharmacodynamics (PD) of medications metabolized by CES1 [5]. The interindividual difference in CES1 activity and expression is partially due to genetic variants. For example, the CES1 nonsynonymous single nucleotide polymorphism (SNP) G143E (rs71647871) is reported as a loss-of-function variant that significantly alters the PK of

MPH [21, 22] and several other medications metabolized by CES1 [23, 24]. Moreover, CES1 activity can be significantly impaired by CES1 inhibitors [5, 25]. While many drugs have been identified as potential CES1 inhibitors in vitro, ethanol is the only inhibitor with a demonstrated effect on MPH PK in human subjects [18, 26]. The use of recreational MPH together with drinking has raised a safety concern, especially on college campuses [27]. In addition to genetic variants and drug-drug interaction (DDI), sex is another factor contributing to the variability in CES1 function. A proteomics study revealed that hepatic CES1 protein expression was about 20% higher in females than in males [28]. Consistent with the finding, MPH exposures were found to be greater in males than females [29, 30]. Although the effects of genetic variation, DDI, and sex on MPH PK have been reported individually, the combined effects of the different factors and the magnitude of those effects have not been assessed.

Physiologically-based pharmacokinetic (PBPK) modeling is a mechanistic approach to predict PK by integrating organism- and drug-dependent properties [31]. One of the advantages of PBPK modeling is its capability to extrapolate PK by incorporating various factors under different clinical scenarios. PBPK models are well recognized by the US Food and Drug Administration (FDA) and European Medicines Agency (EMA) for predicting DDI risk [32]. In the present study, we conducted the genotyping and enzyme activity analysis of CES1 in over a hundred human liver samples and developed PBPK models to evaluate the impact of CES1 genetic variation, DDI, and sex on MPH PK.

2.3 Methods

2.3.1 Materials

dl-MPH, the internal standard d3-dl-MPH (methyl labeled), ritalinic acid, LC–MS grade methanol, acetonitrile, and formic acid were all purchased from Sigma–Aldrich (St. Louis, MO). One M 4-(2-hydroxyethyl)-1-piperazineethanesulfonic acid (HEPES) was purchased from Life Technologies (Carlsbad, CA). All other chemicals and reagents were of analytical grade and commercially available.

A total of 102 human liver samples were obtained from the Cooperative Human Tissue Network (Columbus, OH, USA) and the XenoTech LLC (Kansas City, KS, USA). The donors consisted of 46 males and 56 females with ages ranging from 1 to 83 years old. The racial distribution is as follows: ninety-four Caucasians, five African Americans, one Hispanic, and two classified as "unknown" or "others". The detailed demographic information of the liver donors was provided in Table 2-1.

Table 2-1 Demographics of 102 human liver S9 samples

	CES1 healthy subject	**G143E mutant**
Subject Number (n=)	97	5
Age (years old)	56.3 ± 16.7	65.3 ± 9.3
Gender (%Male)	44.3	60
Race	89 Caucasians 5 African American 1 Hispanic 2 Unknown	5 Caucasians

2.3.2 Genotyping

Genomic DNA was extracted from the human liver samples using the PureLink® Genomic DNA Mini Kit (Life Technologies), following the manufacturer's instructions. Samples were genotyped for the CES1 genetic polymorphism G143E (rs71647871) using the method described in our previous publication [33, 34]. The G143E is a well-established CES1 loss-of-function variant for which a significant effect on MPH PK has been demonstrated.

2.3.3 dl-MPH Hydrolysis in Human Liver S9 Fractions (HLS9)

The dl-MPH hydrolysis study was carried out in 1.5 ml tubes at a total volume of 80 µl. HLS9 samples were prepared according to a previously reported method [33]. Heat-inactivated HLS9 (100 °C for 5 min) was utilized as the negative control. CES1-mediated dl-MPH hydrolysis rates were calculated by subtracting the rate of ritalinic acid formation in the negative control from that in the HLS9 samples. The formation rates were linear with HLS9 protein concentrations (0.2 - 1.0 mg/ml) and incubation times (2–12 hours). dl-MPH working solution was freshly prepared in PBS supplemented with 20 mM HEPES. The reaction was initiated by mixing 40 µl of dl-MPH solution with 40 µl of HLS9; final concentrations of dl-MPH and HLS9 were 50 µM and 0.5 mg protein/ml, respectively. After incubation at 37 °C for 5 hours, the reaction was terminated by the addition of 240 µl of methanol containing 2 nM of the internal standard d3-MPH. The mixture was vortexed for 5 min and centrifuged at 17,000 g for 10 min to remove precipitated proteins. Supernatants were collected and analyzed using the LC-MS/MS assay described below. To compare the CES1 hydrolysis activity between different groups with and without the G143E variant (rs71647871), a Mann–Whitney U-test was performed, and a P value less than 0.05 was considered statistically significant.

2.3.4 LC-MS/MS Assay

LC–MS/MS analysis was performed on a Shimadzu HPLC system (Shimadzu, Tokyo, Japan) coupled with an Applied Biosystems API 4000 triple quadrupole mass spectrometer (Foster City, CA, USA). The assay was performed as previously described with some modifications [35]. The analytes were separated on a Shimadzu VP-ODS column (5 µm, 150 × 2.0 mm, Shimadzu, Japan). The mobile phase consisted of water with 0.02% formic acid (v/v) (phase A) and acetonitrile containing 0.02% formic acid (v/v) (phase B), and was delivered at a flow rate of 0.2 ml/min. A 10.5 min gradient elution was utilized for the separation with the time program set as follows: from 0 to 7 min, phase B was increased from 2% to 70%, then returned to 2% at 8 min, and maintained until the end of the gradient. The MS was operated in a positive ion mode using turbo electrospray ionization. The following parameters were applied: curtain gas: 25 psi; gas 1: 50 psi; gas 2: 50 psi; ionspray voltage: 5500 V; source temperature: 500 °C; entrance potential: 10 V; dwell time: 50 ms; collision cell exit potential: 15 V; declustering potential: 50 V; and collision energy: 30 V for d3-MPH, 35V for ritalinic acid. The following transitions were monitored in the Multiple Reaction Monitoring (MRM) mode: d3-MPH: m/z 237.4 > 84.5; ritalinic acid: m/z 220.5 > 84.6. Quantifications were based on the peak area ratios of ritalinic acid to d3-MPH. The calibration curves were found to have regression coefficients greater than 0.99. Three quality controls representing low, medium, and high concentrations of ritalinic acid (0.1, 1, and 5 µM) were included in every batch of the experiment. The accuracy and precision of the assay met the requirement in the FDA bioanalytical method validation guidance.

2.3.5 MPH PBPK Model Development and Simulation

The workflow of the model development, qualification, optimization, and application was summarized in Figure 2-1.

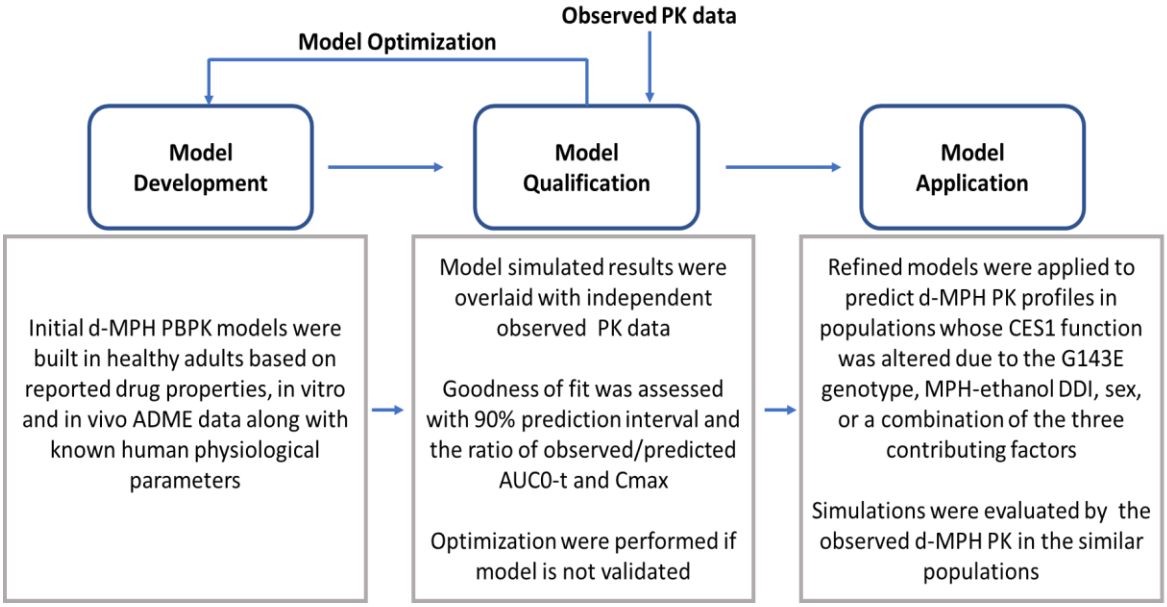

Figure 2-1 Workflow of the d-MPH PBPK model development, qualification, and application.

MPH Base Model Development

d-MPH PBPK models were constructed using the population-based PBPK software PK-Sim® (Open Systems Pharmacology Suite, Version 9.0). All population simulations were carried out using 100 subjects. The default population was the PK-Sim® built-in European (Caucasian) healthy adult male. The G143E heterozygote population was created by reducing CES1 activity by 50% and keeping CES1 expression level unchanged to reflect the change of CES1 function in G143E heterozygotes [36]. Sex and age distributions in the simulated populations were set to match the demographics reported in the MPH clinical studies. Specifically, for the CES1 G143E mutation simulation, a virtual Caucasian population with 50% male and age from 21-29 years

old was used to simulate the study subject population used in the Stage's study [22] ; for other simulation studies, a virtual Caucasian population with ages from 21-42 years old, 50% male, and mean body weight of 82.2 ± 11.1 kg for males and 59.6 ± 6.8 kg for females was created to match the Patrick's study [20]. The demographic information of the two studies was summarized in Table 2-2. PK-Sim built-in inter-individual variability was applied to other demographic parameters of the population.

Table 2-2 Demographics of subjects in the clinical studies utilized for model verification

Reference	**Patrick et.al[20]**		**Stage et.al[22]**	
Gender/ Group	Male	Female	Control	G143E
Subject Number (n=)	12	12	16 (50% Male)	6 (50% Male)
Age (years old)	25.8 ± 2.4	26.9 ± 4.5	24 (21-29)	23 (22-28)
Bodyweight (kg)	82.2 ± 11.1	59.6 ± 6.8	66.5	69
Race	Caucasians	11 Caucasians 1 Asian	Caucasians	Caucasians

The drug-dependent properties of MPH are shown in Table 2-3. A first-order kinetic model without lag time was used to describe MPH absorption. A minimal PBPK model without a single adjusting compartment was used to describe disposition. The total volume of distribution at steady state (Vss) was adopted from the FDA label (Ritalin, FDA Label, 2019). For each tissue, a blood flow-limited distribution model [37] was applied since MPH is quickly equilibrated between systemic circulation and tissues [38]. The partition coefficient of d-MPH in different tissues was calculated by the PK-Sim standard estimation method based on the MPH

lipophilicity, fraction unbound in plasma, and volume fraction of water, lipid, and protein. As reported by Golub et al. [39], about 80% of MPH is hydrolyzed by CES1, and the remaining is metabolized by oxidation. CES1-mediated MPH metabolism was described by Michaelis–Menten kinetics. V_{max} and K_m values were obtained from an in vitro incubation study using recombinant CES1 enzyme [40]. The hepatic CES1 protein levels were estimated based on the reported CES1 protein concentrations in human liver S9 [41], liver S9 protein concentrations per gram of liver tissue [42] with the following equation:

Human hepatic CES1 protein level (pmole/g liver) = Human liver S9 CES1 protein concentration (pmole/mg S9) * liver S9 protein concentration (mg/g liver)

The remaining 20% of MPH was cleared through the oxidation pathway, and the clearance value for MPH oxidation was obtained from literature [37]. The final d-MPH ADME parameters used in the model are listed in Table 2-3.

Table 2-3 Physicochemical and in vitro/in vivo parameters for d-MPH PBPK modeling

Parameters	Value	Sources and Comments
Molecular weight	233.3	[34]
Log Po:w	2.31	[43]
PKa	9.51	[43]
Fraction unbound	0.8	FDA Label-Ritalin (2019)
Absorption model	First-order	[44, 45]
$P_{eff,man}$	0.963×10^{-4} cm/s	[34]Derived based on Papp
Partition Coefficient (richly)	5.66	[44]
Partition Coefficient (slowly)	2.47	[43]
Vss	2.65 ± 1.11 L/kg	FDA Label- Ritalin (2019)
B/P ratio	1.75	Health Canada - Ritalin
V_{max}	3.2 nM/min/mg	[40]recombinant human CES1A1 enzyme
K_m	89.9 µM	[40]recombinant human CES1A1 enzyme
Hepatic CES1 concentration	22.9 µM	[41]
Human liver S9 CES1 concentrations	205.3 pmol/mg protein	[41]
Hepatic oxidation	0.7 L/h/kg	[43]
K_i of Ethanol competitive inhibition on CES1	23 mM	[29, 46]

LogPo:w : logarithm of the n-octanol:buffer partition coefficient,

PKa: logarithmic constant of acid dissociation constant

$P_{eff, man}$ effective permeability in man

Vss: volume of distribution at steady states

B/P ratio: Blood to plasma ratio

V_{max}: maximum rate of reaction

K_m: Michaelis-Menten Constant

K_i: concentration of inhibitor that support half maximum inhibition

Simulation of MPH PK affected by G143E variant, MPH-ethanol DDI, different sex, and the interplay among those factors

We ran simulations for the G143E heterozygote population and the population without the variant. The G143E variant has a very low frequency (2-4%); thus, simulations were only conducted in the heterozygote population. The in vitro HLS9 incubation study showed that the average CES1 activity for metabolizing MPH in the G143E heterozygous HLS9 samples was approximately 50% of that in those without the variant. This is consistent with previous observations that G143E was a loss-of-function variant for the metabolism of CES1 substrates [21]. A virtual European healthy adult population including both males and females (1:1) with a 50% reduction of hepatic CES1 activity was created to represent G143E heterozygotes. This population was then used to develop the MPH basic PBPK model for simulation.

New compound ethanol was built for the simulation of MPH-Ethanol DDI, the physicochemical parameters of ethanol used in PBPK model were listed in Table 2-4: molecular weight = 46, pKa = 15.9 [47], faction unbound in plasma = 1.0 [46], human blood : plasma ratio = 0.81 [48], cellular permeability = 245000(nm/s) [46], in vitro metabolic clearance Vmax = 2 (mmol/min/L) [49], Km = 1 (mmol/L) [49]. A competitive inhibition DDI model was used to

describe the inhibitory effect of ethanol on d-MPH metabolism. The inhibition constant (Ki) of ethanol CES1 was from another PBPK study of the DDI between ethanol and CES1 substrate [46]. This ethanol PBPK model was verified by the clinical data from previous research [46]. For the MPH-ethanol DDI prediction model, a single dose of ethanol 0.6 g/kg was administered 0.5 hour after MPH dosing. We also simulated a multiple-dose scenario, in which ethanol (0.6 g/kg) was given every 6 hours after the first ethanol dose (0.5 hours after MPH dosing).

Table 2-4 PBPK model parameters of ethanol[3]

Parameters	Value
Molecular weight	46
Log D at pH 7.4	-0.31
PKa	15.9
Model type	Whole-body PBPK
Dissolution	dissolved
Fraction unbound in plasma	1
B/P ratio	0.81
Cellular (organ) permeability (nm/s)	245000
Intestinal permeability (nm/s)	42.7
V_{max}(mmol/min/L)	2.0
K_m(mmol/ L)	1.0
K_i competitive inhibition on CES1(mmol/L)	23

PKa: logarithmic constant of acid dissociation constant

B/P ratio: Blood to plasma ratio

Vmax: maximum rate of reaction

Km: Michaelis-Menten Constant

Ki: concentration of inhibitor that support half maximum inhibition

Our liver proteomics study demonstrated that hepatic CES1 protein expression in females was approximately 20% higher than that in males [28]. Therefore, a virtual European healthy

adult female population was created with the hepatic CES1 protein level set at 120% of that in healthy European males.

To study the effects of the interplay among the G143E variant, MPH-ethanol DDI, and sex on MPH PK, the PK profile of 0.15 mg/kg MPH in male G143E heterozygotes who ingested 0.6 g/kg ethanol was simulated. In this population, CES1 activity was decreased by 50% due to the G143E genotype, CES1 expression was 20% lower than adult healthy females, and the inhibitory effect of 0.6 g/kg ethanol administration on CES1 was applied.

2.3.6 Model performance evaluation

The model performances were evaluated by both visual predictive checks and the ratios of the observed to predicted values of C_{max} and AUC_{0-t}. For visual predictive checks, the observed data were overlaid with the 90% confidence interval of prediction. If observed plasma concentration-time profiles fell within the 5^{th} to 95^{th} percentiles of the simulated mean plasma concentration curves, the prediction performance was considered acceptable [50]. In addition, the model was deemed acceptable if the observed/predicted ratios of C_{max} and AUC_{0-t} were within 0.5-2 [51, 52].

2.4 Results

2.4.1 The CES1 G143E Variant Impaired MPH Hydrolysis in the Human Liver

Among the 102 HLS9 samples, five were identified as G143E heterozygotes, which is consistent with the previously reported minor allele frequency of this variant (2% - 4%) [21]. As shown in Fig. 2, the ritalinic acid formation rate in the G143E heterozygote group was 124.8 ± 20.3 pmol/mg protein/hr, which is approximately 50% of that in non-carriers (208.5 ± 96.7

pmol/mg protein/hr, P = 0.024). This observation is in accordance with the G143E variant being a loss-of-function mutation of CES1 [21].

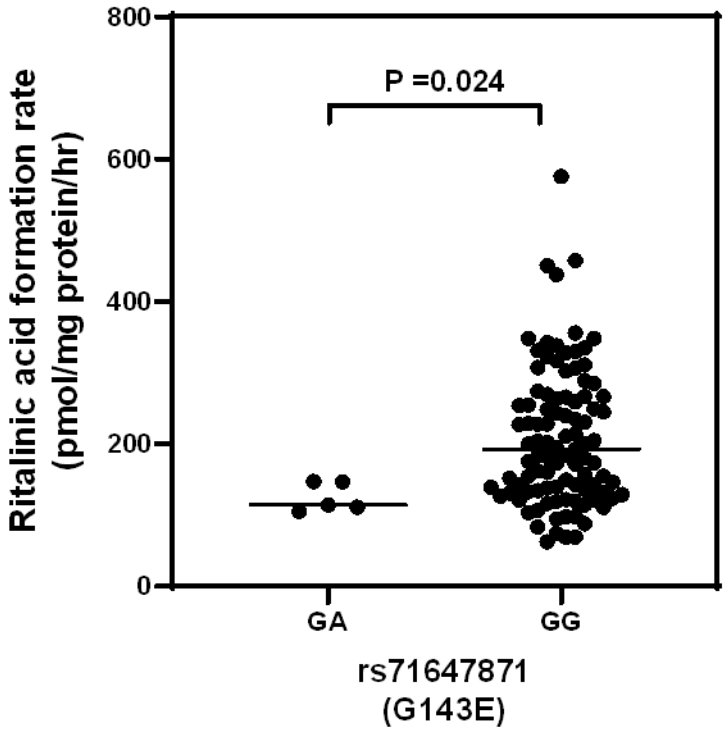

Figure 2-2 Effect of the CES1 genetic polymorphism G143E on MPH metabolism (hydrolysis) rate in 102 human liver S9 samples. The samples were categorized into two genotypes: G143E (rs71647871) heterozygote (G/A) and wild type (G/G). Horizontal bars indicate mean values in each group. Mann–Whitney U-test was utilized to test the differences in CES1 activity between the two genotypes.

2.4.2 Performance of the PBPK Models for Predicting MPH Exposure in a Healthy Adult Population

The developed PBPK model was used to predict d-MPH PK profiles in healthy adults from two independent d-MPH PK studies (0.15 mg/kg and 5 mg single oral dose) [20, 22]. As illustrated in Fig. 2-3A, the PBPK model successfully described the d-MPH PK profiles of both

doses, with all the observed/predicted ratios within the 80% - 120% range. The AUC and C_{max} values of the observed and predicted data are listed in Table 2-5.

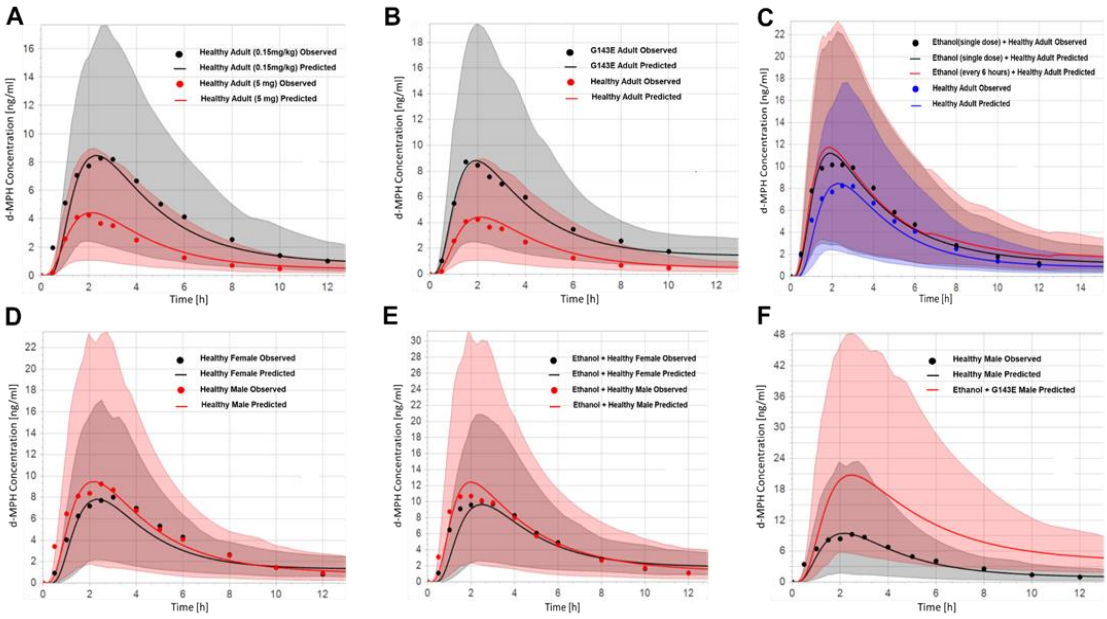

Figure 2-3 Simulated and observed plasma concentration-time profiles of d-MPH in different populations, including (A) a single oral dose of 0.3 mg/kg dl-MPH (i.e., 0.15 mg/kg d-MPH) and 10 mg dl-MPH (i.e., 5 mg d-MPH) in healthy adult populations; (B) a single oral dose of 10mg dl-MPH in healthy adult CES1-G143E carriers and non-carriers; (C) a single oral dose of 0.3 mg/kg dl-MPH co-administrated with a single dose of 0.6 g/kg ethanol 0.5 hours after MPH dosing or additional does of ethanol (0.6 g/kg) every 6 hours in a healthy adult population; (D) a single oral dose of 0.3 mg/kg MPH in healthy males and females, in which simulations were conducted in a virtual female population with hepatic CES1 expression 20% higher than males; (E) a single oral dose of 0.6 g/kg ethanol was given 0.5 hours after oral administration of 0.3 mg/kg MPH in different sex, in which hepatic CES1 expression was set as 20% higher in females than males during the simulations; (F) Simulations of virtual male G143E subjects who received a single oral dose of 0.3 mg/kg dl-MPH and 0.6 g/kg ethanol 0.5 hours after the

administration of MPH. The observed data were obtained from two MPH clinical studies[20, 22]. The colored shadow areas represent the 5th and 95th percentiles of the predicted mean values. The filled circles are observed mean values from the clinical study, and the solid lines represent the predicted mean plasma d-MPH concentrations.

Table 2-5 Cmax and AUC of the observed and predicted d-MPH PK

Treatment [a]	Population[b]	C_{max} (ng/ml)			$AUC_{(0\text{-}inf)}$ (ng.h/ml)		
		Observed	Predicted	Predicted /Observed C_{max} Ratio	Observed	Predicted	Predicted /Observed AUC Ratio
d-MPH 0.15 mg/kg [20]	Healthy Adult	8.3	8.47	1.02	52.1	49.3	0.95
d-MPH 5 mg [22]	Healthy Adult	4.2	4.42	1.05	21.4	25.7	1.20
d-MPH 5 mg [22]	G143E variant	8.7	8.81	1.01	53.3	57.6	1.10
d-MPH 0.15 mg/kg [20]	Healthy Male	9.3	9.48	1.02	54.2	53.7	0.99
d-MPH 0.15 mg/kg Ethanol 0.6 g/kg [20]	Healthy Male	10.8	12.4	1.15	67.6	81.1	1.20
d-MPH 0.15 mg/kg Ethanol 0.6 g/kg	G143E variant, Male	NA	20.81	NA	NA	167.4	NA
d-MPH 0.15 mg/kg [20]	Healthy Female	8.0	7.83	0.98	47.4	44.2	0.93
d-MPH 0.15 mg/kg Ethanol 0.6 g/kg [20]	Healthy Female	10.1	9.66	0.96	57.4	55.3	0.96
d-MPH 0.15 mg/kg Ethanol 0.6 g/kg [20]	Healthy Adult	10.2	11.23	1.1	62.8	67.4	1.07

a. Both observed and simulated data are reported as the mean values
b. The male and female ratio is 1:1 if not specified

2.4.3 Simulation of d-MPH Exposure in G143E Heterozygotes

G143E is a known loss-of-function variant [53], and our HLS9 incubation study demonstrated a 50% decrease in CES1 activity in livers heterozygous for G143E (Fig. 2).

Accordingly, a virtual European adult population, "G143E", was created to represent heterozygotes by reducing CES1 activity to 50%. The resulting PBPK model was applied to simulate d-MPH PK, and the simulated results were compared to the data obtained from a published MPH PK study containing healthy G143E heterozygous subjects (Fig. 2-3B) [22]. The ratios of the predicted data to the observed data were within the 80% - 120% range, indicating that a 50% reduction in CES1 activity in G143E heterozygotes can explain the d-MPH exposure difference between G143E carriers and non-carriers. The fold changes of C_{max} and AUC relative to the control group (5 mg/kg d-MPH, healthy adult population) are listed in Table 2-6.

Table 2-6 Fold changes of the observed and predicted d-MPH PK in different groups compared with control groups[a]

Treatment	**Population[b]**	**C_{max} fold change**		**$AUC_{(0\text{-}12h)}$ fold change**	
		Observed	**Predicted**	**Observed**	**Predicted**
d-MPH 0.15 mg/kg [20]	Healthy Male	1.12	1.12	1.04	1.09
d-MPH 0.15 mg/kg [20]	Healthy Female	0.96	0.92	0.91	0.90
d-MPH 0.15 mg/kg [20] Ethanol 0.6 g/kg	Healthy Adult	1.23	1.32	1.21	1.37
d-MPH 0.15 mg/kg [20] Ethanol 0.6 g/kg	Healthy Male	1.30	1.46	1.30	1.64
d-MPH 0.15 mg/kg [20] Ethanol 0.6 g/kg	Healthy Female	1.22	1.14	1.10	1.12
d-MPH 5mg [22]	G143E variant	2.07	2.0	2.5	2.24
d-MPH 0.15 mg/kg Ethanol 0.6 g/kg	G143E variant, Male	NA	2.46	NA	3.40

a. Control groups are healthy adult subjects, including 50% of females treated with the same dose of d-MPH. The fold changes are calculated for observed and predicted values separately ($observed_i/observed_{control}$, $predicted_i/predicted_{control}$)
b. The male to female ratio is 1:1 if not specified

2.4.4 MPH-ethanol DDI Prediction

Ethanol increases the overall exposure of d-MPH by 23% because of its inhibitory effect on CES1 [20]. Our DDI PBPK model was developed by integrating this inhibitory effect, and it described well the increase of d-MPH exposure following a single oral dose of 0.6 g/kg ethanol (Fig. 2-3C). We simulated the impact of multiple doses of ethanol on MPH exposure to predict the DDI between ethanal and MPH in the real-world scenario. As shown in Fig.2-3C, subjects receiving 0.6 g/kg ethanol every 6 hours exhibited a similar C_{max} value but a 12.4% increase of $AUC_{0\text{-}last}$ compared to those treated with a single dose of ethanol. When compared with the group without ethanol treatment, C_{max} and $AUC_{0\text{-}last}$ increased by 39.7% and 53.2%, respectively, in those receiving multiple doses of ethanol. However, we were unable to verify the simulation results because of a lack of clinical studies concerning the DDI between MPH and multiple doses of ethanol. Moreover, to evaluate how a delayed ethanol administration could affect MPH PK, we simulated various scenarios in which a single dose of ethanol was administrated at 0.5 hours and at an incremental interval of 0.5 hours up to 8 hours following MPH administration and compared the AUCs to the group free of ethanol. We found that a statistically significant MPH-ethanol DDI was observed only when ethanol was given within 3 hours following MPH administration (data not shown).

2.4.5 Simulation of Sex Difference in d-MPH Exposure

When default PK-Sim built-in parameters were used in the model, MPH exposure did not differ between males and females (data not shown). However, as reported by Patrick et al. [20], males and females have different PK of d-MPH, with females being 14.3% lower in AUC and 16.3% lower in C_{max}. Our in vitro human liver S9 studies suggest that this is likely due to that hepatic CES1 expression is higher in females than males [28]. Using PBPK modeling, we found

that a 20% increase in hepatic CES1 expression can capture the d-MPH PK difference between males and females, as shown in Fig. 2-3D and Table2-3.

2.4.6 Prediction of MPH-ethanol DDI in Different Sex

Next, we studied if ethanol will affect MPH PK profiles differently in males and females. To simulate this scenario, sex-dependent hepatic CES1 expression and ethanol-induced reduction of CES1 activity were both applied to the PBPK model. As shown in Fig. 2-3E and Table 2-5, when ethanol was co-administrated, MPH plasma concentrations differed between males and females during the absorption phase (0-3 hours post-dose), and the exposure remained similar between sex groups after 3 hours following MPH administration.

2.4.7 Simulation of the Effect on d-MPH PK of Interplay Among the G143E Variant, DDI, and Sex

To study how ethanol inhibition will affect the MPH exposure in males with the G143E variant, MPH PK profiles of this population with 0.6 g/kg ethanol administration were simulated. In this virtual population, the CES1 activity was reduced by 50% to reflect the impaired CES1 activity due to G143E mutation, and CES1 expression was adjusted to be 20% lower than females. As shown in Fig. 2-3F, male G143E heterozygotes who consume alcohol are expected to exhibit the highest level of d-MPH exposure, with AUC and C_{max} being respectively 340.1% and 240.6% greater than healthy males who do not drink alcohol (Table 2-5, Table 2-6). Although no observed data are available for male alcohol drinkers who are G143E heterozygotes, our model predicts that the MPH exposure could increase dramatically compared to the healthy male population without ethanol administration.

2.5 Discussion

The present study utilized a ‘‘predict-learn-confirm analysis” strategy [54] for the development of an MPH PBPK model, which was used to assess the effect of G143E variant, ethanol consumption, and sex alone or in combination on d-MPH PK. We determined in vitro CES1 activity on MPH metabolism using individual HLS9 samples and used it as a critical parameter for building the PBPK model. The final MPH PBPK model was verified with clinical data sets and well predicted the PK profiles. The established PBPK model was further used to predict MPH PK under various conditions (i.e., G143E genotypes, alcohol consumption, and sex) that have not been examined in clinical settings.

Genetic polymorphisms are critical contributors to interindividual variability in PK and PD. The CES1 nonsynonymous variant G143E has been shown to affect the exposure and clinical outcomes of CES1 substrate medications significantly, such as MPH [22, 55]. Our MPH HLS9 incubation study showed G143E heterozygotes had reduced MPH metabolic activity by approximately 50% (Fig. 2). As illustrated in Fig.2-3B, the PBPK model performed reasonably well with all observed data from a clinical study falling within the 5^{th} and 95^{th} percentiles of the simulated values, although d-MPH exposure in the elimination phase was slightly overestimated in non-carrier populations (Fig.2-3A). Similar overestimation was also reported in a previous MPH PBPK model [43], in which case the prediction was improved after introducing additional MPH hydrolysis and oxidation in the gastrointestinal tract to their model. However, the contribution of the oxidation pathway to MPH metabolism in the gastrointestinal tract is considered minor [56], and the majority of MPH metabolism occurs in the liver via CES1-catalyzed hydrolysis [57]. Thus, we did not include the potential MPH metabolism in the gastrointestinal tract in the present model.

Physiological differences between males and females can affect drug absorption, distribution, metabolism, and elimination processes, resulting in sex-specific differences in PK and PD [58]. PBPK modeling is a powerful tool for predicting PK profiles in different sex and for better understanding the mechanisms underlying the divergence. For MPH in particular, the PK and PD were found to differ between male and female healthy subjects, with d-MPH exposure being significantly lower in females relative to males [59]. It is interesting that no significant differences were predicted in the initial PBPK model when using default parameters in PK-Sim, suggesting that basic sex-specific anatomy and physiology do not account for the differences in d-MPH PK between males and females. Our published proteomics study revealed that hepatic CES1 protein expression and catalytic activity in females were approximately 20% greater than in males [28]. The modified PBPK model in which female hepatic CES1 protein expression was 20% higher than in males was able to capture the d-MPH exposure differences between males and females.

Many drugs have been identified to act as CES1 inhibitors [5]; among these, ethanol is the only inhibitor that has demonstrated a consistent impact on the metabolism of CES1 substrates in humans [60]. The ethanol doses used in published clinical studies are relatively low for safety reasons, which may not be able to reflect the scenarios when people ingest multiple drinks. Thus, our simulations may have underestimated the magnitude of DDI between MPH and ethanal.

An important application of PBPK modeling is to simulate PK under various clinical scenarios where studies have not been or could not be performed in a clinical setting. Clinical studies have been conducted to determine the respective impacts of the G143E variant, ethanol-induced DDI, and sex on MPH PK; however, the combined effect of these contributing factors

on MPH exposure has not been assessed. In the present study, the simulation results suggest that d-MPH PK could be affected to various degrees by the interplay among these factors; in particular, the d-MPH AUC in a G143E heterozygous male alcohol drinker could be 3~4-fold higher than that in a non-carrier who does not consume alcohol. Some severe side effects, including sudden cardiac death, have been reported in patients treated with MPH [61, 62]. Although the causes of MPH adverse reactions are multifactorial, marked interindividual variability in MPH exposure is a potential contributing factor to the unwanted clinical outcomes. PBPK modeling allows for identifying some populations (e.g., male, G143E carrier, alcohol consumer) who are at higher risk of developing severe side effects upon MPH treatment, which could assist in developing appropriate personalized therapeutic regimens to improve the efficacy and safety of MPH therapy.

The current study has several limitations. Firstly, the reported MPH clinical data were limited, and the sample sizes were small, especially for the CES1 G143E carrier population. Thus, our model verification could be heavily affected by the inter-individual variability. Secondly, most of the HLS9 sample donors and the clinical study subjects were Caucasians, which may limit the application of the models to other populations. Lastly, while our PBPK modeling analysis suggests that the differences in MPH exposure between sex groups could be partially explained by the different hepatic CES1 expression levels between males and females, the model cannot fully account for the sex-related MPH PK variation.

In summary, our in vitro HLS9 incubation study demonstrated a 50% reduction of CES1 catalytic activity towards MPH metabolism in human livers with the G143E heterozygous genotype. PBPK models were developed and successfully simulated d-MPH exposure affected by the G143E genetic variant, ethanol-MPH DDI, and sex. These PBPK models predict that the

interplay of these contributing factors could have a significant impact on d-MPH PK. The model suggests that specific patient populations, such as male subjects who carry the G143E variant and consume alcohol, may be more likely to experience side effects associated with MPH overexposure. Our model provides an approach to better understand the mechanisms underlying interindividual variability in MPH PK and PD and could assist in developing a more effective and safer therapeutic strategy to treat patients with ADHD.

*This chapter was used with permission from [63]

Chapter 3 Developing a SWATH Capillary LC-MS/MS Method for Simultaneous Therapeutic Drug Monitoring and Untargeted Metabolomics Analysis of Neonatal Plasma

3.1 Abstract

Most medications prescribed to neonatal patients are off label uses. The pharmacokinetics and pharmacodynamics of drugs differ significantly between neonates and adults. Therefore, personalized pharmacotherapy guided by therapeutic drug monitoring (TDM) and drug response biomarkers are particularly beneficial to neonatal patients. Herein, we developed a capillary LC-MS/MS metabolomics method using a SWATH-based data-independent acquisition strategy for simultaneous targeted and untargeted metabolomics analysis of neonatal plasma samples. We applied the method to determine the global plasma metabolomics profiles and quantify the plasma concentrations of five drugs commonly used in neonatal intensive care units, including ampicillin, caffeine, fluconazole, vancomycin, and midazolam and its active metabolite α-hydroxymidazolam, in neonatal patients. The method was successfully validated and found to be suitable for the TDM of the drugs of interest. Moreover, the global metabolomics analysis revealed plasma metabolite features that could differentiate preterm and full-term neonates. This study demonstrated that the SWATH-based capillary LC-MS/MS metabolomics approach could be a powerful tool for simultaneous TDM and the discovery of neonatal plasma metabolite biomarkers.

3.2 Introduction

As an analogy to the well-known quote, “Children are not little adults”, infants are not just small children. Human organs and biochemical processes undergo substantial maturation after birth, which can greatly affect the pharmacokinetics (PK) and pharmacodynamics (PD) of drugs in neonates [64]. About 65% of drugs used in Neonatal Intensive Care Unit (NICU) are off-label uses and require dosage adjustment for neonatal patients [64]. For example, vancomycin is an off-label antibiotic widely used in NICU to treat late-onset sepsis caused by methicillin-resistant Staphylococcus aureus and coagulase-negative staphylococci [65]. The interindividual variability in vancomycin PK is high in neonates. De Hoog and colleagues reported that the half-life of vancomycin varied between 3.5 h and 10.0 h, and the clearance ranged from 0.63 to 1.40 ml/kg/min among neonatal patients [66]. Because of its narrow therapeutic window and significant nephrotoxicity and ototoxicity, therapeutic drug monitoring (TDM)-based dose individualization is essential to ensure the efficacy and safety of vancomycin treatment [67]. TDM could also be invaluable for many other medications, given that the PK profiles of most drugs have not been well characterized in neonates. Therefore, a reliable analytical method capable of simultaneously monitoring commonly used drugs in neonates is highly desirable. Besides TDM, determining the dynamic changes of endogenous small molecules at the system level (i.e., metabolomics) could lead to the discovery of metabolite biomarkers to further improve pharmacotherapy outcomes through individualized drug regimens. Thus, developing an analytical platform with the capability for both targeted TDM and global metabolomic profiling is of importance to clinical practice and research of precision pharmacotherapy in neonatal patients.

Liquid chromatography−mass spectrometry (LC-MS) has been widely used for both targeted and untargeted analyses of small and large molecules in various research settings [68-70]. Sequential Windowed Acquisition of All Theoretical Fragment Ion Mass Spectra (SWATH) technology is an emerging data-independent acquisition (DIA) strategy that isolates precursors into predefined small mass windows for fragmentation and collects all generated MS2 spectra for identification and quantification. SWATH was originally developed for global proteomics analysis and has demonstrated several advantages over conventional data-dependent and targeted data acquisition methods [71]. Unlike conventional data acquisition methods, SWATH generates a digital archive of comprehensive MS/MS data for both qualitative and quantitative analysis and allows for data re-interrogation without the need for sample re-reanalysis. Besides its wide application in proteomics, SWATH has been increasingly used in metabolomic and lipidomic research [72-74]. For example, Xiong et al. successfully applied a SWATH-based serum metabolomics method to identify pancreatic cancer biomarkers [75]. Drotleff et al. used a SWATH method for an untargeted large-scale lipidomic analysis of mouse plasma [76]. Due to the complexity of SWATH data, several sophisticated software packages have been developed for the efficient processing of SWATH data [72, 77, 78]. However, the SWATH technology has not been utilized for simultaneous TDM and untargeted plasma metabolomics profiling.

The purpose of this study was to develop and validate a SWATH-based analytical platform to enable the simultaneous analysis of global neonatal plasma metabolome and plasma concentrations of several commonly used medications in NICU, including ampicillin, caffeine, fluconazole, vancomycin, midazolam, and its metabolite α-hydroxymidazolam. The method was validated and successfully applied to the TDM and global metabolomics analysis of plasma samples from neonatal patients treated in a NICU.

3.3 Materials and Methods

3.3.1 Chemicals and materials

Ampicillin, caffeine citrate, fluconazole, midazolam, α-hydroxymidazolam, vancomycin hydrochloride, and the internal standards (IS) caffeine-^{13}C3 and midazolam-D4 maleate, LC–MS grade acetonitrile, water, and formic acid were purchased from Sigma Aldrich (St. Louis, MO, USA). All other chemicals and agents were of the highest analytical grade commercially available. Blank human plasma was purchased from Innovative Research (Novi, Michigan, USA). Blood samples were obtained from three preterm and three full-term neonates treated in the NICU of the University of Michigan Hospital. The study was approved by the Institutional Review Board at the University of Michigan. Plasma was separated from the whole blood after centrifugation and stored at -80°C until use.

3.3.2 Calibrators and quality control (QC) samples

Stock solutions of each analyte were prepared in methanol at a concentration of 1 mg/ml. Working standard solutions (100 µg/ml, 10 µg/ml, 1 µg/ml, 100 ng/ml, 10 ng/ml) were obtained by diluting stock solution in methanol. Calibration standards and quality controls (QCs) were prepared by spiking pooled blank human plasma with the working solutions (Table 3-1). Three concentrations of QC samples were summarized Table 3-2. The FDA Bioanalytical Method Validation Guidance and the ranges of the typical plasma concentrations of the candidate drugs (Table 3-3) were considered when choosing the concentrations of calibrators and QCs. Metabolomics QC samples were prepared by mixing pooled blank plasma and clinical plasma samples at a ratio of 1:1.

Table 3-1 Ionization parameters and retention times of the analytes and the internal standards

Compound	Retention Time(min)	Precursor ion(m/z)	Polarity	Molecular	Product ions (m/z)	Collision Energy(V)
Ampicillin	15.7	350.1	Positive	$[M+H]^+$	192.0, 160.0, 333.1	22.0
Caffeine	15.4	195.1	Positive	$[M+H]^+$	195.1, 138.1, 110.1	14.1
Caffeine-3C13	15.4	198.1	Positive	$[M+H]^+$	140.1, 112.1, 141.1	14.1
Fluconazole	17.2	307.1	Positive	$[M+H]^+$	307.1, 238.1, 220.1	20.3
Midazolam	19.2	326.1	Positive	$[M+H]^+$	291.1, 290.1, 244.0	21.1
α-hydroxymidazolam	19.1	342.1	Positive	$[M+H]^+$	342.1, 324.1, 203.0	22.0
Midazolam-D4	19.2	330.1	Positive	$[M+H]^+$	291.1, 234.1, 295.1	21.1
Vancomycin	14.9	724.7	Positive	$[M+2H]^{2+}$	144.1, 100.1, 724.7	41.3

Table 3-2 Analyte concentrations in the quality control samples

	QC_{low}	**QC_{medium}**	**QC_{high}**
Ampicillin	0.25 μg/ml	1 μg/ml	10 μg/ml
Caffeine	1 μg/ml	4 μg/ml	10 μg/ml
Fluconazole	0.25 μg/ml	1 μg/ml	10 μg/ml
Midazolam	0.1 μg/ml	1 μg/ml	10 μg/ml
α-hydroxymidazolam	20 ng/ml	100 ng/ml	400 ng/ml
Vancomycin	0.1 μg/ml	1 μg/ml	10 μg/ml

Table 3-3 Performance of calibration curves, LLOQ, LLOD, and typical plasma concentration ranges of the targeted compounds

Compound	Calibration Curve			LLOQ (ng/ml)	LLOD (ng/ml)	Typical concentration range (µg/ml)
	Slope	R^2	Linear range			
Ampicillin	0.0103	0.992	0.1-20 µg/ml	100	5	0.85-46.4 [79]
Caffeine	0.0039	0.999	0.5-20 µg/ml	500	0.5	5-20 [80]
Fluconazole	0.0254	0.997	0.2-20 µg/ml	200	1	0.5-14 [81]
Midazolam	0.0291	0.999	0.02-50 µg/ml	20	1	0.08-3.2 [82]
α-hydroxymidazolam	0.0244	0.994	5-500 ng/ml	5	1	0.008-0.062 [83, 84]
Vancomycin	0.0028	0.998	0.002-50 µg/ml	2	0.5	0.5 -60 [85]

3.3.3 Sample preparation

For calibrators, 25 µl of pooled blank human plasma was mixed with 25 µl of working solutions, followed by the addition of 150 µl of methanol containing 100 ng/ml IS. For clinical samples, 25 µl of plasma was mixed with 175 µl methanol containing the same amount of IS. Caffeine-^{13}C3 was used as the IS for the quantification of ampicillin, caffeine, fluconazole, and vancomycin, and midazolam-D4 maleate was the IS for midazolam and α-hydroxymidazolam quantification. Samples were vortexed thoroughly for 10 min and centrifuged at 20,000 rcf for 10 min at 4°C to remove the precipitated proteins. The resulting supernatant was transferred to a new Eppendorf tube and was vacuum dried in a SpeedVac SPD1010 concentrator (Thermo Scientific, Hudson, NH). Samples were then reconstituted in 50 µl of water/acetonitrile mixture (4:1, v/v) and vortexed for 10 min. After centrifugation at 20,000 rcf for 10 min at 4°C, 0.5 µl of the supernatant was injected into an LC-MS/MS system for analysis.

3.3.4 SWATH data acquisition

A SWATH-based LC-MS/MS method was established for both targeted quantification and non-targeted metabolomics analysis. The LC-MS/MS system consisted of a TripleTOF 5600 plus mass spectrometer (Sciex, Framingham, MA) coupled with a Digital PicoView 450 nanospray ion source (New Objective, Woburn, MA) and an Eksigent 2D plus LC system (Eksigent Technologies, Dublin, CA). An ACQUITY UPLC M-Class Peptide BEH C18 column (130 Å, 150 μm × 100 mm,1.7 μm, Waters, Milford, MA) was used for the chromatography separation at 40°C. The mobile phase A and B were water and acetonitrile, respectively, and both mobile phases contained 0.1% (v/v) formic acid. The mobile phase was delivered at a flow rate of 1 μl/min with the following gradient: the gradient started with 3% of B and was kept for 10 min, then linearly increased to 100% at 40 min and held for 3 min, and then changed back to 3% in 1 min and held till the end of the 50 min gradient.

The SWATH acquisition included an MS1 full scan at an m/z range of 100-1,250 Da and 60 variable precursor isolation windows calculated by the Sciex SWATH Variable Window Calculator (ESM2). For each SWATH isolation window, the MS1 and MS2 accumulation times were 150 ms and 30 ms, respectively, resulting in a cycle time of 2 seconds. The average peak width of analytes was about 30 seconds, and thus, approximately 15 data points were collected for each peak. Data were acquired under a positive electrospray ion (ESI) mode. Collision energy (CE) voltage was automatically optimized by the acquisition software (Analyst TF 1.7) for each SWATH window with the CE spread (CES) set at 15 V. The declustering potential was 100 V, the voltage of the spray was set at 3,800 V, and the temperature of the interface heater was 200°C. For the gas settings, the ion source Gas 1 was 52, the ion source Gas 2 was 0, and the curtain gas was 30.

3.3.5 Method validation

linearity and lower limit of quantification (LLOQ)

The linearity of analyte response was evaluated based on the correlations between the analyte to IS peak area ratios and the nominal analyte concentrations of the calibrators. A weighting factor of 1/x was used for calculation. The LLOQ was defined as the lowest concentration with a signal-to-noise ratio greater than 10, a coefficient of variation (CV%) $\leqslant$ 20%, and accuracy between 80% and 120% of the nominal concentration. A calibration curve was accepted when the back-calculated concentrations of calibrators were within 100 ± 15% of the nominal values (except for 100 ± 20 % for the LLOQ).

Intra-batch and Inter-batch accuracy and precision

Intra-batch accuracy and precision were assessed by analyzing five replicates of QC samples at three concentrations (QC-Low, QC-Medium, QC-High). Accuracy was evaluated based on the differences between the measured concentrations and the nominal concentrations. Precision was determined by calculating the CV% of the five replicates. Inter-batch accuracy and precision were assessed by analyzing the QCs from three independent batches. The acceptance criteria for the Intra-batch and Inter-batch accuracy and precision were that the measured concentrations should be within 100 ± 15% of the nominal concentrations, and the CV% should be no more than 15%.

Stability, matrix effect, and extraction recovery

Autosampler stability, freeze-thaw stability, matrix effect, and extraction recovery were assessed for each analyte using QC samples at three concentrations. Autosampler stability was studied after the extracted analytes were placed in the autosampler (4°C) for 24 hours and 48 hours before injection. For freeze and thaw stability, samples were analyzed after three consecutive freeze-thaw cycles, during which the samples were frozen at -80°C and thawed at

room temperature. Matrix effect was evaluated by comparing the peak area of the analytes dissolved in the mobile phase to that of the same concentrations of analytes spiked in the post-extracted plasma. Extraction recovery was determined by comparing the peak areas of the analytes exacted from blank plasma samples spiked with the analytes (i.e., pre-spike) with the peak areas of the analytes spiked in blank plasma extraction eluent (i.e., post-spike).

3.3.6 Data processing and statistical analysis

The workflow of the SWATH data acquisition and analysis is summarized in Fig 3-1. The Skyline software (version 20.1, University of Washington, Seattle, WA) [86] was used for the targeted analysis. The sum of MS1 and MS2 peak areas were utilized for quantification, and the analyte concentrations were calculated according to the analyte/IS peak area ratios. For untargeted metabolomics analysis, the MS-DIAL software (version 4.16) was used for peak detection, alignment, MS2 information extraction, relative quantification, and metabolite annotation [87]. The parameters of MS-DIAL are listed in Table 3-4, blank matrix samples were used for background subtraction in the MS-DIAL. Database-based metabolite annotations were conducted with a public metabolomics library (http://prime.psc.riken.jp/compms/msdial/main.html#MSP) containing 13,303 unique compounds. Following the MS-DIAL analysis, the peak areas of all the metabolite features in each sample were exported. Metabolite features which were detected in over 80% of the samples and showed a relative standard deviation (RSD) below 30% in the QC samples were included in data analysis. The data were then normalized to the average level and transposed before being exported to the SIMCA-P software (version 12.0, Umetrics) for principal component analysis

(PCA) and partial least-squares discriminant analysis (PLS-DA).

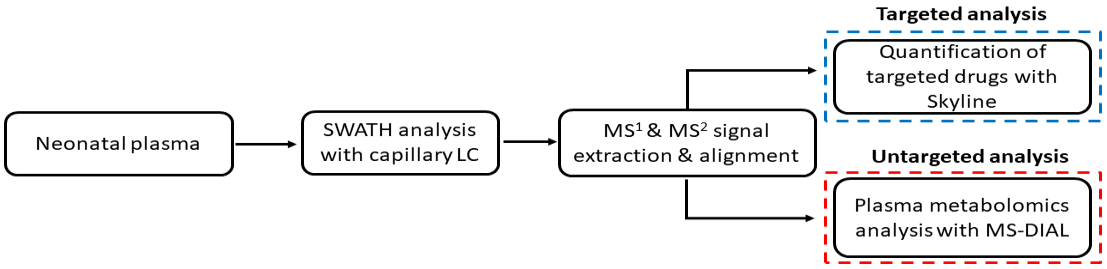

Figure 3-1 Workflow of the SWATH capillary LC-MS/MS method for simultaneous therapeutic drug monitoring and untargeted metabolomics analysis

Table 3-4 MS-DIAL software parameters used for untargeted metabolomics analysis

Data collection parameters	
Retention time begin	0.1
Retention time end	50
Mass range begin	25
Mass range end	1250
Mass accuracy parameters	
MS1 tolerance	0.01
MS2 tolerance	0.05
Peak detection parameters	
Smoothing method	Linear Weighted Moving Average
Smoothing level	3
Minimum peak width	5
Minimum peak height	1000
Mass slice width	0.1
Deconvolution parameters	
Peak consideration	Both
Sigma window value	0.5
Exclude after precursor	TRUE
MSP file and MS/MS identification setting	
MSP file	MSMS-Public-Pos-Curated-VS15.msp
Retention time tolerance	100
Accurate mass tolerance (MS1)	0.01

Accurate mass tolerance (MS2)	0.05
Identification score cut off	80
Text file and post identification (retention time and accurate mass based) setting	
Retention time tolerance	0.2
Accurate mass tolerance	0.01
Identification score cut off	85
Advanced setting for identification	
Top candidate report	TRUE
Adduct ion setting	
$[M+H]^+$	$[M+K]^+$
$[M+NH4]^+$	$[M+CH3OH+H]^+$
$[M+Na]^+$	$[M-C6H10O4+H]^+$
$[M+2H]^{2+}$	$[M-C6H10O5+H]^+$
Alignment parameters setting	
Retention time tolerance	0.1
MS1 tolerance	0.015
Retention time factor	0.5
MS1 factor	0.5
Peak count filter	1
QC at least filter	FALSE
Tracking of isotope labels	
Tracking of isotopic labels	FALSE

3.4 Results

3.4.1 Method validation

As presented in Figure 3-2, the chromatographic performance was acceptable for all analytes in neonate plasma samples under the present LC conditions. The chromatograms of blank plasma containing the analytes at the concentrations of LLOQ and of blank matrix demonstrated excellent sensitivity and selectivity of the assay (Figure 3-3, 3-4). The ionization parameters and retention times of the targeted analytes and the IS were listed in Table 3-1. The retention times of the analytes were between 14 min and 20 min, and the collision energy ranged from 14.1 V to 41.3 V. The targeted method was validated for calibration curves, linearity, intra-batch and inter-batch accuracy and precision, matrix effect, extraction recovery, and stability. All the calibration curve R^2 values were greater than 0.99, and the back-calculated concentrations of

the calibrators were within the range of 85%-115% of the nominal concentrations. The slope, intercept, R^2, and linear ranges of each calibration curve and the LLOQ and LLOD of the analytes were shown in Table 3-3. The intra-batch and inter-batch accuracy validation study showed that the measured concentrations of the QC samples ranged from 92.8% to 103.8% of the nominal concentrations (Table 3-5 and Table 3-6). The intra-batch and the inter-batch precision study demonstrated that the CVs of the QC samples were within 9.4% for all analytes (Table 3-5 and Table 3-6). The matrix effect study did not show significant ion suppression or ion enhancement for all analytes (Table 3-7). The extraction recovery rates were similar among the analytes, ranging from 89.9% to 113.9% (Table 3-7). The results also demonstrated that all analytes were stable after being kept in the autosampler for 48 hours or after three freeze-thaw cycles (Table 3-7, Table 3-8).

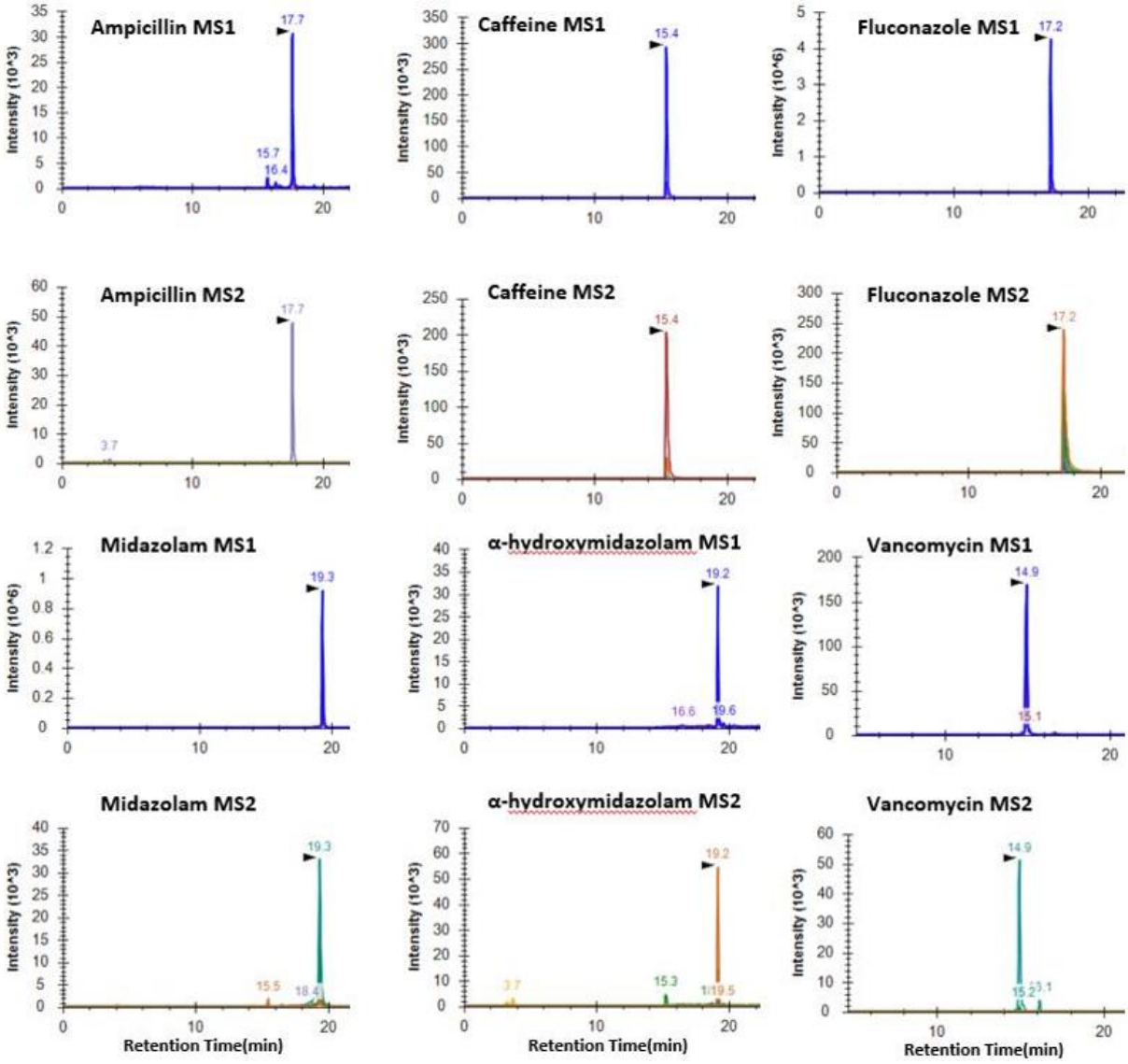

Figure 3-2 MS1 and selected MS2 chromatograms of the targeted analytes obtained from neonate samples

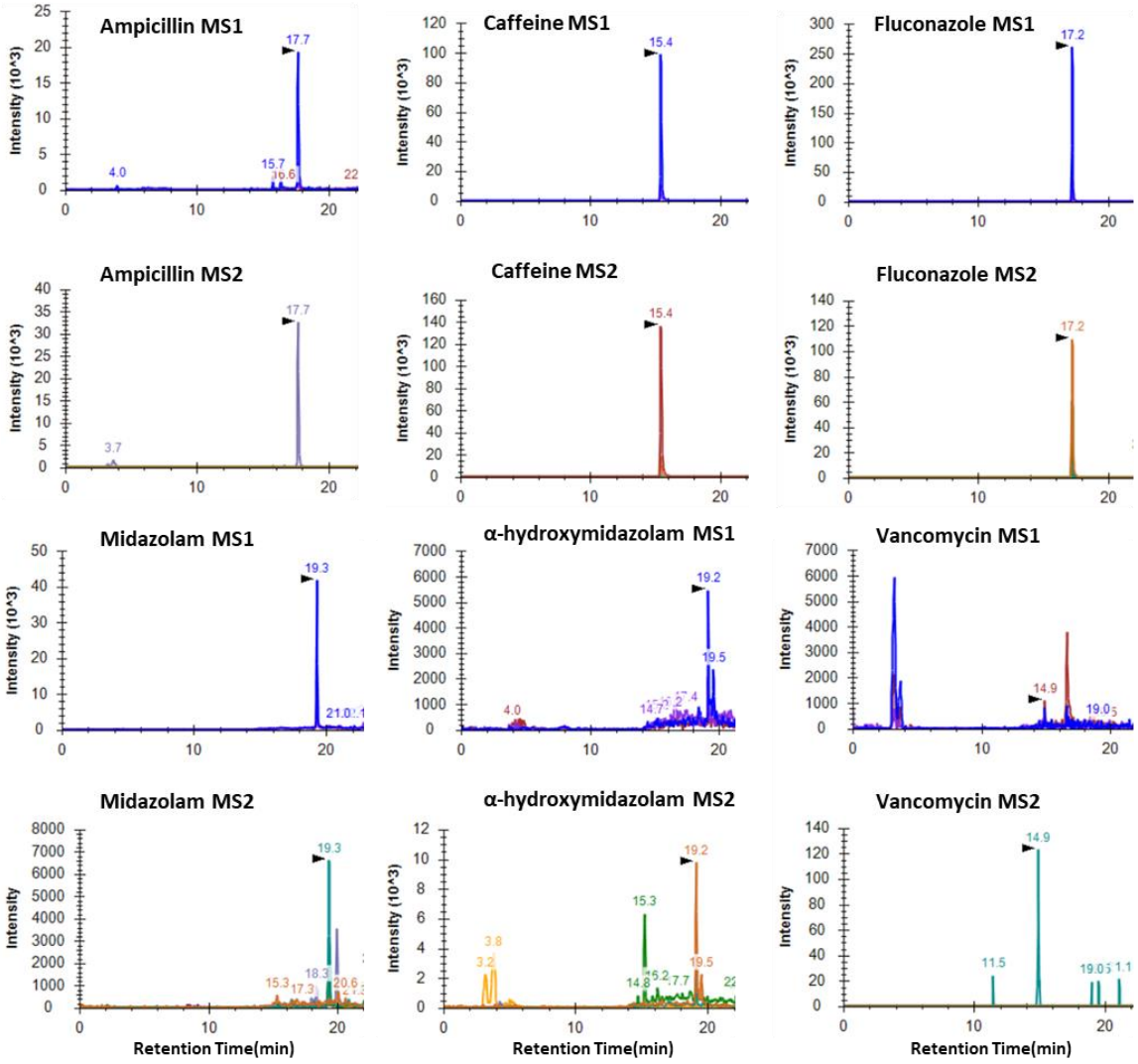

Figure 3-3 MS1 and selected MS2 chromatograms of the targeted analytes obtained from blank plasma spiked with the analytes at the concentrations of LLOQ

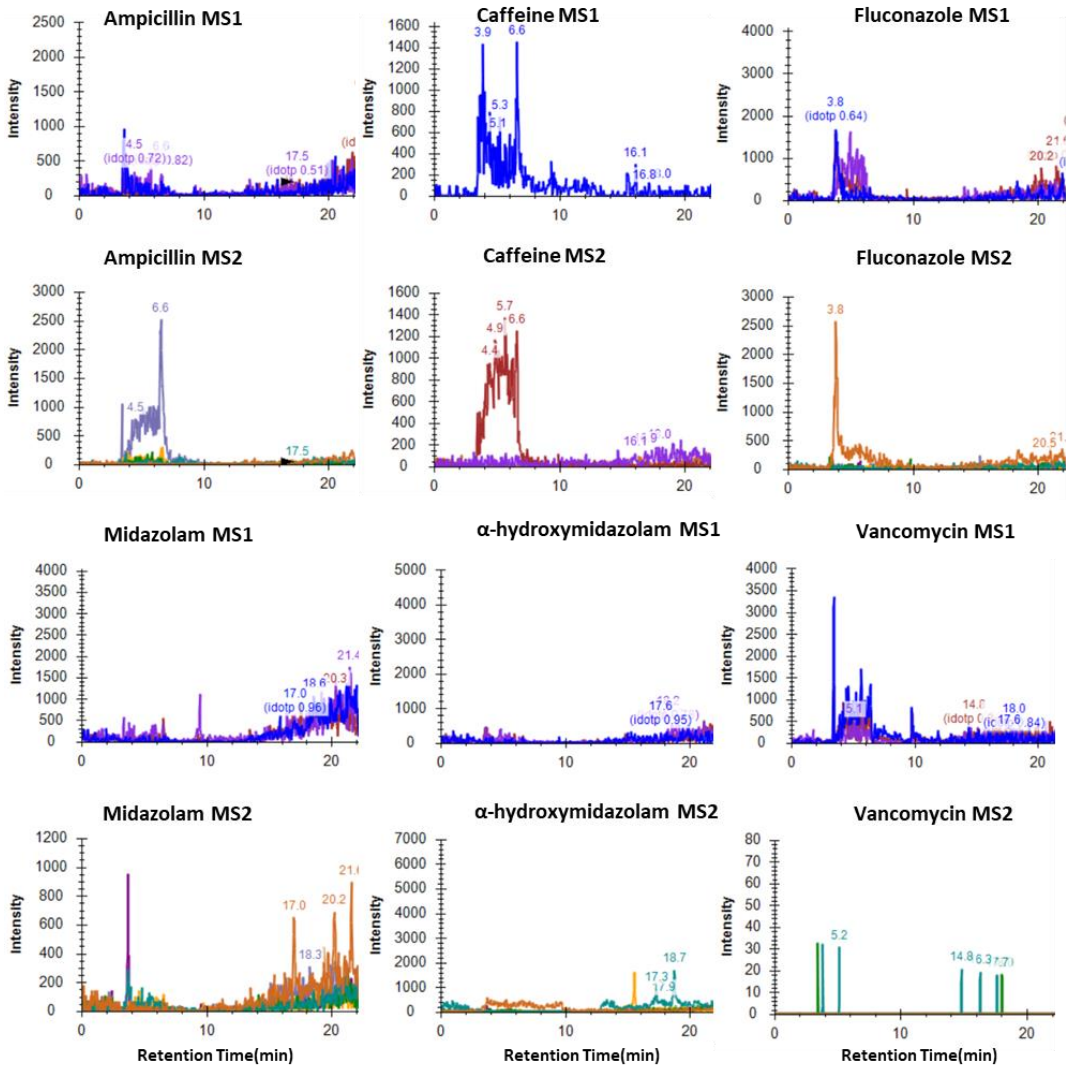

Figure 3-4 MS1 and MS2 chromatograms of the targeted analytes in the blank plasma

Table 3-5 Intra-batch precision and accuracy

	QC $_{low}$		**QC $_{medium}$**		**QC $_{high}$**	
	Precision (%)	Accuracy (%)	Precision (%)	Accuracy (%)	Precision (%)	Accuracy (%)
Ampicillin	7.0	103.3	5.3	93.6	9.4	101.7
Caffeine	5.4	102.6	8.0	99.6	1.7	102.4
Fluconazole	4.9	98.9	5.0	99.4	8.3	99.0
Midazolam	7.6	102.4	11.5	101.6	8.9	92.8
α-hydroxymidazolam	4.7	101.8	5.0	98.8	3.7	105.7
Vancomycin	5.2	100.3	9.4	96.6	2.5	103.8

Table 3-6 Inter-batch precision and accuracy

	QC $_{low}$		**QC $_{medium}$**		**QC $_{high}$**	
	Precision (%)	Accuracy (%)	Precision (%)	Accuracy (%)	Precision (%)	Accuracy (%)
Ampicillin	6.4	102.6	7.5	97.5	8.7	103.1
Caffeine	4.4	99.2	7.9	100.8	7.8	99.7
Fluconazole	8.1	103.4	5.8	99.8	6.5	99.7
Midazolam	6.4	100.1	8.7	102.2	9.1	97.2
α-hydroxymidazolam	5.9	102.6	5.9	97.2	6.8	102.2
Vancomycin	7.3	98.4	8.1	100.5	8.1	101.5

Table 3-7 Freeze and thaw stability, matrix effect, and extraction recovery

	QC $_{low}$			**QC $_{medium}$**			**QC $_{high}$**		
	F/T(%)	ME(%)	Recovery(%)	F/T(%)	ME(%)	Recovery(%)	F/T(%)	ME(%)	Recovery(%)
Ampicillin	103.6	95.5	103.2	102.4	108.3	95.2	111.8	100.4	110.8
Caffeine	97.9	100.1	103.1	102.9	106.6	98.6	96.8	92.4	105
Fluconazole	98.3	102.8	94.3	106.1	87.2	95.7	102.6	104.1	89.9
Midazolam	103.4	104.7	101.3	89.8	101.7	101.6	90.9	113.0	102.3
MiOH	100.7	95.2	103.2	91.8	86.9	93.2	91.5	85.3	90.0
Vancomycin	93.6	93.2	104.7	92.4	100.1	113.9	105.7	111.6	103.0

F/T: Freeze and thaw stability ME: Matrix effect

Values are the means from three independent experiments.

Table 3-8 Autosampler stability

	QC $_{low}$		**QC $_{medium}$**		**QC $_{high}$**	
	24 h (%)	48 h (%)	24 h (%)	48 h (%)	24 h (%)	48 h (%)
Ampicillin	100.4	104.0	98.9	101.2	99.4	111.1
Caffeine	98.5	96.4	101.5	103.2	99.9	96.7
Fluconazole	106.0	104.2	99.5	102.9	99.1	101.7

Midazolam	97.2	100.5	107.2	96.2	104.6	95.1
MiOH	103.0	103.7	101.0	92.7	104.3	95.4
Vancomycin	101.0	94.5	106.0	97.9	98.0	103.6

Values are the means from three independent experiments.

3.4.2 Untargeted metabolomics analysis

For the untargeted metabolomics analysis, a total of 2,245 metabolite features were detected from the human plasma samples. Among these metabolite features, 1,055 were annotated by the MS-DIAL software according to their accurate mass and MS/MS spectra. The distribution of the MS^1 ion intensity of the annotated metabolites was presented in Figure 3-5, showing that most of the annotated metabolites had ion intensity greater than 1×10^4 cps. The annotated plasma metabolites were classified into various classes of metabolites (Figure 3-6A), and the distribution of the annotated metabolites is in agreement with the previous reports [88, 89]. The MS^1 and MS^2 peaks of the representative annotated metabolites phenylalanine, and LPC 18:0 are shown in Figure 3-6B and Figure 3-6C, respectively. The measured MS2 spectra were matched with the reference metabolite spectra, which increased the credibility of the annotated metabolites. The reproducibility of this untargeted metabolomics method was evaluated by measuring four metabolomics QC samples. Figure 3-6D showed the RSD distribution of all the detected features in the four QC samples, and most of them are within 30%. The PCA analysis showed that the four QC samples were clustered closely (within 2 SD, Figure 3-7), indicating that the method was highly reproducible.

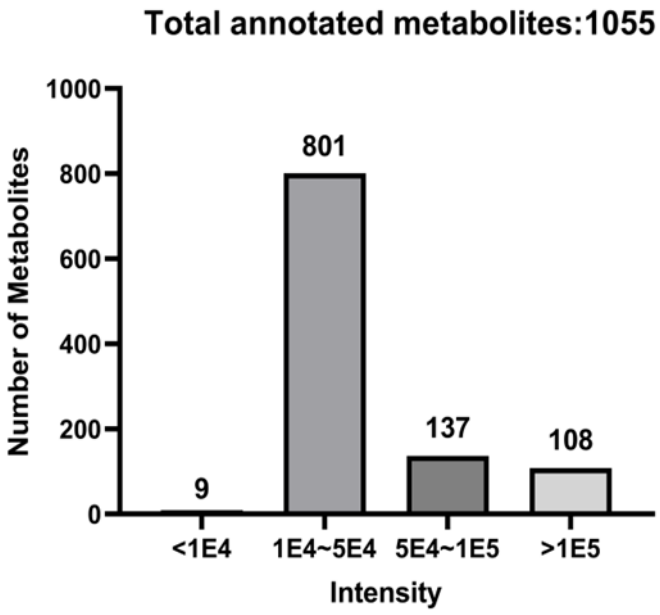

Figure 3-5 Distribution of the MS1 ion intensity of the annotated metabolites

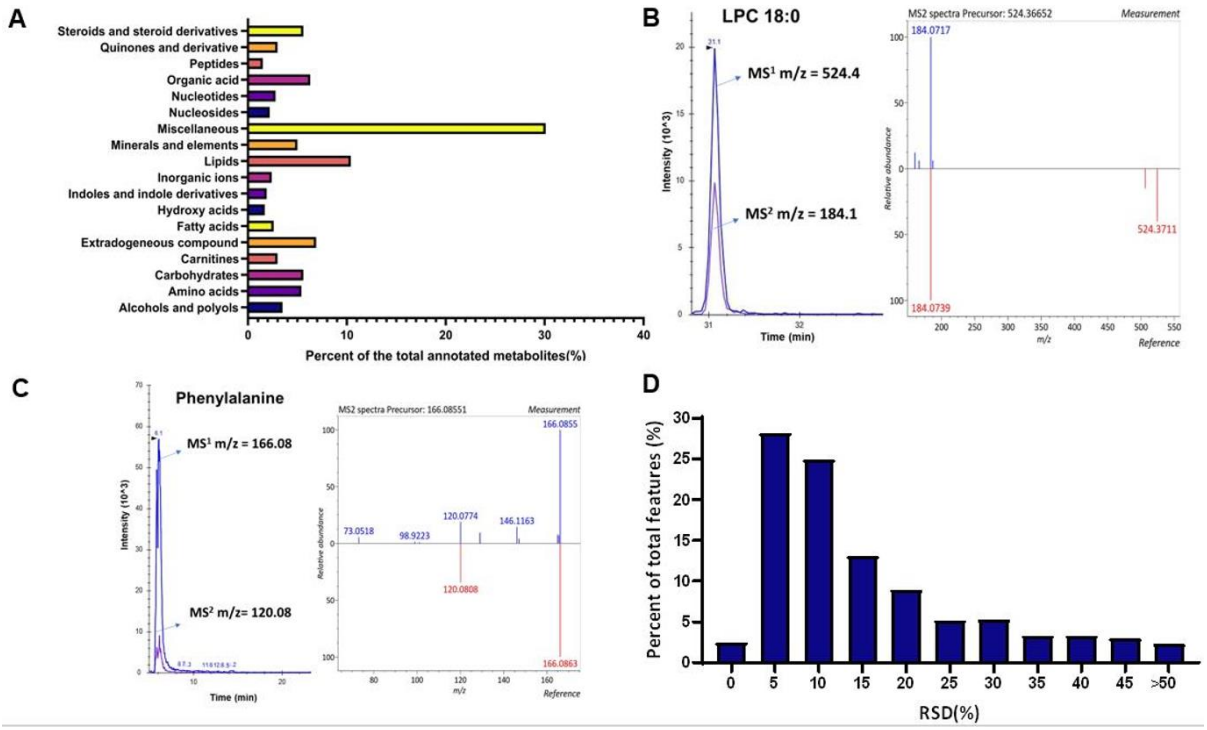

Figure 3-6 Profiles of the untargeted metabolomic analysis method. (A) Classification and relative abundance of the annotated metabolites (B) Example of identified metabolites phenylalanine, left panel: overlapped MS1 and MS2 peaks; right panel: deconvoluted MS/MS

spectrum from the plasma samples (blue) matched against database spectrum (red). (C) Example of identified metabolites LPC 18:0, left panel: overlapped MS1 and MS2 peaks; right panel: deconvoluted MS/MS spectrum from the plasma samples (blue) matched against database spectrum (red). (D) Distribution of RSD (%) of all the features in QC samples. The percentage of compound numbers within the corresponding %RSD range is represented by each column.

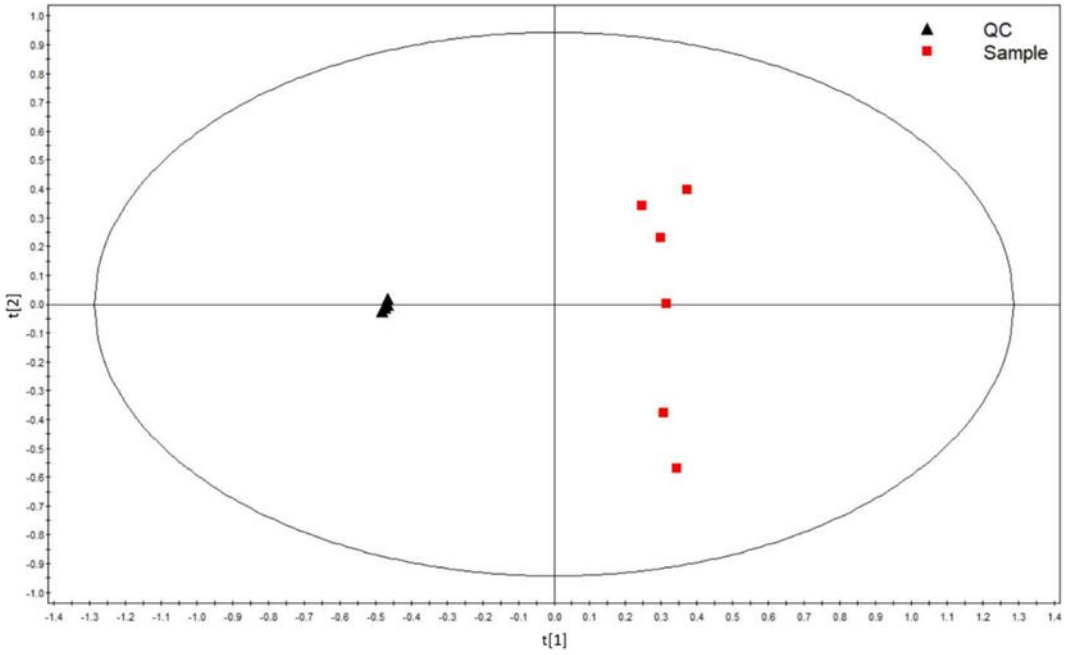

Figure 3-7 PCA score plot of the metabolic profiles of the QC and neonatal plasma samples. Black triangles represent four QC samples and red squares are the six neonatal samples

3.4.3 Application to clinical samples

The established SWATH metabolomics method was applied to the analysis of plasma samples collected from three preterm and three full-term neonatal patients who were treated with at least one of the five targeted drugs in the NICU of the University of Michigan hospital. As

shown in Table 3-9, all analytes of interest were successfully measured by the assay. It is noted that the drugs detected in the study were consistent with the drug administration information in the patients' electronic medical records, suggesting the excellent sensitivity and specificity of the method.

Table 3-9 Concentrations of targeted drugs (ng/ml) measured in neonate plasma samples

Patient number	Ampicillin	Caffeine	Fluconazole	Midazolam	α-hydroxymidazolam	Vancomycin
1	18,100	ND	ND	931	131	10
2	ND	ND	ND	617	53	ND
3	4,670	ND	ND	472	46	17
4	ND	16,100	12,400	2,560	130	8,910
5	ND	4,590	7,520	212	26	8,100
6	ND	ND	ND	ND	ND	13

ND: not detected

The SWATH method was evaluated for its capability in assessing the metabolome differences between preterm and full-term neonates. The drugs measured by the targeted metabolomic analysis were removed from the metabolome dataset to eliminate the contributions of the administered medications to their metabolomic profiles. The preterm and full-term neonates were completely separated in the PLS-DA score plot (model parameters: $R^2X = 0.76$, $R^2Y = 0.987$, $Q^2 = 0.324$) (Figure 3-8A). Due to the limited sample size (n = 3), the Q^2 value of the permutation plot and the CV-ANOVA test of the PLS-DA model could not be validated. In the S-plot of the PLS-DA scores (Figure 3-8B), variables with absolute covariance (X axis) > 0.05 and absolute correlation (Y axis) > 0.3 were in the shaded area and were considered to be the major contributors to the classification. The loading plot of the PLS-DA scores is shown in ESM1 Figure 3-9. The corresponding VIP values were calculated, and a total of 175 metabolite features

were found to have a VIP value > 1. For the univariate screening of statistically different metabolite features between the two groups, the Student's t-test with Bonferroni correction was utilized, and 106 features with $P < 0.05$ were retained. The fold changes of the normalized metabolite feature intensities were also calculated, and 622 features differed by greater than 20% between the two groups. The Venn diagram (Figure 3-8C) shows the overlapped features reported by the three data analysis approaches, and a total of 61 features were identified by all three methods to be the metabolites differentiating between the preterm and full-term groups. Nineteen out of the 61 metabolite features were annotated using the plasma metabolomic libraries from MS-DIAL and the Human Metabolome Database (HMDB). The relative abundances of these annotated metabolites in each sample were shown in the heatmap (Figure 3-8D) and violin plots (Figure 3-10).

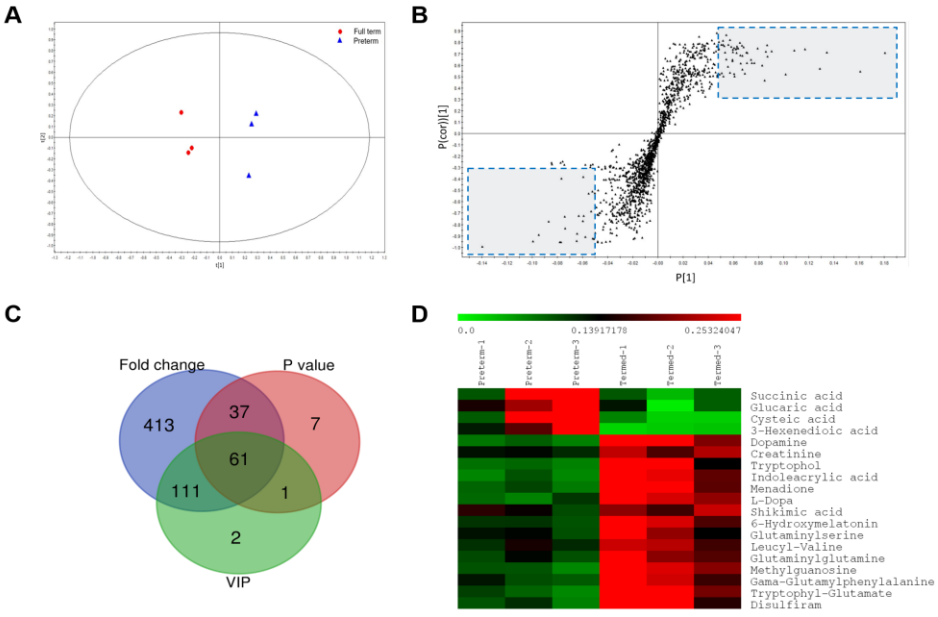

Figure 3-8 Metabolomics profiles of neonate samples. (A) PLS-DA score plot of the full-term and preterm neonates. Red dots represent the three full-term neonates, and blue triangles represent the three preterm neonates. (B) S-plot plot of the PLS-DA model. The variables that contributed most to the classification were in shaded areas. (C) Venn diagram of VIP (VIP>1, n=175), P-value (P < 0.05, n = 106), and fold change (FC < 0.8 or FC > 1.2, n = 622). (D) Heatmap of 19 potential differential metabolites between preterm and termed groups.

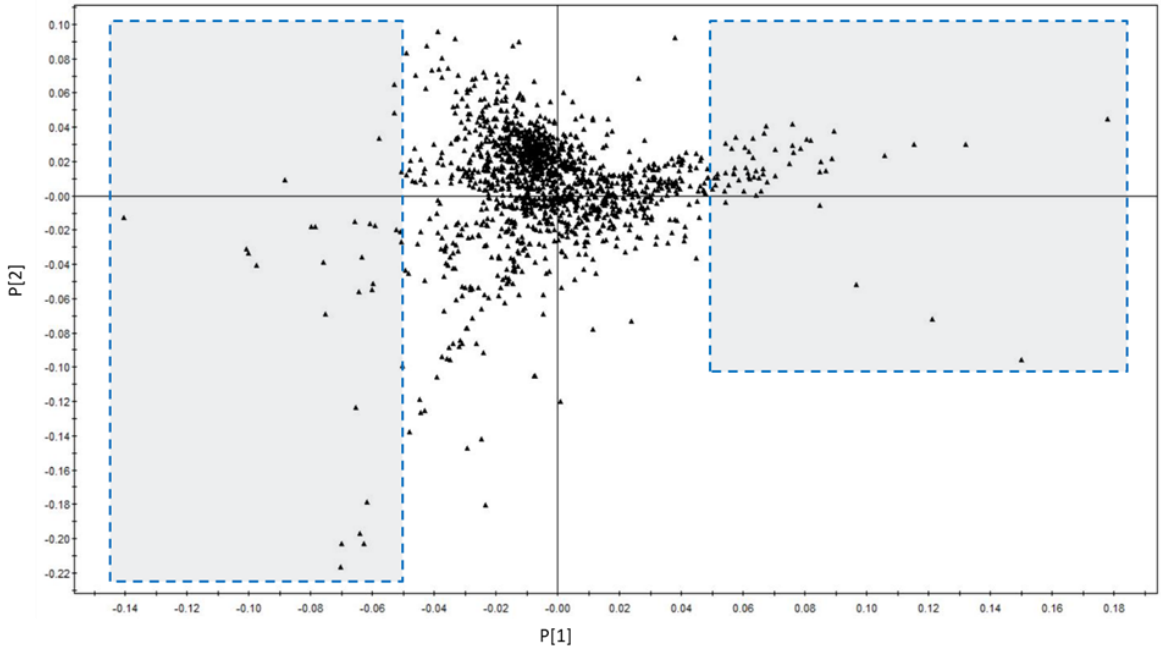

Figure 3-9 Loading plot of the PLS-DA model. The variables contributed most to the classification were in the shaded areas.

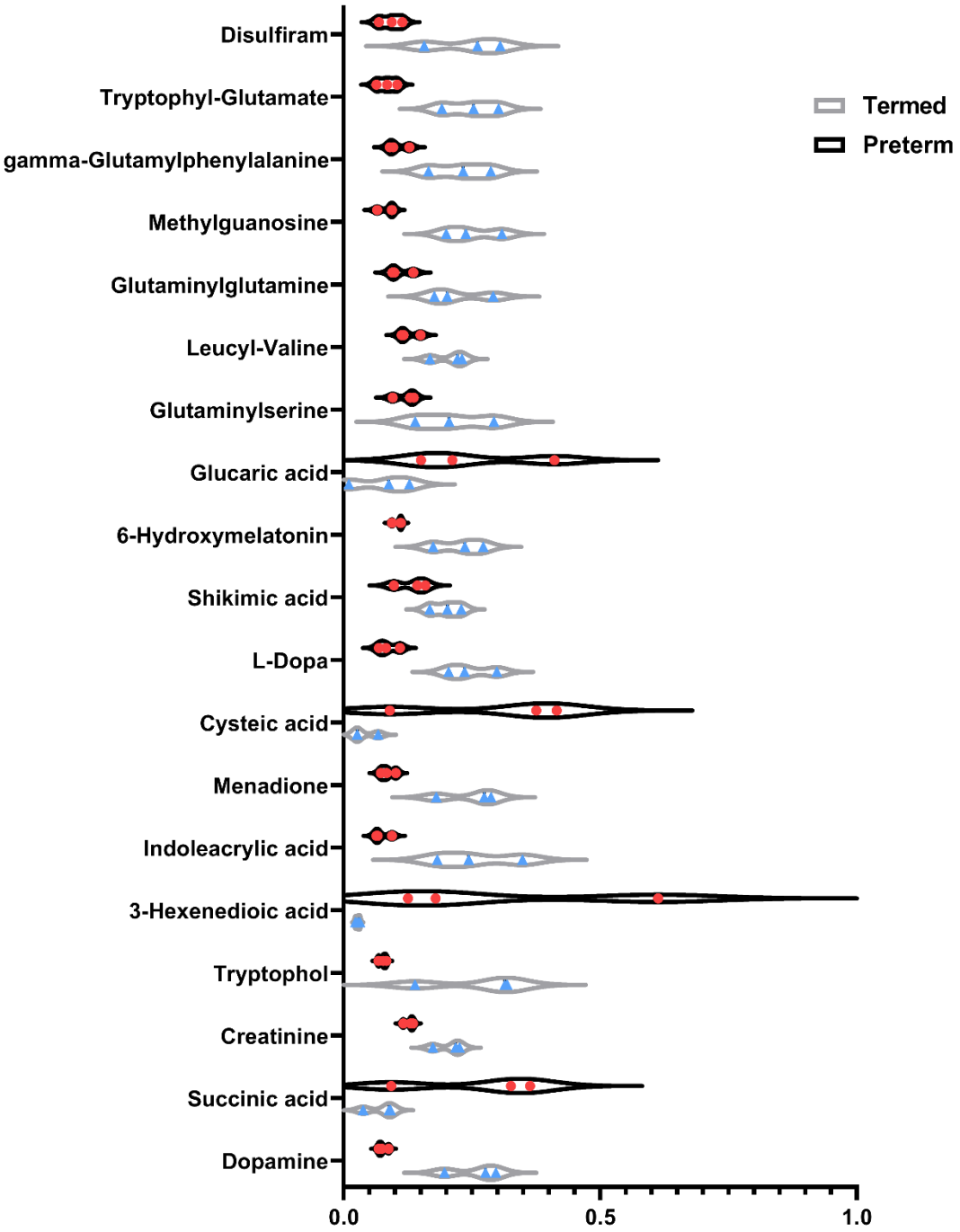

Figure 3-10 Violin plot of the 19 annotated plasma metabolites that differed between the preterm and termed neonates. Red circles are preterm subjects and blue triangles are termed subjects. The X axis is the normalized concentration level.

3.5 Discussion

In this study, a SWATH capillary LC-MS/MS metabolomics method was developed for both targeted quantification and global metabolite profiling. The method was validated for linearity, sensitivity, precision, and accuracy for the targeted analytes. We demonstrated its suitability for the quantification of several commonly used medications in neonates, including ampicillin, caffeine, fluconazole, vancomycin, midazolam, and its metabolite α-hydroxymidazolam. The assay was also successfully applied to the untargeted metabolomics analysis of six plasma samples collected from neonatal patients. The preterm and full-term neonates could be readily differentiated according to their metabolite features.

Nano-flow (e.g., 300 nl/min) is the mainstay for proteomics analysis [90], whereas analytical flow (e.g., 0.2 - 1 ml/min) is most common in metabolomics research [91]. Nano-LC offers greater sensitivity but is generally less robust compared to an analytical flow configuration. In the present study, a capillary-LC system with a 150 µm ID column and a flow rate of 1 µl/ml was employed to achieve a balanced performance of sensitivity and robustness. The results were found to be highly reproducible, as demonstrated by both the validation study of the targeted analytes and the results from the untargeted metabolomics study of the QC samples.

Different from other data acquisition modes (e.g., data-dependent acquisition and multiple reaction monitoring (MRM)), SWATH generates both MS1 and MS2 chromatograms of all analytes. Therefore, SWATH quantification can be based on the peak areas of MS1, MS2, or the sum of MS1 and MS2. We compared the performances of the three quantification approaches and found that the method utilizing the sum of MS1 and MS2 signals generally outperformed the methods using either MS1 or MS2 regarding sensitivity and reproducibility. For example, when only MS1 was used for vancomycin quantification, the LLOQ was 10 ng/ml, whereas the LLOQ

was 2 ng/ml when the quantification was based on the sum of MS1 and MS2. The variations of ampicillin and vancomycin calibration curves also increased when only MS1 signals were used (data not shown). In addition, when only MS2 signals were used, the R^2 values of the midazolam and ampicillin calibration curves decreased to 0.946 and 0.984, respectively. Accordingly, the sum of MS1 and MS2 peaks was utilized to quantify the targeted compounds throughout the study.

Several LC-MS/MS-based methods were established to quantify ampicillin [92], caffeine [93], fluconazole , midazolam, α-hydroxymidazolam [94], and vancomycin [95] in neonatal plasma. All these methods were based on the same MRM data acquisition strategy using low-resolution triple quadrupole mass spectrometers. As a comparison, this reported SWATH method utilized an emerging data-independent data acquisition technology on a high-resolution Q-TOF instrument. The generated SWATH data is a complete digital archive of all detected analytes. Thus, unlike those targeted methods (e.g., MRM), the SWATH approach allows post-acquisition data extraction. For example, if a new interest arises for a compound that was not targeted in the original study, investigators can re-interrogate the previously collected SWATH data and extract the quantitative information of the compound of interest. The flexibility of this approach was also demonstrated by two recent studies: Drotleff and collegues quantified steroid hormones in human plasma using SWATH-acquisition and untargeted profiling [96]. Sanwald et al. used both targeted and SWATH assays to quantify amino acids in human corneal epithelial cells treated with ionic liquids [97]. Moreover, the SWATH analysis generated thousands of metabolite features that successfully differentiated the preterm and full-term neonates enrolled in the study, indicating that the SWATH-based metabolomics could be a powerful tool for clinical biomarker discovery. In this preliminary study, 61 metabolite features were found to differ between the

preterm and termed neonates, among which 19 were annotated. The classes of the 19 annotated metabolites include organic acids, nucleotides, nucleosides, amino acids and indole derivatives. Some of them are critical in various signaling pathways. For example, both dopamine and its precursor L-dopa play important roles in the brain activity mediated by dopamine pathways, and the plasma concentrations of the two neurotransmitters were different between the preterm and termed neonates, which is consistent with a previous report showing that the activation of the dopamine pathways in preterm patients was different from that in termed patients [98]. Apart from the signaling pathways, some identified metabolites such as creatinine are indicators of the maturation of organ functions. Indeed, creatinine plasma levels were reported to be significantly different between preterm and termed neonates [99, 100]. However, it should be noted that only six subjects were included in this proof-of-concept study, and a larger sample size is warranted in order to perform a more in-depth global metabolomics analysis. Also, chemical standards are needed for authenticating the identified metabolite biomarkers.

In sum, we developed a SWATH capillary-LC-MS/MS analytical platform capable of simultaneously analyzing the compounds of interest and the whole plasma metabolomes of neonatal patients. This method is suitable for clinical TDM for multiple medications while concurrently generating comprehensive untargeted metabolomics data for biomarker discovery and targeted post-acquisition data extraction.

*This chapter was used with permission from [101]

Chapter 4 Population PK/PD Study of Midazolam in the Neonatal Intensive Care Unit Patients

4.1 Abstract

Midazolam is one of the most widely used sedatives in the neonatal intensive care unit (NICU). However, its concentration-effect relationship is still unclear in neonates, and clinical responses vary markedly between individuals. We conducted a population PK/PD study in neonates treated in the University of Michigan NICU to better understand the factors that determine midazolam PK and PD in neonatal patients. A two-compartment population PK model of midazolam with two sequential compartments for its metabolites 1-hydroxymidazolam and 4-hydroxymidazolam was built. After the stepwise screening, patient lab results like ALT and creatinine levels were incorporated as the covariates of the model. Our PK model prediction matched well with the observed data. For drug response prediction, a binary probability model was used as the final PD model. No direct correlation was observed between midazolam PK and PD based on the goodness-of-fit plot, even with midazolam metabolites concentrations being included.

4.2 Introduction

Midazolam (MDZ) is a benzodiazepine drug with rapid onset of action and short-acting for anesthesia, procedural sedation, and the management of trouble sleeping and severe agitation [83]. The sedative and anticonvulsant properties of midazolam are related to GABA

accumulation and the occupation of benzodiazepine receptors [102]. The half-life of MDZ is 1.9 hours in adults [103], and the bioavailability is about 50% when being absorbed through either oral or nasal mucosa [104].

In adults, MDZ is mainly metabolized by CYP3A4 and CYP3A5 enzymes through hydroxylation to form1-hydroxymidazolam (1-OH-MDZ). A small amount of MDZ can be metabolized to 4-hydroxymidazolam (4-OH-MDZ) by CYP3A7[105]. For pharmacological potent, 1-OH-MDZ is at least as potent as the parent compound, and 4-OH-MDZ is about 1/3 of 1-OH-MDZ regarding the sedative effect [106]. Both 1-OH-MDZ and 4-OH-MDZ are glucuronidated before excretion into urine [83]. In neonates, hepatic CYP3A4 activity is only about 20% of the adult level during the first several weeks of life [107], resulting in reduced midazolam clearance (CL) and 1-OH-MDZ concentration. Meanwhile, the hepatic CYP3A7 enzyme activity is higher in 1-3 months old neonates than in adults, which leads to higher blood levels of 4-OH-MDZ [107].

Physical growth and development are rapid in neonates; both the PK and PD of a drug in neonates could differ markedly from that in adults. To date, only a small number of drugs used in neonates are licensed for use in this specific group, and approximately 90% of the drugs used in neonatal intensive care are prescribed for off-label use [108]. Drug dosing regimens in neonatal patients are usually empirically derived from adult regimens using linear extrapolations based on body weight. However, the developmental changes during the neonatal stage are non-linear dynamic processes, and thus, using the linear extrapolation dosing paradigm may result in over or under-dosing and cause severe adverse effects and therapeutic failure. Thus, PK/PD studies in neonates are vital to improve the efficacy and safety of pharmacotherapy in this special population.

PK/PD research in the neonate population faces many challenges. Firstly, due to the relatively small body size, the quantity of blood samples that can be drawn from a neonate is limited, which often prevents an extensive sampling strategy-based conventional PK study [109]. Secondly, moral issues disallow “pediatric healthy volunteers”, and only neonatal patients who can benefit from the study could be enrolled, which greatly limits the design and performance of clinical trials. Thirdly, due to developmental changes, ontogeny, and the maturation of DMEs, it is challenging to scale neonatal doses from adult doses. In the face of all these challenges, population PK/PD modeling methods have been increasingly developed and applied to predict drug doses and responses in neonates. Population PK/PD models are particularly useful in the neonatal population[110], where repeat blood sampling is often infeasible and ethically inappropriate for a neonatal patient [111]. In addition, relative to allometric scaling, population PK/PD modeling allows the incorporation of more covariates, such as age (both post-natal and post-menstrual), body weight, and renal and liver functions, which could lead to better prediction performance.

Although MDZ is one of the most prescribed sedatives in the NICU, a concentration-effect relationship has been fully established for MDZ in the neonate population. Several studies have reported the discordance between the PK and PD of MDZ in neonates [112-114]. In this study, we built a MDZ population PK/PD model by incorporating MDZ and its two active metabolites and multiple covariates, aiming to explain the interindividual variabilities in the MDZ PK and PD and the relationship between the PK and PD in neonatal patients.

4.3 Materials and Methods

4.3.1 Patient and study designs

The study included neonate patients who were treated with midazolam for sedation and pain relief at the University of Michigan NICU. Neonates who were given MDZ were identified through the MiChart system. The residue whole blood samples left from patients' routine complete blood count (CBC) tests were collected. Informed consents were not required for this study. Patients' demographic information, medication history, and lab results were all obtained from MiChart or the University of Michigan DataDirect system.

4.3.2 Midazolam and its metabolites concentration measurements

Midazolam, 1-hydroxymidazolam, and 4-hydroxymidazolam concentration in plasma were simultaneously measured by an LC-MS/MS assay as previously described in Chapter 3. The lowest limit of quantification was 5 ng/ml for midazolam and 2 ng/ml for 1-hydroximidazolam and 4-hydroxymidazolam. The method validation results (precision, accuracy, matrix effect, extraction recovery, and stability) were within the acceptable range.

4.3.3 Midazolam PD response assessment

The PD response to midazolam treatment was assessed using the neonatal pain, agitation, and sedation scale (N-PASS). N-PASS is widely used in the NICU to assess the pain, agitation, and sedation levels in a critically ill infant with acute pain. The total score is documented as a positive number from 0 to 10, as shown in Table 4-1. The goal of pain treatment/intervention is to keep the N-PASS score under 3. In our study, the N-PASS scores were the mean values within 24 hours. The N-PASS variables were set to 0 (normal) if the N-PASS value is less than 3 and were set to 1 (abnormal) if N-PASS is over 3 in our final datasets for modeling.

4.3.4 Data set

In the current study, PK and PD data from 116 neonates who received the midazolam treatment were used for the population PK/PD analysis, including 545 PK and PD data points. The latent variables used as candidate covariates were dosing weight (kg), postnatal age (week), gestational age (week), sex, creatinine (mg/dl), serum aspartate transaminase (AST), and alanine transaminase (ALT).

4.3.5 Population PK/PD model development

The population PK/PD analysis was conducted using the nonlinear mixed effects modeling software NONMEM (ver. 7.4; Icon Development Solution, Ellicott City, MD, USA). The first-order conditional estimation (FOCE) method was used for model prediction. The inter-individual variability of each parameter was applied to the basic model with the exponential expression:

$$P_{ij} = \Theta_j * \exp(\eta_{ij})$$

Where P_{ij} is the value of the j^{th} parameter in the i^{th} individual; Θ_j is the typical value of the j^{th} parameter; η_{ij} is the interindividual variability of the j^{th} parameter for i^{th} individual, with a mean of 0 and variance of ω^2.

A proportional combined with additive error model was used to describe the residual error:

$$C_{obs,ij} = C_{pred,ij} *(1+ \varepsilon_{pro,ij})+ \varepsilon_{add,ij}$$

Where Cobs,ij is the observed value of the jth parameter in the ith individual; Cpred,ij is the predicted value of the jth parameter in the ith individual; εpro,ij and εadd,ij are the proportional and additive residuals of intra-individual variability, respectively. Their means are zero with variances being σ2pro and σ2add for the proportional and additive residuals, respectively. A similar error model was applied to PD observations. Model parameters were optimized by log-

likelihood ratio test (LRT), in which, if the decrease of the objective function value (OFV) was greater than 3.84 ($p<0.05$), the result for LRT was considered statistically significant.

To account for the variability in PK parameters due to the bodyweight changes of individual neonates during the study, clearances, and volumes of distributions were standardized to the median bodyweight of 2.74 kg with an allometric scaling model:

$$P_i = P_{2.74kg} * (WT_i/2.74)^{\Theta p}$$

Where P_i is the parameter of the ith individual. WT_i is the bodyweight of the ith individual, $P_{2.74kg}$ is the parameter of a neonate with a standardized bodyweight of 2.74kg, Θp is the power exponent fixed at 1 for volumes of distribution, and 0.75 for clearance.

For the midazolam PK model, one, two, and three-compartment models were evaluated. For the PD model, a logistic model for dichotomous data was utilized to explain the instantaneous PK-PD relationship:

$$P\ (Y=1) = C^{\gamma}_{pred,ij} / (EC^{\gamma}_{50} + C^{\gamma}_{pred,ij})$$

Where P (Y =1) is the probability that the response will occur, $C_{pred,ij}$ is the predicted concentration over time for individuals; EC_{50} is the plasma concentration that will produce 50% probability of response; γ express the steepness reflecting the interindividual variability in the measured effect. To implement this approach, the PD data (N-PASS) was transformed into a binary format. According to the N-PASS guidance, the goal of pain treatment/intervention is N-PASS score < 3, therefore, N-PASS values less than 3 were regarded as responders with DV=0, whereas values >3 were regarded as non-responders (DV=1).

4.3.6 Covariates analysis

To explain the interindividual and intraindividual variability in PK and PD parameters, several variables in the dataset were explored as covariates. The correlation of all the covariates

was studied. Covariates were incorporated into the basic model stepwisely: first, all the potential covariates were tested, and the covariates with the largest decrease of the objective function value (ΔOFV >3.84) were retained; the rest potential covariates were evaluated for the next round until no covariates could achieve the decrease of OFV >3.84 compared to the former model.

4.3.7 Model validation

The significant difference between models was tested by the changes in OFV (ΔOFV > 3.84). Goodness-of-fit plots were plotted for graphical analysis of the model prediction performance, including observed-versus-population predicted, observed-versus-individual predicted, weighted residual-versus-time, and weighted residual-versus-individual predicted. The median value and coefficient variance of each parameter were calculated. Predicted model parameters were compared with the published studies.

4.4 Results

4.4.1 Study population

Totally 116 neonates with 565 blood samples were included in this study. The demographics of study participants are listed in Table 4-1. The mean postnatal age of the neonate patients was 8.48 weeks, and the mean dosing weight was 2.74 kg. Midazolam was administrated via IV infusion or IV bolus, and the dosages ranged from 10 to 400 μg/kg/hour and 0.03 to 2 mg, respectively.

Table 4-1 Demographic information of neonate patients

	Mean	SD
Bodyweight (kg)	2.74	1.34
Postnatal Age (week)	8.48	11.60
Gestational Age (week)	33.52	5.60
ALT (iu/l)	71.76	122.90
AST (iu/l)	100.22	260.69
Creatinine (mg/dl)	0.40	0.26

4.4.2 Population PK modeling

For the structural MDZ PK model, one, two, and three-compartment models were tested, and the two-compartment model (central and peripheral) fits our observed data best. The MDZ metabolites, 1-hydroxymidazolam(1-OH-MDZ) and 4-hydroxymidazolam(4-OH-MDZ) were described by two sequential compartments separately. The schematic representation of the structural model was shown in Figure 4-1. The metabolism of MDZ to 1-OH-MDZ and 4-OH-MDZ were reported to be linear in therapeutic midazolam doses in children[115]; thus, linear metabolism was chosen to describe the formation of 1-OH-MDZ and 4-OH-MDZ rather than Michaelis-Menten equation. The volume of distributions (V) of 1-OH-MDZ and 4-OH-MDZ were not identifiable from our data; accordingly, we fixed these values with the published results after scaling with body weight[116]. The model was implemented in the PREDPP library subroutine “ADVAN6 TRANS1” built in NONMEM. Exponential models were used for interindividual variability, and the proportional plus additive model was used for the residual

error model. The correlations of all the covariates were studied, and the correlation between each covariate was shown in Figure 4-2. After the stepwise forward and backward covariates selection as described in the method section, ALT and creatinine level were selected as the covariates, which significantly improved the goodness of fit and the OFV of the model. The effects of ALT on CL and V were explained by the following equations separately:

$$CL_j = \theta pop_{cj} * (\theta ALT_{cj})^{ALT}$$

$$V_j = \theta pop_{vj} * (\theta ALT_{vj})^{ALT}$$

Where θpop_{cj} and θpop_{vj} were the typical population values of CL and V of j_{th} compound (MDZ, 1-OH-MDZ, 4-OH-MDZ). θALT_{cj} and θALT_{vj} were the estimated influence factor for CL and V of j_{th} compound. The ALT used here was dichotomized to 0 if the ALT level was between 7 IU/L to 56 IU/L and =1 if the ALT level was not in the normal range.

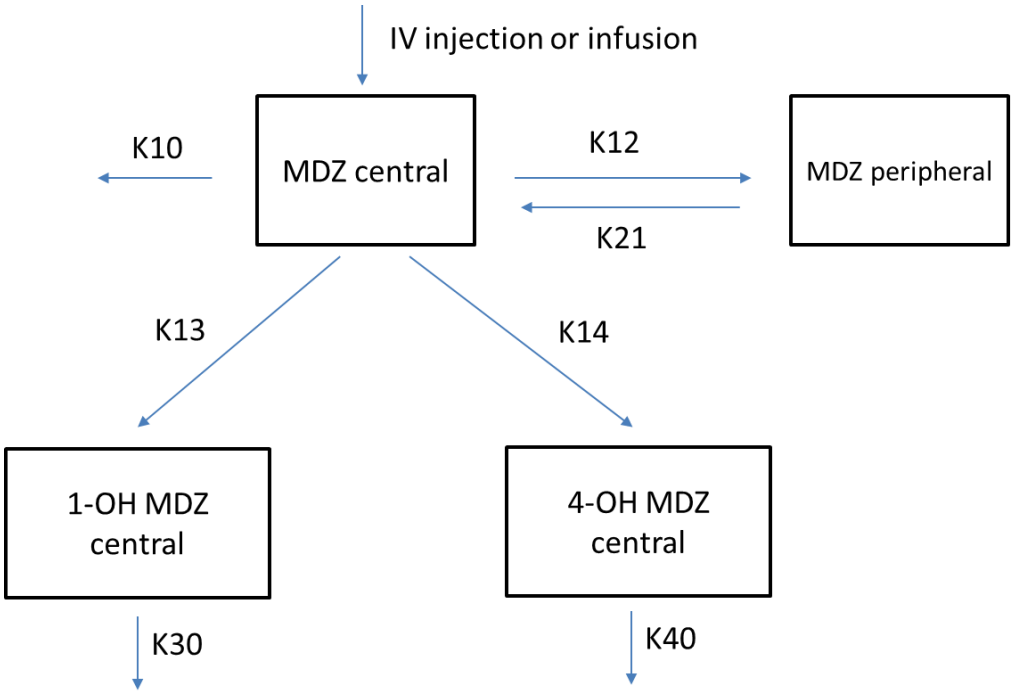

Figure 4-1 Schematic representation of the MDZ and metabolites structural model

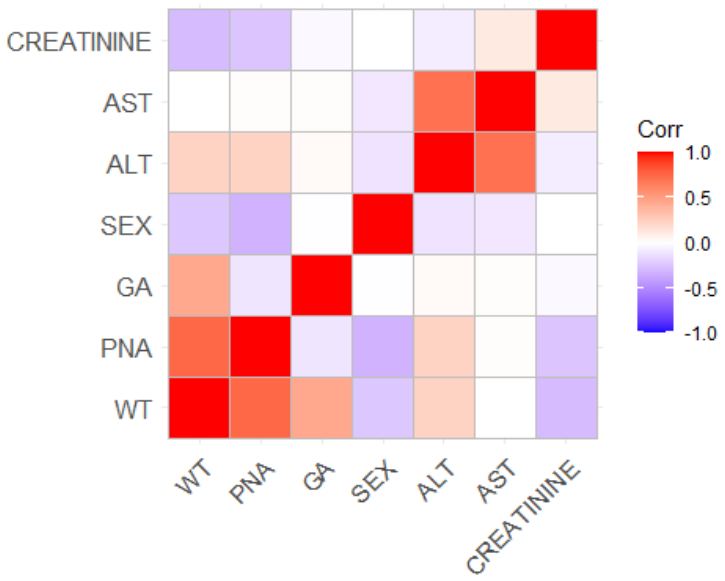

Figure 4-2 Heatmap of correlations between potential covariates of the MDZ PK/PD model

The effects of creatinine levels on CL and V were explained by the following equations separately:

$$CL_j = \theta pop_{cj} * (\theta ALT_{cj})^{Creatinine}$$

$$V_j = \theta pop_{vj} * (\theta ALT_{vj})^{Creatinine}$$

Where θpop_{cj} and θpop_{vj} were the typical population values of CL and V of j_{th} compound (MDZ, 1-OH-MDZ, 4-OH-MDZ). θALT_{cj} and θALT_{vj} were the estimated influence factor for CL and V of j_{th} compound. The creatinine level used here was dichotomized to 0 if the creatinine level was between 0.3 mg/dl to 0.7 mg/dl and =1 if the creatinine level was not in the normal range. The process of model development and OFV changes are shown in Table 4-2.

Table 4-2 Stepwise process of MDZ PK model development

Variable	OFV	Δ OFV	P-Value
No covariates, MDZ = 1 compartment	133.4	NA	<0.01
No covariates, MDZ = 2 compartments	-3541.3	-3674.7	<0.01
+ Increased volume and clearance(MDZ,1-OH-MDZ,4-OH-MDZ) with body weight	-3627.1	-85.8	<0.01
+ Increased clearance(MDZ,1-OH-MDZ,4-OH-MDZ) with ALT	-3711.8	-84.7	<0.01
+ Increased clearance(MDZ, 1-OH-MDZ,4-OH-MDZ) with Creatinine = Final model	-3724.8	-13.0	<0.01

The final estimations of the mean values and inter-individual variability of parameters are summarized in Table 4-3. The observed-versus-population predicted, observed-versus-individual predicted, weighted residual-versus-time, and weighted residual-versus-individual predicted were plotted to assess the goodness-of-fit of the PK models. The model prediction results fit the observed data well for both MDZ (Figure 4-3) and metabolites (Figure 4-4, Figure 4-5).

Table 4-3 Parameter estimation of the MDZ population PK model

Variable	Midazolam		1-hydroxymidazolam		4-hydroxymidazolam	
	Estimation	CV	Estimation	CV	Estimation	CV
Parameter estimates						
CL (L/day/2.7kg)	11.3	13.5%	3.32	22.8%	1.83	61.7%
Q (L/day/2.7kg)	19.5	108.2%	0.28	57.1%	1.03	80.5%
V (L/2.7kg)	0.93	173.0%	6.36 FIX	N.A.	1.18 FIX	N.A.
Peripheral V (L/2.7kg)	3.23	47.6%				
Covariate effects						
Bodyweight on CL	1.16	13.2%	1.16	13.2%	1.16	13.2%
ALT on CL	0.41	19.2%	1.46	18.3%	2.12	18.4%
Creatinine on CL	0.84	14.9%	1.32	12.7%	1.5	22.5%
Interindividual variability						
CL	0.21	25.0%	0.055	89.1%	0.099	62.6%
Residual variability						
Additional	0.002	66.3%				
Proportional	0.25	23.8%	0.53	15.5%	0.58	20.3%

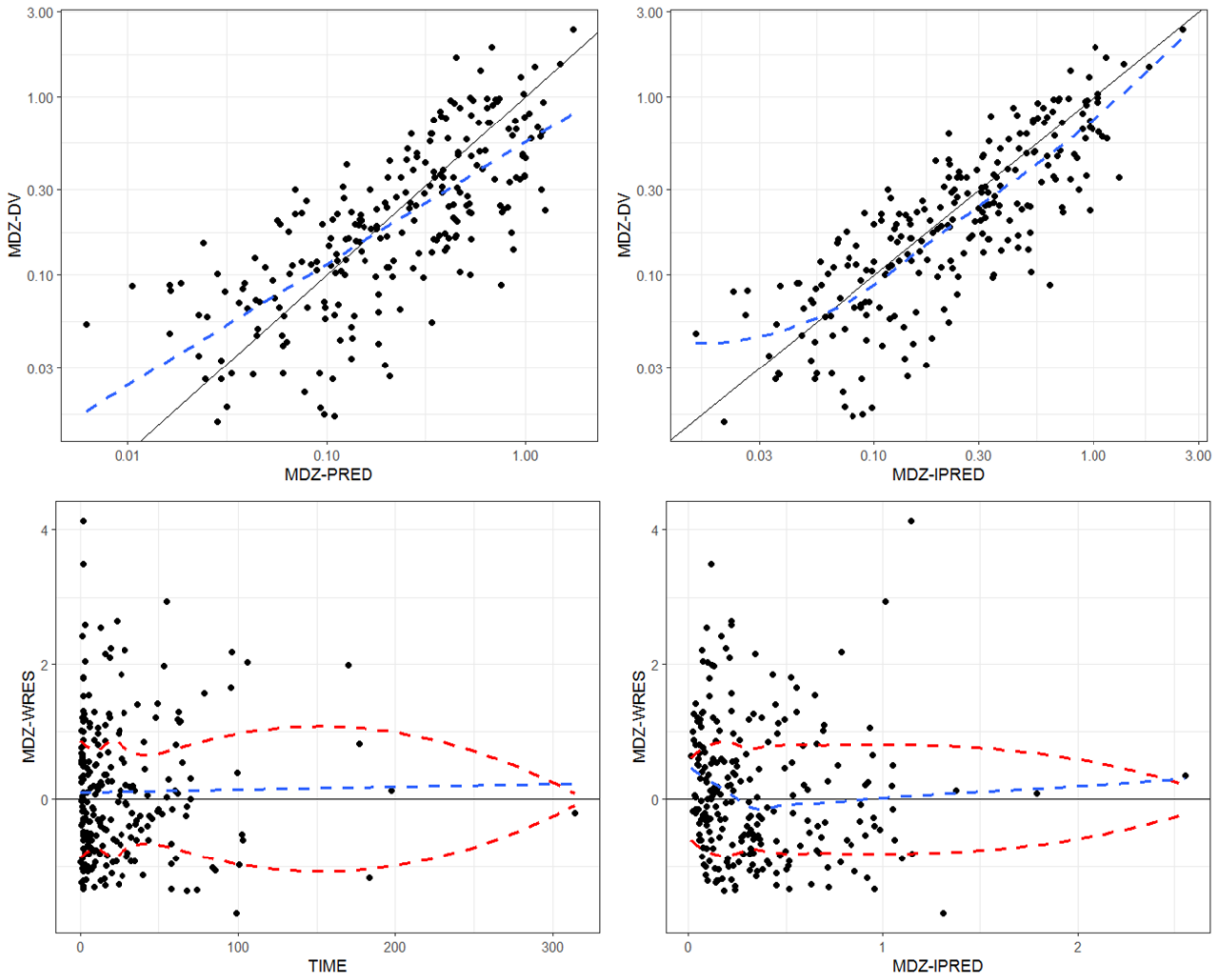

Figure 4-3 Goodness-of-fit plots of MDZ observed data and model prediction The dashed line is the locally weighted scatterplot smoothing.

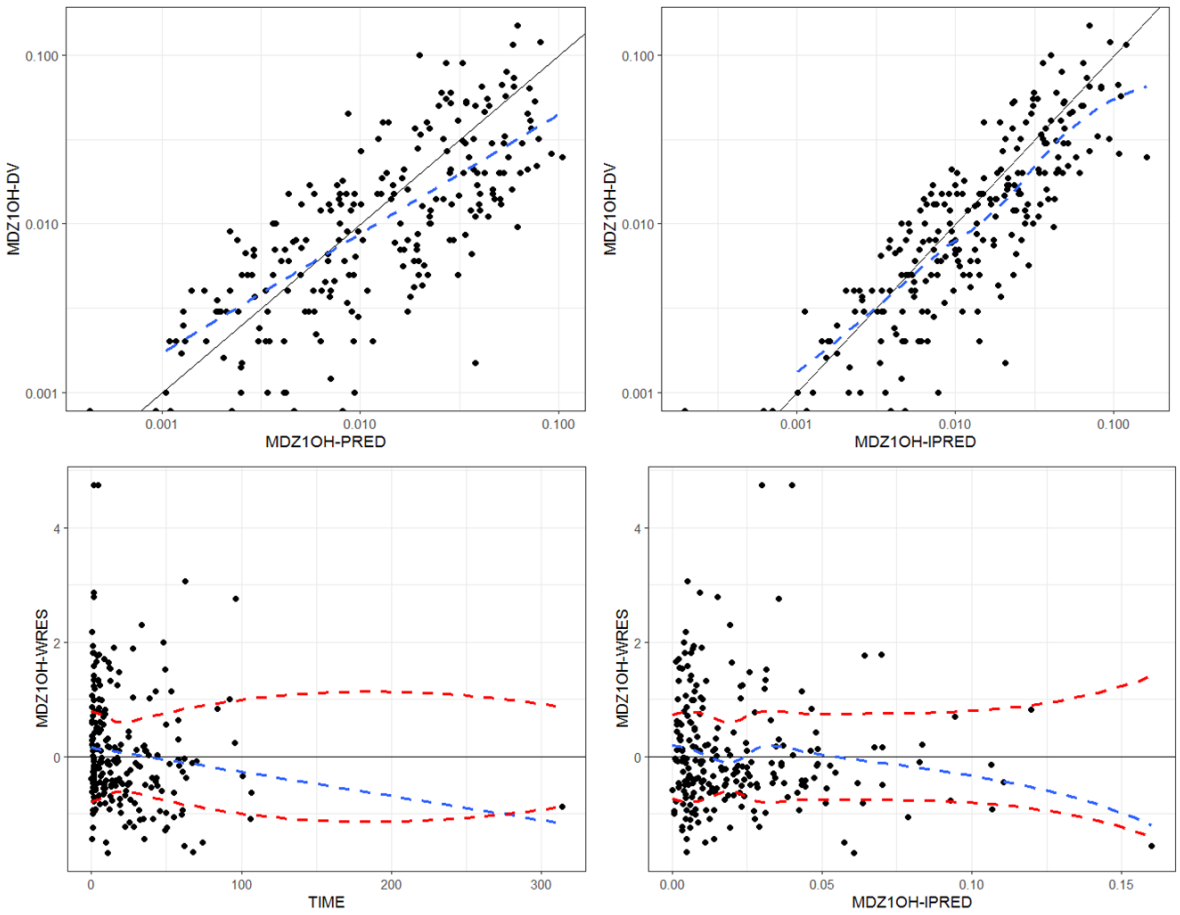

Figure 4-4 Goodness-of-fit plots of 1-OH-MDZ observed data and model prediction The dashed line is the locally weighted scatterplot smoothing.

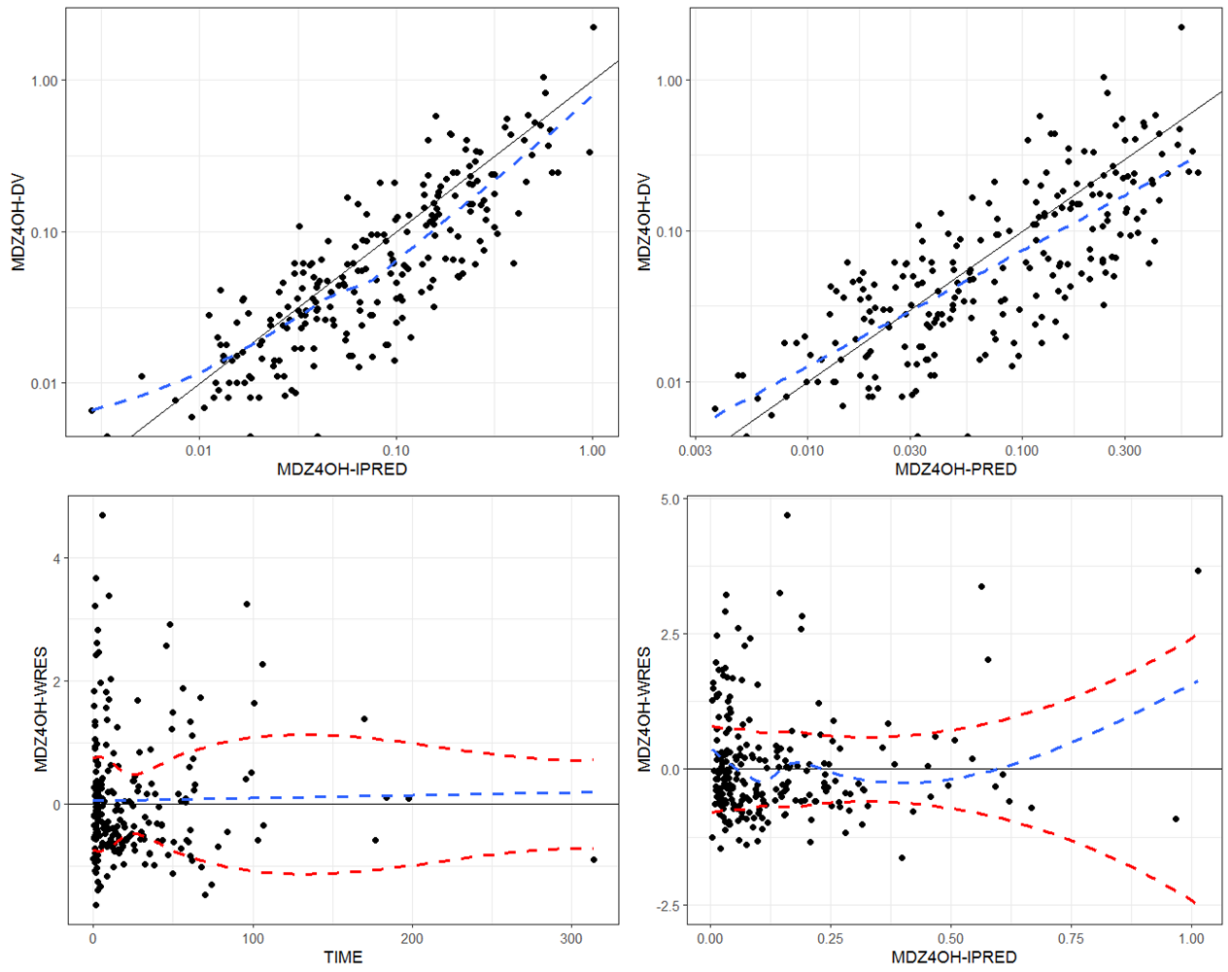

Figure 4-5 Goodness-of-fit plots of 4-OH-MDZ observed data and model prediction. The dashed line is the locally weighted scatterplot smoothing

4.4.3 Population PD modeling

The binary probability model was used as the final PK-PD model, which incorporated the concentrations of MDZ, 1-OH-MDZ, and 4-OH-MDZ. The estimated parameters of the PD model were: EC_{50} = 0.57 µg/ml, γ= 2.12, interindividual variability =0.692 for EC_{50} and 0.74 for γ. Here the EC_{50} is the total concentration of MDZ and its two metabolites. No significant correlation was observed between PK and PD response. The goodness-of-fit plots of the PD model were not shown.

4.4.4 Model evaluation

The standard errors and coefficients of variation showed that the models are robust and the model parameter estimations are acceptable (Table 4-3). The goodness-of-fit plots showed that the simulated MDZ and its metabolites PK data match well with the observed data. The estimated parameters were compared with several published MDZ neonate/pediatric models, as shown in Table 4-4.

Table 4-4 Estimated PK parameters compared with other published models [116-119]

	Our results	Pediatric population [1]	Neonate population [2]	Neonate population [3]	Premature infant population[4]
MDZ central clearance (L/hour)	11.3	36.6	0.47	0.132	0.074
MDZ intercompartment clearance (L/hour)	19.5	43.8	0.51	1.1	0.59
MDZ central volume of distribution (L)	0.93	42	4.29	0.5	0.82
MDZ peripheral volume of distribution (L)	3.23	160	14.6	0.607	1.04
1-OH-MDZ clearance (L/hour)	3.32	222	1.38	N.A.	N.A.
1-OH-MDZ volume of distribution (L)	6.36 FIX	72	10.2	N.A.	N.A.
4-OH-MDZ clearance (L/hour)	1.83	35.4	N.A.	N.A.	N.A.
4-OH-MDZ volume of distribution (L)	1.18 FIX	13.4	N.A.	N.A.	N.A.

4.5 Discussions

In the present study, a two-compartment population PK model was built to describe the PK profiles of MDZ, 1-OH-MDZ, and 4-OH-MDZ in the neonate population. The PK parameters were standardized by patients' body weights. Covariates, including ALT and creatinine, were incorporated into the PK model to explain the inter-individual variability. Goodness-of-fit plots showed our predicted PK profiles matched well with the observed values.

We predicted MDZ PD response using a binary probability model but did not observe a significant concentration-effect relationship in the neonate population.

When incorporating ALT and creatinine as covariates in our PK model, we regarded them as categorical rather than continuous variables because the ALT or creatinine levels are not in direct proportion to the liver or renal function in neonates. The prediction would be biased by some extreme values if the exact ALT or creatinine levels were used. Besides ALT and creatinine levels, some other covariates, such as AST, GA, and PMA, were also tested but did not significantly improve the PK model. Usually, PK parameters in the neonate population are very sensitive to age. However, in our study, the incorporation of age as a covariate made the model unstable and difficult to converge. This observation could be due to the complex disease states of neonates in NICU and the large age variation (from several hours old to 2 years old).

For the prediction of PD response, it is a common practice that, when the response is categorical data like a pain scale, the prediction will be made to estimate the probability of each category under a given drug plasma concentration. Unfortunately, in our study, the number of samples in each PD response category is not balanced, with over 90% of samples having a mean N-PASS score of less than 3. Thus, it will be less meaningful to predict the probability of some categories with very few or even no samples. To handle this issue, we transformed the PD data to two categories: MDZ responders (N-PASS<3, PD=0) and not responders (N-PASS >3, PD=1) according to the goal of pain treatment/intervention in clinic(N-PASS<3). By dichotomizing the PD data, we not only simplified the PD model, but also matched the clinical assessment of MDZ treatment in neonates.

To date, no significant concentration-effect relationship for midazolam has been found in the neonate population. Many papers have reported the PK-PD inconsistency in the neonate

population[112-114], and none of the studies incorporated 4-OH-MDZ into their PK/PD model. 4-OH-MDZ concentrations are usually lower than 1-OH-MDZ in pediatric and adult populations due to the diminishing CYP3A7 expression during maturation. However, 4-OH-MDZ concentrations were much higher than 1-OH-MDZ in our neonatal population (Figure 4-6). This can be explained by the young postnatal age of our subjects (average= 8.5 weeks); during that time, the activity of CYP3A7 is still high. We hypothesized that the incorporation of 4-OH-MDZ concentrations in our PK/PD model would improve the prediction of PD response and explain the reported PK-PD inconsistency. Even though 4-OH-MDZ did not significantly improve the PD prediction performance in the study, the contribution of 4-OH-MDZ to PD response needs further investigation.

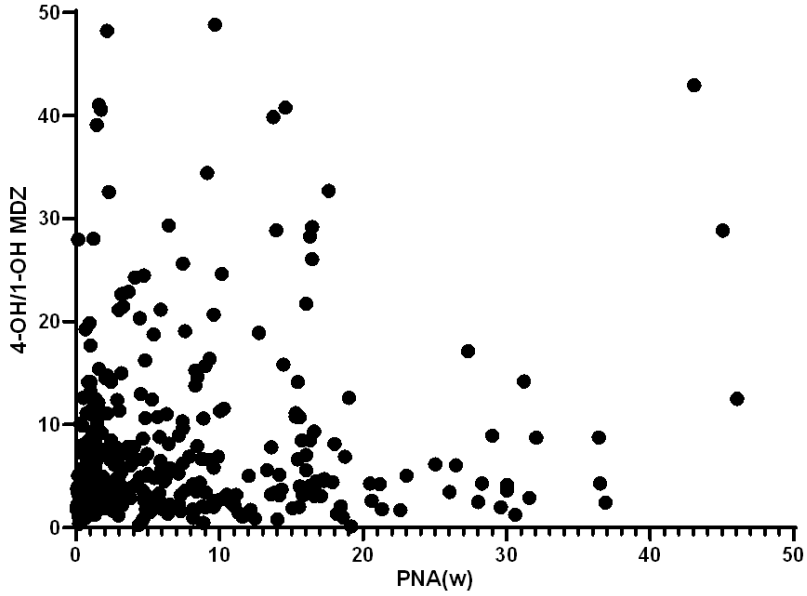

Figure 4-6 Observed concentration of 4-OH-MDZ and 1-OH-MDZ.The Y-axis shows the concentration ratios of 4-OH-MDZ to 1-OH-MDZ, and the X-axis represents the postnatal ages of the patients.

Differences in the estimated PK parameters between MDZ population PK studies among different patient populations were observed (Table 4-4). For MDZ central clearance, our prediction value is 11.3 L/hour, while the value was 36.6 L/hour in the pediatric population from the Zuppa et al. study. This discrepancy could be explained by the differences between the neonatal and pediatric populations. Moreover, for the neonatal population, the parameter estimations are different between studies. For example, we estimated the volume of distribution of MDZ in the central compartment to be 0.93 L, while in other neonate studies, it was reported to be 4.29L[117], 0.5L [118], and 0.82L [119]. The inter-study variability still exists even though the difference in body weights was taken into consideration.

The opportunistic sampling strategy enabled us to collect a large set of samples during a short period of time without imposing additional burdens on study subjects; however, it also greatly increased the complexity of PK data analysis. For example, the sample numbers of an individual patient varied from 1 to 32, and the time intervals between sampling within a subject ranged from several hours to over 1 year; the dosing regimens were different within the study subjects and changed with the patients' body weight. The very sparse PK sampling complicated the data exploratory data analysis, and the commonly used exploratory plots (e.g., DV vs. time, DV vs. dose) were unable to be drawn, which limited our ability to screen out outliers and abnormal data points. Additionally, 1-OH-MDZ and 4-OH-MDZ can be further metabolized by UDP-glucuronosyltransferase (UGT) to 1-hydroxymidazolam glucuronide (1-OH-MDZ -Glu) and 4-hydroxymidazolam glucuronide (4-OH-MDZ -Glu), respectively. We did not include the glucuronide metabolites in our study since they are not pharmacologically active [120]. However, it was reported that both 1-OH-MDZ-Glu and 4-OH-MDZ-Glu could be converted back to 1-OH-MDZ and 4-OH-MDZ by β-glucuronidase [120]. This will affect the PK profiles

of both MDZ metabolites and should be considered. Moreover, a simplified binary probability model was applied to predict PD response due to the imbalanced categorical PD data. A more sophisticated PD model with probability prediction of individual N-PASS score could be used when PD data are ample and balanced. For future work, neonates could be stratified according to their disease states, age, and co-administrated drugs, and PK parameters are then estimated for each stratified population for a better prediction. Furthermore, different PD models could be tested to explore the concentration-effect relationship for MDZ in the neonate population.

Chapter 5 Machine Learning Assisted Population PD Study of Midazolam in Neonatal Patients

5.1 Abstract

Machine learning-based modeling is commonly used in precision medicine research. In the current study, we developed six machine learning models (K Nearest Neighbor, Support Vector Machine, Decision Tree, Random Forest, Naïve Bayes, and Neural Network) in python to predict the PD response (N-PASS score) to midazolam treatment in neonates. Models were trained using a training dataset, and the hyper parameters of all the models were tuned using grid search. The final prediction performance of each model was evaluated using a testing dataset. With the accuracy = 0.83, precision = 0.98, and area under the receiver operating characteristic curve = 0.81, the random forest classifier had the best prediction performance of PD response for our current dataset. Postmenstrual age, birth weight, and dosing weight are the top 3 most important features for the random forest classifier. Our ML-based modeling enables midazolam PD response prediction without a PK model as a prerequisite, and this approach can also be used for other medications.

5.2 Introduction

Machine learning (ML) is a statistical technique for fitting models to data and to ‘learn’ by training models with data [121]. The purpose of ML is to construct computer programs that automatically improve the accuracy of their output with experience. ML algorithms use sample

data (also known as a training dataset) for training computational models to generate predictions that will fit the sample data [122]. Usually, the model prediction performance will be evaluated by another independent dataset called testing dataset [123]. ML approaches can be classified into three major types: (1) reinforcement learning: models are trained to fulfill tasks and will be rewarded for good actions and punished for bad operations. (2) unsupervised learning: methods aim to unravel underlying complex structures in the data and enable to reason about these patterns. (3) supervised learning: Used labeled data to find connections between input variables and outcomes [124].

Nowadays, ML prediction is commonly used to guide clinical decisions in various contexts, including pre-clinical solution (PCS); recommendation system (RecSys); computer-aided detection system (CADe); computer-aided diagnosis system (CADx); and early warning system (EWS)[125]. PCSs is aimed at creating the infrastructure that is subsequently utilized by downstream analytical tools. RecSys individualize medical, pharmacological, or dietary recommendations for a patient. CADe is an ML system that assists physicians in interpreting medical detection results, while CADx provides a more-structured diagnosis of a given image [126]. EWS produces warning information to help patients prepare and proactively respond in advance to a specific risk.

Precision medicine is one of the most common applications of machine learning in healthcare. Unlike the conventional one-size-fits-all paradigm, precision medicine predicts what treatment protocols are likely to succeed in a patient based on various patient attributes and the treatment context [127]. The underlying assumption here is that individualized healthcare will yield higher efficacy and lower rates of adverse outcomes [128].

As described previously, PK/PD modeling is a set of mathematical expressions that integrates a pharmacokinetic model with a pharmacodynamic model to describe the time course of effect intensity in response to drug dose [129]. PK/PD modeling is commonly used to predict the individualized dose and therapeutic response in precision medicine. However, PK/PD model development is an iterative, empirically guided process that relies on principles of pharmacology and physiology to quantitatively represent the system [130]. The quality of the model heavily depends on the developer's knowledge and experience [131]. Moreover, due to the advances in high-throughput bioanalysis and electric health record system, massive amounts of data are being generated and ready for use by PK/PD modeling [132]. These developments generated an ever-expanding data landscape that pharmacometrics research should navigate.

There is an increasing interest in incorporating ML techniques in population PK/PD modeling. For example, neural network methods were used to predict the peak and trough plasma concentrations of gentamycin [133], tobramycin [134], and arbekacin [135] in population PK studies. Tang et al. compared 8 different ML methods to investigate the dose-response relationship of tacrolimus [136]. ML methods were also applied in the population PK/PD modeling of digoxin [137] and remifentanil [138] to predict the initial doses and PD responses.

In this study, we collected midazolam PK and PD data from 565 neonatal samples. Six different ML techniques were investigated to predict the PD response, with numerous patient demographic information, lab results, and co-administrated drug concentrations incorporated as model features. The prediction performances of the six ML models were compared to identify the most suitable model for our dataset.

5.3 Materials and Methods

5.3.1 Patients

The patient recruitment and study design were described in the method section of chapter 4. The demographic information of the subjects was obtained from their electronic health record through MiChart and the Data Direct system.

5.3.2 Data processing

Drug plasma concentration and patient demographic information were processed as the variables of the machine learning model. The plasma concentrations of morphine, midazolam, and their metabolites were determined by the LC-MS/MS method as described in chapter 3. For patient demographic information, gender was set to 0 for females and 1 for males. Race = 0 for white subjects, 1 for black patients, and 2 for other races. Other variables like postnatal ages (PNA), postmenstrual age (PMA), gestational age (GA), birth weight, dosing weight, level of alanine aminotransferase (ALT), level of aspartate aminotransferase (AST), level of creatinine (CREAT), the plasma concentration of morphine (Morphine), morphine-3-glucuronide (M3G), morphine-6-glucuronide (M6G), midazolam (Midazolam), 1-hydroxymidazolam (1-hydroxymidazolam), 4-hydroxymidazolam (4-hydroxymidazolam) were processed as numerical data. The mean and standard deviation (SD) of all numerical variables are listed in Table 5-1.

Table 5-1 Means and standard deviations of all numerical variables

Variables	Mean	SD
Bodyweight at dosing (kg)	2.74	1.34
Postnatal Age (week)	8.48	11.60

Gestational Age (week)	33.52	5.60
Bodyweight at birth (kg)	1.89	1.10
ALT (iu/l)	71.76	122.90
AST (iu/l)	100.22	260.69
Creatinine (mg/dl)	0.40	0.26
Morphine (ng/ml)	118.16	237.15
M3G (ng/ml)	148.7	315.0
M6G (ng/ml)	87.35	126.4
Midazolam (ng/ml)	316.92	536.15
1-hydroxymidazolam (ng/ml)	21.07	52.76
4-hydroxymidazolam (ng/ml)	104	180.5

The PD response to midazolam treatment was assessed via the neonatal pain, agitation, and sedation scale (N-PASS), which combines the assessment of pain, agitation, and sedation levels in a critically ill infant with acute and/or ongoing pain. The total pain score is documented as a positive number from 0 to 10, as shown in Table 5-2. The goal of pain treatment and intervention is N-PASS < 3. In our study, the N-PASS value was calculated as the mean of all N-PASS within 24 hours. The N-PASS variables were set to 0 (responder) if the actual N-PASS value were less than 3 and set to 1 (responder) if N-PASS is over 3 in our final datasets.

Table 5-2 Neonatal Pain, Agitation, and Sedation Scale (N-PASS) [139]

Assessment Criteria	Sedation		Normal	Pain / Agitation	
	-2	-1	0	1	2
Crying Irritability	No cry with painful stimuli	Moans or cries minimally with painful stimuli	Appropriate crying Not irritable	Irritable or crying at intervals Consolable	High-pitched or silent-continuous c Inconsolable
Behavior State	No arousal to any stimuli No spontaneous movement	Arouses minimally to stimuli Little spontaneous movement	Appropriate for gestational age	Restless, squirming Awakens frequently	Arching, kicking Constantly awake or Arouses minimally / movement (not seda
Facial Expression	Mouth is lax No expression	Minimal expression with stimuli	Relaxed Appropriate	Any pain expression intermittent	Any pain expression continual
Extremities Tone	No grasp reflex Flaccid tone	Weak grasp reflex ↓ muscle tone	Relaxed hands and feet Normal tone	Intermittent clenched toes, fists or finger splay Body is not tense	Continual clenched t fists, or finger spla Body is tense
Vital Signs HR, RR, BP, SaO_2	No variability with stimuli Hypoventilation or apnea	< 10% variability from baseline with stimuli	Within baseline or normal for gestational age	↑ 10-20% from baseline SaO_2 76-85% with stimulation – quick ↑	↑ > 20% from baselir $SaO_2 \leq 75\%$ with stimulation – slow ↑ Out of sync with ver

To handle the missing data in our dataset, the K-Nearest Neighbor method-based imputation was utilized to complete the missing values. Each sample's missing values were imputed with the mean value from n nearest neighbors. To avoid the influence of extremely high or low values, all the features in the dataset were scaled to the range of 0 to 1 with the MinMax scaler method from Sklearn packages. Our dataset with a total of 565 samples was then split into training and testing datasets for ML classifier. About 2/3 of the data (n= 377) were used as training data, and 1/3 were used as testing data (n = 188). Data were stratified prior to data splitting; thus, the variable distributions are balanced between the training and testing datasets.

5.3.3 Model building

Six ML classifiers were utilized to predict the PD response, which include K Nearest Neighbor (KNN), Support Vector Machine (SVM), Decision Tree (DT), Random Forest (RF), Naïve Bayes (NB), and Neural Network (NN). The hyper parameters of each classifier were optimized by grid search with K fold cross validation (k=5). For the K fold cross validation, the training dataset is split into k smaller sets, the model is trained using k-1 of the folds as training data, and the resulting model is validated on the remaining fold of the data. The average values

computed in the loop were reported as the performance measurements. All analyses in this study were implemented using Python (Version 3.10) with related packages or our custom written functions.

5.3.4 Model evaluation

To evaluate the prediction performance, the accuracy, precision, recall, and f1 value of each optimized model classifier were calculated. The Precision-Recall Curve (PRC), Receiver Operating Characteristic Curve (ROC), and Area under the ROC curve were compared between the models. Feature importance was also measured for some classifiers to investigate the influence of features on model prediction performance.

5.4 Results

5.4.1 K Nearest Neighbor (KNN) classifier

After grid search for the best hyper parameter combination, the optimized hyper parameters of KNN classifier with the best f1 score are: number of neighbors (n_nerighbors) = 3; weight function used in prediction metric is ‘distance’; algorithm used to compute the nearest neighbors is ‘auto’; the distance metric to use is ‘Manhattan’; other hyper parameters are default values in the sklearn.neighbors.KNeighborsClassifier packages. The performance of optimized KNN classifier was verified on the testing dataset, the confusion matrix was calculated and the accuracy = 0.84, precision = 0.69, recall rate = 0.31, f1 score = 0.42. The Precision-Recall curve of the model is shown in Figure 5-1 with thresholds from 0 to 1. The KNN Receiver Operating Characteristic (ROC) Curve was plotted (Figure 5-2), and the area under the ROC curve was 0.72, indicating that there is a 72% chance that the model will be able to distinguish between

positive class and negative class. The importance of each feature in KNN model was evaluated using feature permutation, and the results are shown in Figure 5-3. Gestational age, dosing weight, and birth weight are the features with the highest importance in the KNN model.

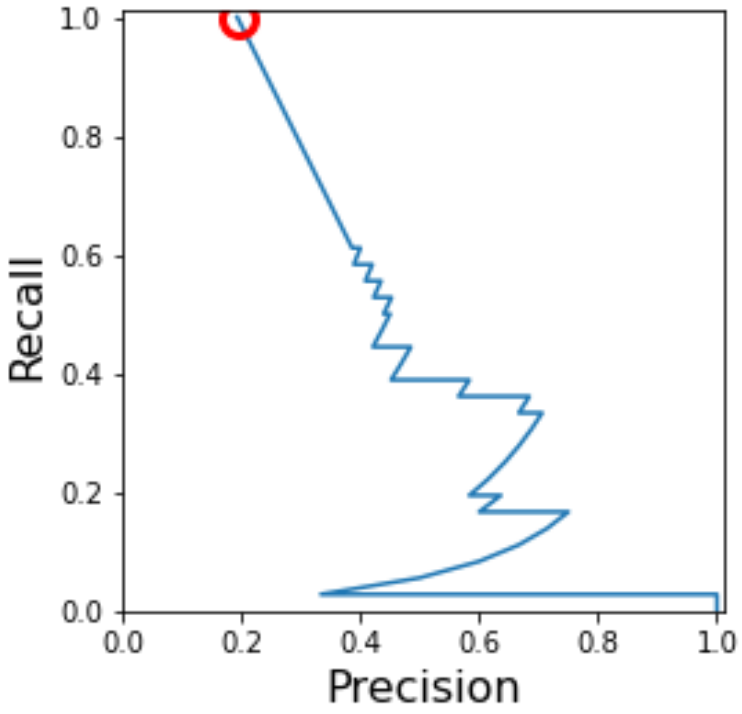

Figure 5-1 Precision-Recall Curve of KNN classifier

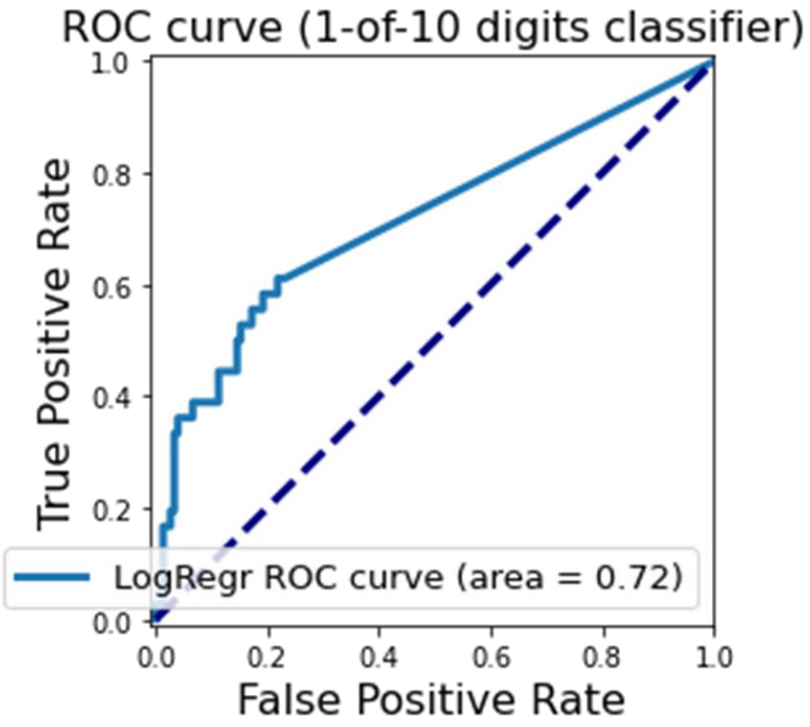

Figure 5-2 Receiver Operating Characteristic Curve of KNN classifier

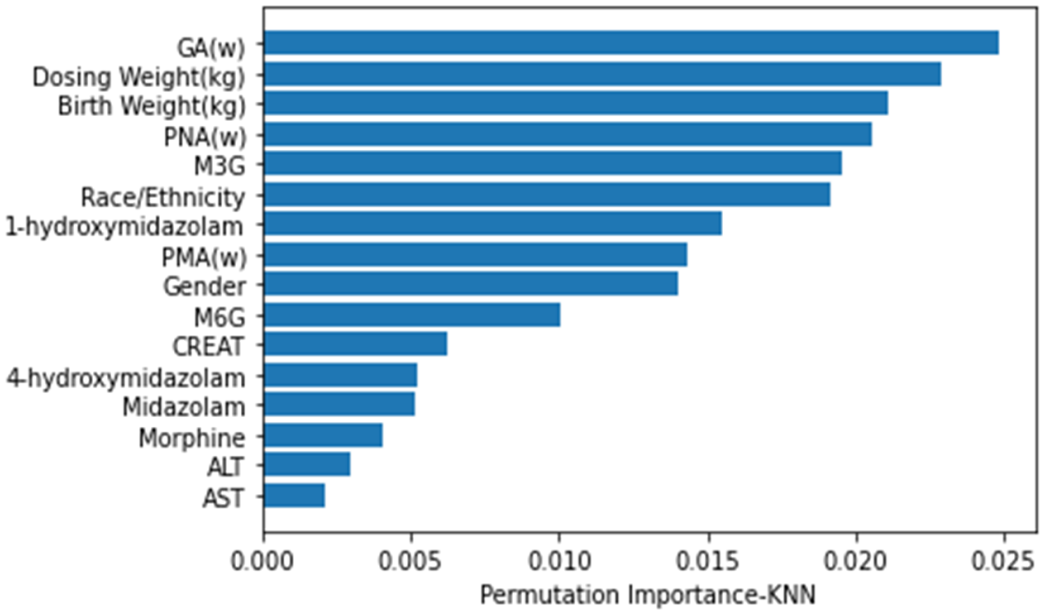

Figure 5-3 Permutation feature importance of KNN classifier

5.4.2 Support vector machine (SVM) classifier

For SVM classifier, the best hyper parameters combination after grid search are: regularization parameter (C) = 6; kernel = 'polynomial', degree of the polynomial kernel function (degree) = 2; Kernel coefficient for polynomial kernel (gamma) = 10; other hyper parameters are default values in the sklearn.svm.SVC packages. Confusion matrix was used to evaluate the prediction performance of the optimized SVM model on the testing dataset, the accuracy = 0.78, precision = 0.37, recall = 0.19, f1 score = 0.25. To evaluate the trade-off between precision and recall for different thresholds, a Precision-Recall curve was plotted (Figure 5-4). The ROC curve of SVM model is shown in Figure 5-5, with the area under the ROC curve of 0.56, indicating a 56% chance that the model will be able to distinguish between positive class and negative class.

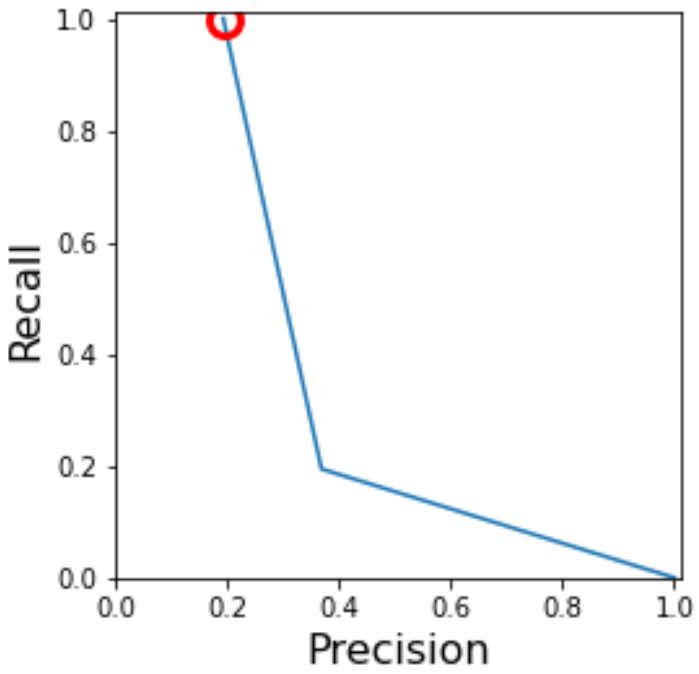

Figure 5-4 Precision-Recall Curve of SVM classifier

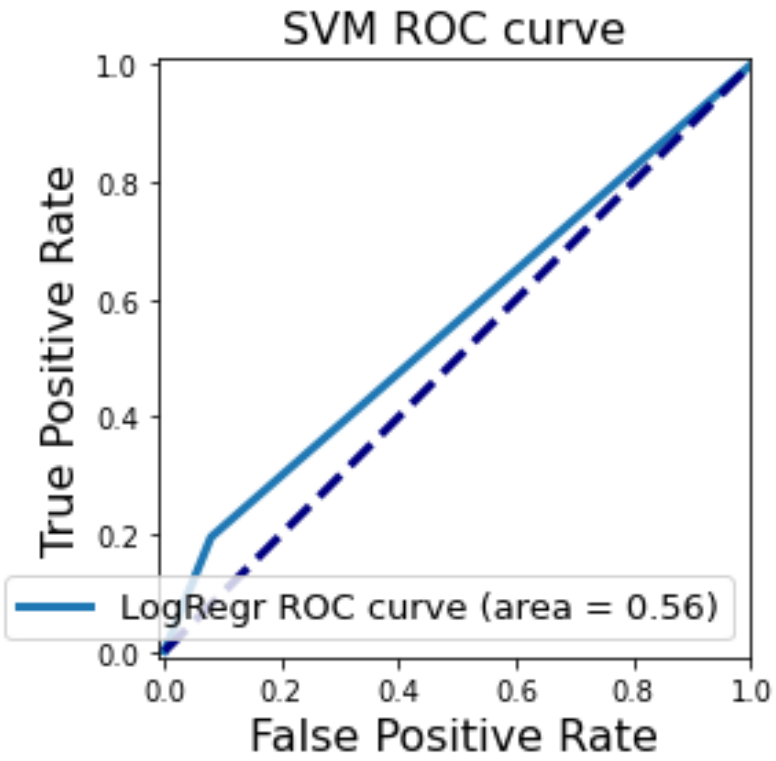

Figure 5-5 Receiver Operating Characteristic Curve of SVM classifier

5.4.3 Decision Tree (DT) Classifier

Grid search for the best hyper parameter combinations was conducted as previously described; the hyper parameters of DT model with the best f1 score are as follows: the function to measure the quality of a split (criteria) = 'entropy'; the strategy used to choose the split at each node = 'best', which chooses the best split; the number of features to consider when looking for the best split (max_features) = 9. Other parameters are the default values of the sklearn.tree.DecisionTreeClassifier package. The prediction performance of the optimized DT model was verified on the testing dataset. Confusion matrix was calculated with accuracy = 0.74, precision=0.36, recall = 0.38, and f1 score = 0.38. The Precision-Recall curves and ROC curves

of the optimized DT model on the testing dataset are shown in Figure 5-6 and Figure 5-7. The area under the ROC curve equals 0.62.

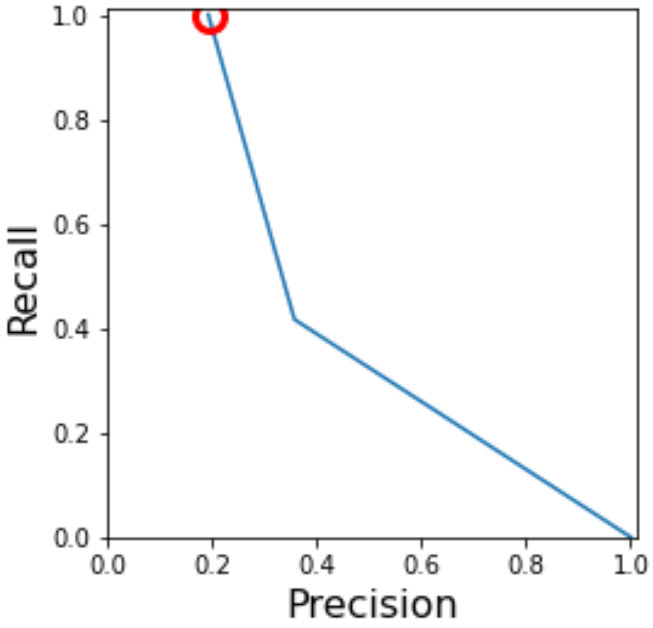

Figure 5-6 Precision-Recall Curve of DT classifier

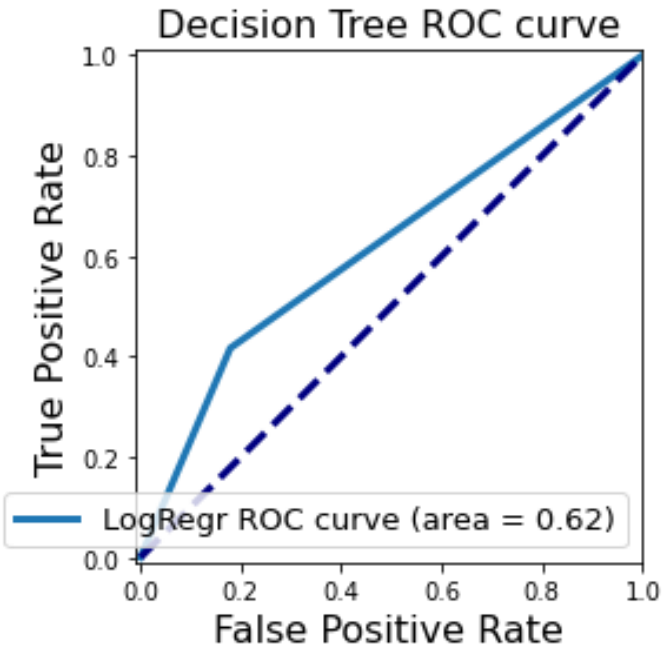

Figure 5-7 Receiver Operating Characteristic Curve of DT classifier

5.4.4 Random Forest (RF) classifier

After grid search for the best hyper parameter combination, the optimized hyper parameters of the RF classifier with the best f1 score are: the function to measure the quality of a split (Criterion) = 'gini'; the number of trees in the forest (n_estimators) = 100; the number of features to consider when looking for the best split (max_features) = 7; the minimum number of samples required to be at a leaf node (min_samples_leaf) = 1; the minimum number of samples required to split an internal node (min_samples_split) = 6. Other hyper parameters are the default values of the sklearn.ensemble.RandomForestClassifier package. The performance of optimized RF classifier was verified on the testing dataset, and the confusion matrix was calculated (accuracy = 0.83, precision = 0.98, recall rate = 0.14, f1 score = 0.24). The Precision-Recall curve of the model is shown in Figure 5-8, with the threshold from 0 to 1. The ROC Curve was plotted (Figure 5-9), and the area under the ROC curve was 0.81, which indicates an 81% chance that the model will be able to distinguish between positive class and negative class. The importance of each feature in the RF model was studied using feature permutation, and the results are shown in Figure 5-10, indicating that PMA, birth weight, dosing weight are the features with the highest importance in the RF model.

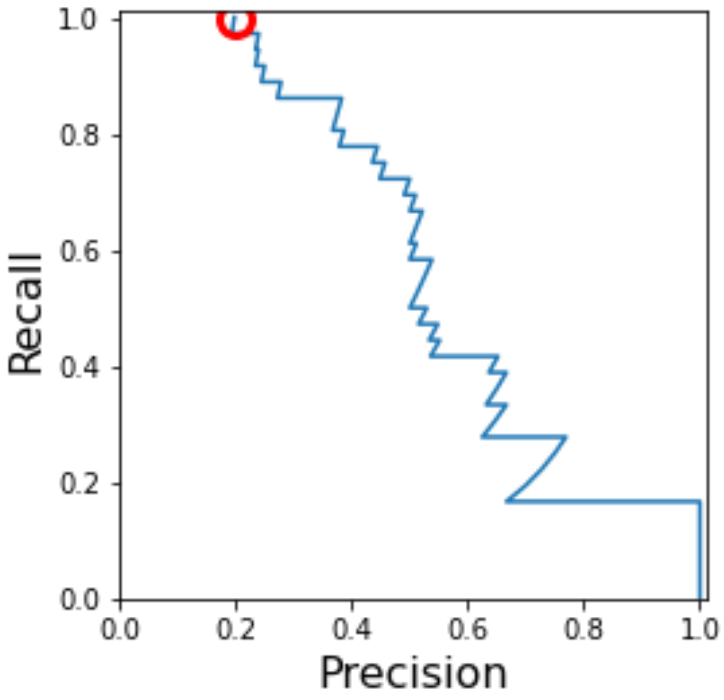

Figure 5-8 Precision-Recall Curve of RF classifier

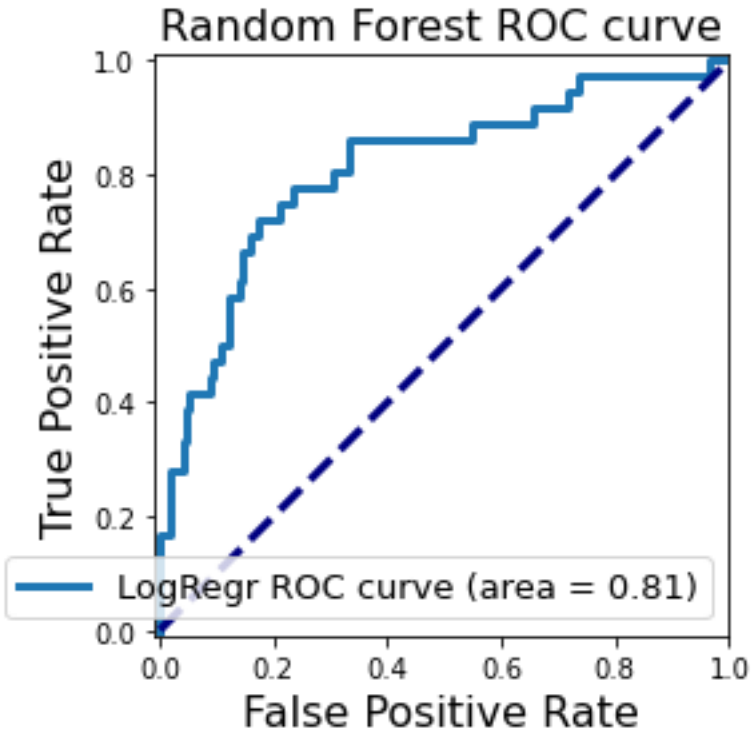

Figure 5-9 Receiver Operating Characteristic Curve of RF classifier

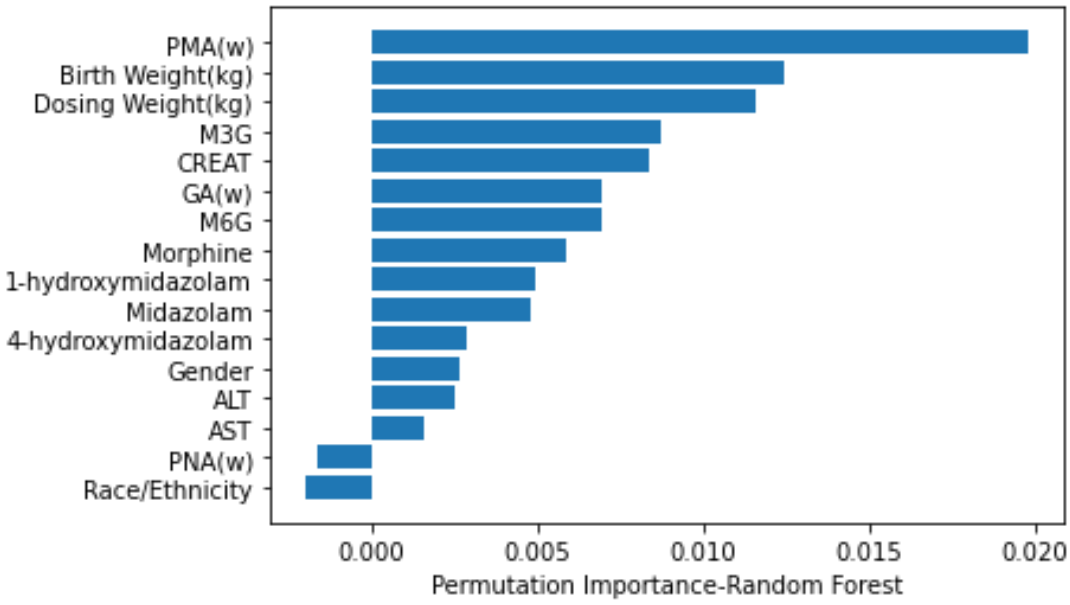

Figure 5-10 Permutation feature importance of RF classifier

5.4.5 Naïve Bayes (NB) classifier

For the NB classifier, the best hyper parameter combination after a grid search is: Prior probabilities of the classes (priors) = 'None'; Portion of the largest variance of all features that is added to variances for calculation stability (var_smoothing) = 1e-9. Other hyper parameters are default values in the sklearn.naive_bayes.GaussianNB package. Confusion matrix was used to evaluate the prediction performance of the optimized NB model on the testing dataset, and the results are as follows: accuracy = 0.53, precision = 0.22, recall = 0.56, f1 score = 0.31. To evaluate the trade-off between precision and recall for different thresholds, Precision-Recall curve was plotted (Figure 5-11). The ROC curve of NB model is shown in Figure 5-12, with the area under the ROC curve = 0.55, indicating a 55% chance that the model will be able to distinguish between positive class and negative class.

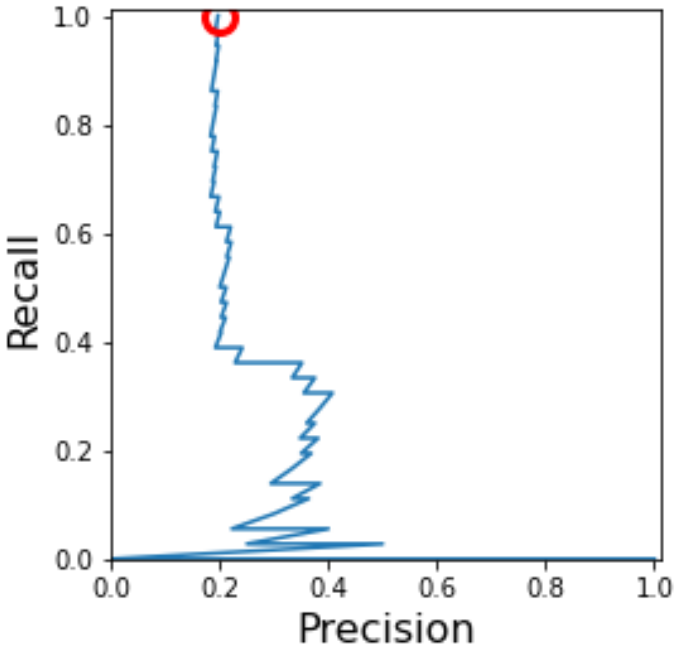

Figure 5-11 Precision-Recall Curve of NB classifier

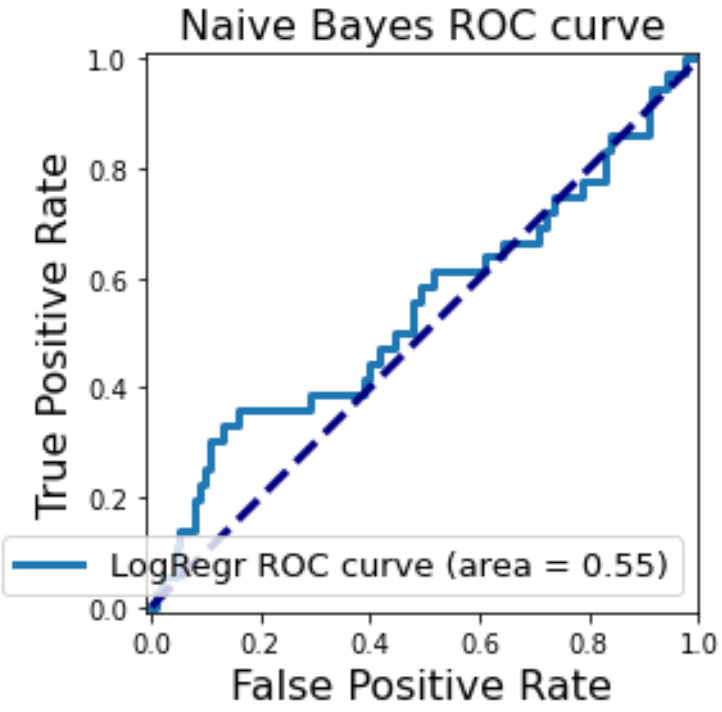

Figure 5-12 Receiver Operating Characteristic Curve of NB classifier

5.4.6 Neural Network (NN) Classifier

A grid search for the best hyper parameter combinations was conducted as previously described, the hyper parameters of the NN model with the best f1 score are as follows: hidden layer size = 1000; activation function for the hidden layer = 'relu' (the rectified linear unit function); the solver for weight optimization = 'lbfgs' (an optimizer in the family of quasi-Newton methods); alpha (L2 regulation item) = 0.0001; learning rate schedule for weight updates = 'constant'; maximum number of iterations (max_iter) = 1000. Other parameters are the default values of the sklearn.neural_network.MLPClassifier package. The prediction performance of the optimized NN model was verified on the testing dataset. Confusion matrix was calculated with accuracy = 0.80, precision=0.45, recall = 0.28 and f1 score = 0.34. The Precision-Recall curves and ROC curves of the optimized NN model on the testing dataset are shown in Figure 5-13 and Figure 5-14. The area under the ROC curve equals 0.64.

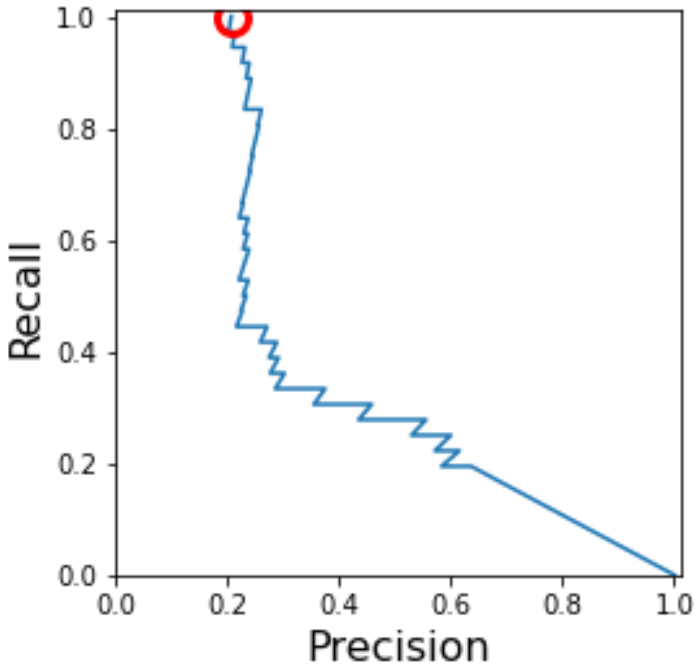

Figure 5-13 Precision-Recall Curve of NN classifier

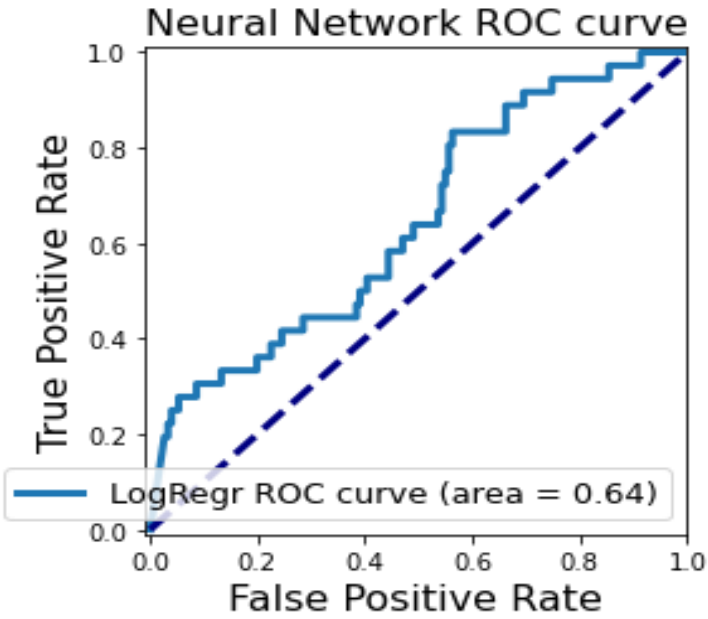

Figure 5-14 Receiver Operating Characteristic Curve of NN classifier

5.5 Discussion

In the ML-assisted population PD study, six ML classifiers were developed and optimized. The same testing dataset was used to compare the prediction performance between the classifiers. KNN and random forest classifier had comparable accuracy (0.84), while the precision of random forest was higher than KNN (0.98 vs. 0.69). The naïve Bayes classifier demonstrated the highest recall value (0.56), and KNN exhibited the highest f1 scores (0.42) among the six classifiers. The recall values were low in most of our models, which indicates some neonate patients with abnormal PD responses may be missed by our prediction. Considering the precision-recall curve and ROC curve results of the classifiers, the random forest model showed the best area under the ROC curve (0.81).

The feature importance analysis of the KNN and random forest models revealed that, in both models, the dosing weight, birth weight, PMA, and GA are the most important features for prediction. Those are fundamental covariates but are usually not as vital as drug concentration

regarding their influence on PD response. However, considering our study subjects are neonates, whose physiological conditions and drug PK profiles are very sensitive to the changes in age and body weight, the result of the feature importance analysis is not surprising. Further clinical studies are needed to verify these findings.

ML has been well recognized to be data-hungry and requires a large quantity of data [140]. However, the sample sizes are small for many clinical studies because of the high costs of data acquisition and inherent challenges of clinical research [141]. Thus, ML methods might not be suitable for many clinical studies. An opportunistic sample collection strategy was used in our study. We obtained residual blood samples originally collected for routine clinical care, which did not impose additional burdens on study subjects. Compared to other neonatal studies, our sample size is larger and, thus, is more appropriate for ML-based analysis. Moreover, besides the drug concentration data obtained from our PK analysis, other data, including patient demographic information and lab results, were retrieved from the electric health record system, which greatly expanded the features available for machine learning analysis.

Unlike traditional PK/PD modeling, which usually first establishes a PK model and then links the PK model to PD response [142], ML-based modeling does not need a PK model as a prerequisite. In our study, PD responses were predicted using different ML classifiers, and the prediction performance of the classifiers could then be conveniently evaluated and compared. Moreover, various covariates could be easily incorporated into the ML models as features to improve PD prediction. In classic PK/PD modeling, each covariate needs to be manually evaluated with the stepwise selection to determine if the covariate should be added to the structure model, which is tedious and time-consuming. As a comparison, in an ML-based model, covariates are easily incorporated with less restriction. This is particularly useful in PK/PD

studies involving high-throughput data (e.g., metabolomics, genomics, and proteomics) since those multi-omics data are too complex to be incorporated into a classic PK/PD model as covariates.

Whilst our ML models demonstrated their capability in dealing with numerous covariates and predicting PD response; the study has some limitations. Firstly, the PD responses are imbalanced in our samples. For the 565 samples, 472 of them have PD response = 0 (responders) while only 93 of them with PD = 1 (non-responders). This is expected because the goal of midazolam treatment is to alleviate neonate pain and agitation symptoms. However, this imbalanced dataset may have caused prediction bias during the development and validation of the ML models [143]. In addition, it is difficult to mechanistically understand the ML-based models and the prediction results from a clinical perspective. For example, we do not fully understand why some covariates such as dosing weight are more important than midazolam PK data for predicting PD response in the KNN model. Furthermore, some important factors such as patients' genotype, disease status, and other medication histories were not collected, and we were unable to include those covariables in our PD models. Future investigation should focus on further optimizing the models to increase the prediction performance (like recall rate) and explore the potential of the ML-based models in precision pharmacotherapy.

Chapter 6 Conclusions and Future Directions

The work presented in this thesis focuses on the PK/PD study in special populations with different pharmacometrics approaches, including PBPK modeling, population PK/PD modeling, and machine learning-based modeling. We have built a PBPK model to predict MPH exposure affected by the interplay among CES1 pharmacogenetics, DDIs, and sex. The study has led to a better understanding of the interindividual variability in MPH PK and PD. We developed an LC-MS/MS method for simultaneous quantification of targeted and untargeted metabolomes. This method was successfully applied to the MDZ population PK/PD study in neonates. Midazolam and metabolites exposure in neonates was well predicted by our 2-CMT population PK model. Furthermore, the MDZ concentration-response relationship was captured by the machine learning-based model.

The bottom-up PBPK approach is becoming the preferred methodology for neonate dosage prediction [144]. PBPK models for the neonatal population integrate the knowledge of the physiology, physiochemistry, biochemistry, ontogeny, and maturation of different systems to mathematically describe drug absorption, disposition, metabolism, and excretion (ADME) in neonates [145]. However, there are many obstacles hindering the use of PBPK modeling in neonates. For example, preterm neonates as a subpopulation are often discussed together with full-term neonates in PBPK studies, whilst studies indicate marked differences in physiology between preterm and term neonates [145]. The In Vitro In Vivo Extrapolation (IVIVE) of clearance in the pediatric population often fails due to the underestimation of non-CYP metabolic enzymes [146]. Moreover, ontogeny data on neonate transporters are often lacking,

which hinders the prediction of transporter expression at different ages [147]. In the future, various PBPK models will be developed for specific neonate subpopulations. To simulate the ontogeny of tissue, DMEs, and transporters in neonates, multi-omics data (e.g., proteomics and metabolomics) could be incorporated into our PBPK modeling. The genotypes and phenotypes of DMEs should also be studied to discover latent mutations associated with drug PK/PD.

Recently, plasma as a liquid biopsy surrogate for tissue biopsy has garnered increased interest[148]. Many studies have reported the use of circulating tumor cells (CTC) or circulating tumor DNA (ctDNA) in plasma or serum for numerous diagnostic applications [149]. Biomarkers obtained from serum/plasma samples can also help clinicians detect cancer early, stratify patients for the most suitable treatment, perform real-time monitoring of treatment response, study resistance mechanisms in the tumor, evaluate the risk for metastatic relapse, and estimate prognosis [149]. However, despite the great progress in identifying biomarkers for cancer diagnosis, studies using serum/plasma DMEs or other biomarkers to predict the drug ADME process in the body are limited. For future DME-mediated drug exposure/response studies, we could identify plasma ADME biomarkers and determine the correlations between the biomarkers and the metabolic activity in the body. Recently, our lab quantified CES1 protein concentrations in plasma samples collected during an MPH PK study [150] and revealed a significant inverse correlation between normalized plasma CES1 protein concentrations and the area under the concentration-time curves (AUCs) of plasma d-MPH ($P = 0.003$, $r = -0.703$), suggesting that plasma CES1 protein could explain ~ 50% of the variability in d-MPH AUCs. This strategy can be applied to study different hepatic DMEs and determine if their plasma concentrations could predict the metabolic function and the PK of their substrate drugs.

Extracellular vesicles (EVs) in the blood could be utilized for biomarker discovery. Four major types of extracellular vesicles constitute the “secretome”: exomeres, exosomes, microvesicles (e.g., ectosomes), and apoptotic bodies [151, 152]. They differ in size, protein signature, and mechanism of formation. Of these, exosomes are the most important for ADME research because they contain functional proteins and nucleic acids derived from the originating organs. Exosomes in peripheral blood contain ADME biomarkers which may reflect the functional state of the originating organ [153]. There are some promising results supporting the use of exosomes as potential ADME biomarkers: Rowland et al. [154] isolated plasma exosomes from patients with different CYP3A genotypes. They reported a good correlation between the exosomal CYP3A4 expression (mRNA and protein) and NADPH-dependent exosomal CYP3A4 activity. Another report focused on the correlation of intestinal miR-328 expression with the AUC of an orally-dosed BCRP substrate sulfasalazine. The investigators isolated GPA33-enriched plasma exosomes and found a better correlation with sulfasalazine plasma AUC than for the total plasma exosomes [155]. In future studies, we can use the proteomics technique to quantify the DMEs in exosomes, determine the correlation between exosomal and hepatic DMEs, and build models to simulate how the DME expression variability could alter the PK/PD of their substrates in various populations.

Bibliography

1. Srinivasan M, White A, Chaturvedula A, Vozmediano V, Schmidt S, Plouffe L, et al. Incorporating Pharmacometrics into Pharmacoeconomic Models: Applications from Drug Development. Pharmacoeconomics. 2020 Oct;38(10):1031-42.
2. Tylutki Z, Polak S, Wisniowska B. Top-down, Bottom-up and Middle-out Strategies for Drug Cardiac Safety Assessment via Modeling and Simulations. Curr Pharmacol Rep. 2016;2:171-7.
3. Xu C, Li CY, Kong AN. Induction of phase I, II and III drug metabolism/transport by xenobiotics. Arch Pharm Res. 2005 Mar;28(3):249-68.
4. Imai T, Taketani M, Shii M, Hosokawa M, Chiba K. Substrate specificity of carboxylesterase isozymes and their contribution to hydrolase activity in human liver and small intestine. Drug Metab Dispos. 2006 Oct;34(10):1734-41.
5. Her L, Zhu HJ. Carboxylesterase 1 and Precision Pharmacotherapy: Pharmacogenetics and Nongenetic Regulators. Drug Metab Dispos. 2020 Mar;48(3):230-44.
6. An G. The Utility of Pharmacometric Models in Clinical Pharmacology Research in Infants. Curr Pharmacol Rep. 2020 Oct;6(5):260-6.
7. Tayman C, Rayyan M, Allegaert K. Neonatal pharmacology: extensive interindividual variability despite limited size. J Pediatr Pharmacol Ther. 2011 Jul;16(3):170-84.
8. Rhodin MM, Anderson BJ, Peters AM, Coulthard MG, Wilkins B, Cole M, et al. Human renal function maturation: a quantitative description using weight and postmenstrual age. Pediatr Nephrol. 2009 Jan;24(1):67-76.
9. Kumar SS, Biltaji E, Bies R, Sherwin CM. The clinical utility of pharmacometric models. Br J Clin Pharmacol. 2018 Jul;84(7):1413-4.
10. Mahone EM, Denckla MB. Attention-Deficit/Hyperactivity Disorder: A Historical Neuropsychological Perspective. J Int Neuropsychol Soc. 2017 Oct;23(9-10):916-29.
11. Raz R, Gabis L. Essential fatty acids and attention-deficit-hyperactivity disorder: a systematic review. Dev Med Child Neurol. 2009 Aug;51(8):580-92.
12. Arnsten AFT, Rubia K. Neurobiological circuits regulating attention, cognitive control, motivation, and emotion: Disruptions in neurodevelopmental psychiatric disorders. Journal of the American Academy of Child and Adolescent Psychiatry. 2012;51(4):356--67.
13. Murnane KS, Howell LL. Neuroimaging and drug taking in primates. Psychopharmacology. 2011;216(2):153--71.
14. Favi. Phenobarbital, Midazolam Pharmacokinetics, Effectiveness, and Drug-Drug Interaction in Asphyxiated Neonates Undergoing Therapeutic Hypothermia. Neonatology. 2019;116(2):154--62.
15. Godfrey J. Safety of therapeutic methylphenidate in adults: a systematic review of the evidence. Journal of Psychopharmacology. 2008;23(2):194--205.
16. Kimko HC, Cross JT, Abernethy DR. Pharmacokinetics and clinical effectiveness of methylphenidate. Clinical Pharmacokinetics. 1999;37(6):457--70.

17. Patrick KS, Caldwell RW, Ferris RM, Breese GR. Pharmacology of the enantiomers of threo-methylphenidate. The Journal of pharmacology and experimental therapeutics. 1987;241(1):152--8.
18. Srinivas NR, Hubbard JW, Korchinski ED, Midha KK. Enantioselective pharmacokinetics of dl-threo-methylphenidate in humans. Pharmaceutical research. 1993;10(1):14--21.
19. Faraj BA, Israili ZH, Perel JM, Jenkins ML, Holtzman SG, Cucinell SA, et al. Metabolism and disposition of methylphenidate-14C: studies in man and animals. The Journal of pharmacology and experimental therapeutics. 1974;191(3):535--47.
20. Patrick KS, Straughn AB, Reeves OT, Bernstein H, Bell GH, Anderson ER, et al. Differential Influences of Ethanol on Early Exposure to Racemic Methylphenidate Compared with Dexmethylphenidate in Humans. 2013;1(January):197--205.
21. Zhu HJ, Patrick KS, Yuan HJ, Wang JS, Donovan JL, DeVane CL, et al. Two CES1 gene mutations lead to dysfunctional carboxylesterase 1 activity in man: clinical significance and molecular basis. Am J Hum Genet. 2008 Jun;82(6):1241-8.
22. Stage C, Jurgens G, Guski LS, Thomsen R, Bjerre D, Ferrero-Miliani L, et al. The impact of CES1 genotypes on the pharmacokinetics of methylphenidate in healthy Danish subjects. Br J Clin Pharmacol. 2017 Jul;83(7):1506-14.
23. Stangier J, Rathgen K, Sthle H, Gansser D, Roth W. The pharmacokinetics, pharmacodynamics and tolerability of dabigatran etexilate, a new oral direct thrombin inhibitor, in healthy male subjects. British Journal of Clinical Pharmacology. 2007;64(3):292--303.
24. Qian Y, Gilliland TK, Markowitz JS. The influence of carboxylesterase 1 polymorphism and cannabidiol on the hepatic metabolism of heroin. Chem Biol Interact. 2020 Jan 25;316:108914.
25. Zou LW, Jin Q, Wang DD, Qian QK, Hao DC, Ge GB, et al. Carboxylesterase Inhibitors: An Update. Curr Med Chem. 2018;25(14):1627-49.
26. Volkow ND, Swanson JM. Variables that affect the clinical use and abuse of methylphenidate in the treatment of ADHD. The American journal of psychiatry. 2003;160(11):1909--18.
27. Faraone SV, Biederman J, Wilens TE, Adamson J. A naturalistic study of the effects of pharmacotherapy on substance use disorders among ADHD adults. Psychological medicine. 2007;37(12):1743--52.
28. Shi J, Wang X, Nguyen J-H, Bleske BE, Liang Y, Liu L, et al. Dabigatran etexilate activation is affected by the CES1 genetic polymorphism G143E (rs71647871) and gender. Biochemical Pharmacology. 2016;119:76--84.
29. Patrick KS, Straughn AB, Minhinnett RR, Yeatts SD, Herrin AE, Devane CL, et al. Influence of Ethanol and Gender on Methylphenidate Pharmacokinetics and Pharmacodynamics. 2007;81(3).
30. Davis C, Levitan RD, Kaplan AS, Carter-Major JC, Kennedy JL. Sex differences in subjective and objective responses to a stimulant medication (methylphenidate): Comparisons between overweight/obese adults with and without binge-eating disorder. Int J Eat Disord. 2016 May;49(5):473-81.
31. Jones HM, Chen Y, Gibson C, Heimbach T, Parrott N, Peters SA, et al. Physiologically based pharmacokinetic modeling in drug discovery and development: a pharmaceutical industry perspective. Clinical pharmacology and therapeutics. 2015;97(3):247--62.

32. Hanke N, Frechen S, Moj D, Britz H, Eissing T, Wendl T, et al. PBPK Models for CYP3A4 and P-gp DDI Prediction: A Modeling Network of Rifampicin, Itraconazole, Clarithromycin, Midazolam, Alfentanil, and Digoxin. CPT: pharmacometrics \& systems pharmacology. 2018;7(10):647--59.
33. Wang X, Wang G, Shi J, Aa J, Comas R, Liang Y, et al. CES1 genetic variation affects the activation of angiotensin-converting enzyme inhibitors. Pharmacogenomics J. 2016 Jun;16(3):220-30.
34. Watanabe A, Fukami T, Takahashi S, Kobayashi Y, Nakagawa N, Nakajima M, et al. Arylacetamide deacetylase is a determinant enzyme for the difference in hydrolase activities of phenacetin and acetaminophen. Drug Metabolism and Disposition. 2010;38(9):1532--7.
35. Paterson SM, Moore GA, Florkowski CM, George PM. Determination of methylphenidate and its metabolite ritalinic acid in urine by liquid chromatography/tandem mass spectrometry. Journal of chromatography B, Analytical technologies in the biomedical and life sciences. 2012;881-882:20--6.
36. Willmann S, Hohn K, Edginton A, Sevestre M, Solodenko J, Weiss W, et al. Development of a physiology-based whole-body population model for assessing the influence of individual variability on the pharmacokinetics of drugs. J Pharmacokinet Pharmacodyn. 2007 Jun;34(3):401-31.
37. Yang X, Duan J, Fisher J. Application of physiologically based absorption modeling to characterize the pharmacokinetic profiles of oral extended release methylphenidate products in adults. PLoS ONE. 2016;11(10):1--28.
38. Kimko HC, Cross JT, Abernethy DR. Pharmacokinetics and clinical effectiveness of methylphenidate. Clin Pharmacokinet. 1999 Dec;37(6):457-70.
39. Golub M, Costa L, Crofton K, Frank D, Fried P, Gladen B, et al. NTP-CERHR Expert Panel Report on the reproductive and developmental toxicity of methylphenidate. Birth Defects Res B Dev Reprod Toxicol. 2005 Aug;74(4):300-81.
40. Sun Z, Murry DJ, Sanghani SP, Davis WI, Kedishvili NY, Zou Q, et al. Methylphenidate is stereoselectively hydrolyzed by human carboxylesterase CES1A1. Journal of Pharmacology and Experimental Therapeutics. 2004;310(2):469--76.
41. Wang X, He B, Shi J, Li Q, Zhu H-J. Comparative Proteomics Analysis of Human Liver Microsomes and S9 Fractions. Drug metabolism and disposition: the biological fate of chemicals. 2020;48(1):31--40.
42. Wilson ZE, Rostami-Hodjegan A, Burn JL, Tooley A, Boyle J, Ellis SW, et al. Inter-individual variability in levels of human microsomal protein and hepatocellularity per gram of liver. Br J Clin Pharmacol. 2003 Oct;56(4):433-40.
43. Yang X, Morris SM, Gearhart JM, Ruark CD, Paule MG, Slikker W, Jr., et al. Development of a physiologically based model to describe the pharmacokinetics of methylphenidate in juvenile and adult humans and nonhuman primates. PLoS One. 2014;9(9):e106101.
44. Berezhkovskiy LM. Volume of distribution at steady state for a linear pharmacokinetic system with peripheral elimination. Journal of pharmaceutical sciences. 2004;93(6):1628--40.
45. Davison JM, Dunlop W. Renal hemodynamics and tubular function normal human pregnancy. Kidney Int. 1980 Aug;18(2):152-61.
46. Hu Z-Y, Edginton AN, Laizure SC, Parker RB. Physiologically Based Pharmacokinetic Modeling of Impaired Carboxylesterase-1 Activity: Effects on Oseltamivir Disposition. Clinical Pharmacokinetics. 2014;53(9):825--36.

47. Parrott N, Davies B, Hoffmann G, Koerner A, Lave T, Prinssen E, et al. Development of a physiologically based model for oseltamivir and simulation of pharmacokinetics in neonates and infants. Clin Pharmacokinet. 2011 Sep;50(9):613-23.
48. Jones AW, Hahn RG, Stalberg HP. Distribution of ethanol and water between plasma and whole blood; inter- and intra-individual variations after administration of ethanol by intravenous infusion. Scand J Clin Lab Invest. 1990 Nov;50(7):775-80.
49. Umulis DM, Gurmen NM, Singh P, Fogler HS. A physiologically based model for ethanol and acetaldehyde metabolism in human beings. Alcohol. 2005 Jan;35(1):3-12.
50. Sager JE, Yu J, Ragueneau-Majlessi I, Isoherranen N. Physiologically Based Pharmacokinetic (PBPK) Modeling and Simulation Approaches: A Systematic Review of Published Models, Applications, and Model Verification. Drug Metab Dispos. 2015 Nov;43(11):1823-37.
51. Maharaj AR, Edginton AN. Physiologically based pharmacokinetic modeling and simulation in pediatric drug development. CPT Pharmacometrics Syst Pharmacol. 2014 Oct 22;3:e150.
52. Khalil F, Laer S. Physiologically based pharmacokinetic models in the prediction of oral drug exposure over the entire pediatric age range-sotalol as a model drug. AAPS J. 2014 Mar;16(2):226-39.
53. Lewis JP, Horenstein RB, Ryan K, O'Connell JR, Gibson Q, Mitchell BD, et al. The functional G143E variant of carboxylesterase 1 is associated with increased clopidogrel active metabolite levels and greater clopidogrel response. Pharmacogenet Genomics. 2013 Jan;23(1):1-8.
54. Suri A, Chapel S, Lu C, Venkatakrishnan K. Physiologically based and population PK modeling in optimizing drug development: A predict-learn-confirm analysis. Clin Pharmacol Ther. 2015 Sep;98(3):336-44.
55. Stage C, Dalhoff K, Rasmussen HB, Schow Guski L, Thomsen R, Bjerre D, et al. The impact of human CES1 genetic variation on enzyme activity assessed by ritalinic acid/methylphenidate ratios. Basic Clin Pharmacol Toxicol. 2019 Jul;125(1):54-61.
56. DeVane CL, Markowitz JS, Carson SW, Boulton DW, Gill HS, Nahas Z, et al. Single-dose pharmacokinetics of methylphenidate in CYP2D6 extensive and poor metabolizers. Journal of clinical psychopharmacology. 2000;20(3):347--9.
57. Laizure SC, Herring V, Hu Z, Witbrodt K, Parker RB. The role of human carboxylesterases in drug metabolism: have we overlooked their importance? Pharmacotherapy. 2013;33(2):210--22.
58. Soldin OP, Mattison DR. Sex differences in pharmacokinetics and pharmacodynamics. Clinical Pharmacokinetics. 2009;48(3):143--57.
59. Patrick KS, Straughn AB, Reeves OT, 3rd, Bernstein H, Bell GH, Anderson ER, et al. Differential influences of ethanol on early exposure to racemic methylphenidate compared with dexmethylphenidate in humans. Drug Metab Dispos. 2013 Jan;41(1):197-205.
60. Parker RB, Hu ZY, Meibohm B, Laizure SC. Effects of alcohol on human carboxylesterase drug metabolism. Clin Pharmacokinet. 2015 Jun;54(6):627-38.
61. Shellenberg TP, Stoops WW, Lile JA, Rush CR. An update on the clinical pharmacology of methylphenidate: therapeutic efficacy, abuse potential and future considerations. Expert Rev Clin Pharmacol. 2020 Aug;13(8):825-33.

62. Conklin HM, Lawford J, Jasper BW, Morris EB, Howard SC, Ogg SW, et al. Side effects of methylphenidate in childhood cancer survivors: a randomized placebo-controlled trial. Pediatrics. 2009 Jul;124(1):226-33.
63. Xiao J, Shi J, Thompson BR, Smith DE, Zhang T, Zhu HJ. Physiologically-based pharmacokinetic modeling to predict methylphenidate exposure affected by interplay among carboxylesterase 1 pharmacogenetics, drug-drug interactions, and sex. J Pharm Sci. 2022 May 5.
64. De Rose DU, Cairoli S, Dionisi M, Santisi A, Massenzi L, Goffredo BM, et al. Therapeutic Drug Monitoring Is a Feasible Tool to Personalize Drug Administration in Neonates Using New Techniques: An Overview on the Pharmacokinetics and Pharmacodynamics in Neonatal Age. Int J Mol Sci. 2020 Aug 17;21(16).
65. Jacqz-Aigrain E, Zhao W, Sharland M, van den Anker JN. Use of antibacterial agents in the neonate: 50 years of experience with vancomycin administration. Semin Fetal Neonatal Med. 2013 Feb;18(1):28-34.
66. de Hoog M, Mouton JW, van den Anker JN. Vancomycin: pharmacokinetics and administration regimens in neonates. Clin Pharmacokinet. 2004;43(7):417-40.
67. Mian P, Flint RB, Tibboel D, van den Anker JN, Allegaert K, Koch BCP. Therapeutic Drug Monitoring in Neonates: What Makes them Unique? Curr Pharm Des. 2017;23(38):5790-800.
68. Shao Y, Zhu B, Zheng R, Zhao X, Yin P, Lu X, et al. Development of urinary pseudotargeted LC-MS-based metabolomics method and its application in hepatocellular carcinoma biomarker discovery. J Proteome Res. 2015 Feb 6;14(2):906-16.
69. Lin W, Wang M, Chen M, Zheng X, Wu Y, Gao D, et al. Metabolomics and correlation network analyses of core biomarkers in type 2 diabetes. Amino acids. 2020.
70. Bagheri M, Willett W, Townsend MK, Kraft P, Ivey KL, Rimm EB, et al. A lipid-related metabolomic pattern of diet quality. The American journal of clinical nutrition. 2020.
71. Roemmelt AT, Steuer AE, Poetzsch M, Kraemer T. Liquid chromatography, in combination with a quadrupole time-of-flight instrument (LC QTOF), with sequential window acquisition of all theoretical fragment-ion spectra (SWATH) acquisition: systematic studies on its use for screenings in clinical and forensic toxicology and comparison with information-dependent acquisition (IDA). Anal Chem. 2014 Dec 2;86(23):11742-9.
72. Zha H, Cai Y, Yin Y, Wang Z, Li K, Zhu ZJ. SWATHtoMRM: Development of High-Coverage Targeted Metabolomics Method Using SWATH Technology for Biomarker Discovery. Analytical Chemistry. 2018;90(6):4062--70.
73. Song J, Wang X, Guo Y, Yang Y, Xu K, Wang T, et al. Novel high-coverage targeted metabolomics method (SWATHtoMRM) for exploring follicular fluid metabolome alterations in women with recurrent spontaneous abortion undergoing in vitro fertilization. Sci Rep. 2019 Jul 26;9(1):10873.
74. Bruderer T, Varesio E, Hidasi AO, Duchoslav E, Burton L, Bonner R, et al. Metabolomic spectral libraries for data-independent SWATH liquid chromatography mass spectrometry acquisition. Anal Bioanal Chem. 2018 Mar;410(7):1873-84.
75. Xiong Y, Shi C, Zhong F, Liu X, Yang P. LC-MS/MS and SWATH based serum metabolomics enables biomarker discovery in pancreatic cancer. Clin Chim Acta. 2020 Jul;506:214-21.
76. Drotleff B, Illison J, Schlotterbeck J, Lukowski R, Lammerhofer M. Comprehensive lipidomics of mouse plasma using class-specific surrogate calibrants and SWATH acquisition for large-scale lipid quantification in untargeted analysis. Anal Chim Acta. 2019 Dec 4;1086:90-102.

77. Raetz M, Duchoslav E, Bonner R, Hopfgartner G. Hybrid SWATH/MS and HR-SRM/MS acquisition for phospholipidomics using QUAL/QUANT data processing. Anal Bioanal Chem. 2019 Sep;411(22):5681-90.
78. Schlotterbeck J, Chatterjee M, Gawaz M, Lammerhofer M. Comprehensive MS/MS profiling by UHPLC-ESI-QTOF-MS/MS using SWATH data-independent acquisition for the study of platelet lipidomes in coronary artery disease. Anal Chim Acta. 2019 Jan 10;1046:1-15.
79. Tremoulet A, Le J, Poindexter B, Sullivan JE, Laughon M, Delmore P, et al. Characterization of the population pharmacokinetics of ampicillin in neonates using an opportunistic study design. Antimicrob Agents Chemother. 2014 Jun;58(6):3013-20.
80. Natarajan G, Botica ML, Thomas R, Aranda JV. Therapeutic drug monitoring for caffeine in preterm neonates: an unnecessary exercise? Pediatrics. 2007 May;119(5):936-40.
81. Momper JD, Capparelli EV, Wade KC, Kantak A, Dhanireddy R, Cummings JJ, et al. Population Pharmacokinetics of Fluconazole in Premature Infants with Birth Weights Less than 750 Grams. Antimicrob Agents Chemother. 2016 Sep;60(9):5539-45.
82. Mulla H, Lawson G, Peek GJ, Firmin RK, Upton DR. Plasma concentrations of midazolam in neonates receiving extracorporeal membrane oxygenation. ASAIO J. 2003 Jan-Feb;49(1):41-7.
83. Pacifici GM. Clinical pharmacology of midazolam in neonates and children: effect of disease-a review. Int J Pediatr. 2014;2014:309342.
84. Johnson TN, Rostami-Hodjegan A, Goddard JM, Tanner MS, Tucker GT. Contribution of midazolam and its 1-hydroxy metabolite to preoperative sedation in children: a pharmacokinetic-pharmacodynamic analysis. Br J Anaesth. 2002 Sep;89(3):428-37.
85. Tauzin M, Cohen R, Durrmeyer X, Dassieu G, Barre J, Caeymaex L. Continuous-Infusion Vancomycin in Neonates: Assessment of a Dosing Regimen and Therapeutic Proposal. Front Pediatr. 2019;7:188.
86. Adams KJ, Pratt B, Bose N, Dubois LG, St John-Williams L, Perrott KM, et al. Skyline for Small Molecules: A Unifying Software Package for Quantitative Metabolomics. J Proteome Res. 2020 Apr 3;19(4):1447-58.
87. Tsugawa H, Cajka T, Kind T, Ma Y, Higgins B, Ikeda K, et al. MS-DIAL: Data-independent MS/MS deconvolution for comprehensive metabolome analysis. Nature Methods. 2015;12(6):523--6.
88. Yu Z, Kastenmuller G, He Y, Belcredi P, Moller G, Prehn C, et al. Differences between human plasma and serum metabolite profiles. PLoS One. 2011;6(7):e21230.
89. Trabado S, Al-Salameh A, Croixmarie V, Masson P, Corruble E, Feve B, et al. The human plasma-metabolome: Reference values in 800 French healthy volunteers; impact of cholesterol, gender and age. PLoS One. 2017;12(3):e0173615.
90. Bian Y, Zheng R, Bayer FP, Wong C, Chang YC, Meng C, et al. Robust, reproducible and quantitative analysis of thousands of proteomes by micro-flow LC-MS/MS. Nat Commun. 2020 Jan 9;11(1):157.
91. Sarvin B, Lagziel S, Sarvin N, Mukha D, Kumar P, Aizenshtein E, et al. Fast and sensitive flow-injection mass spectrometry metabolomics by analyzing sample-specific ion distributions. Nat Commun. 2020 Jun 24;11(1):3186.
92. Cohen-Wolkowiez M, White NR, Bridges Aa. Development of a liquid chromatography-tandem mass spectrometry assay of six antimicrobials in plasma for pharmacokinetic studies in premature infants. Journal of chromatography B, Analytical technologies in the biomedical and life sciences. 2011;879(30):3497--506.

93. Zhang Y, Mehrotra N, Budha NR, Christensen ML, Meibohm B. A tandem mass spectrometry assay for the simultaneous determination of acetaminophen, caffeine, phenytoin, ranitidine, and theophylline in small volume pediatric plasma specimens. Clinica Chimica Acta. 2008;398(1-2):105--12.
94. Yin OQP, Lam SSL, Lo CMY, Chow MSS. Rapid determination of five probe drugs and their metabolites in human plasma and urine by liquid chromatography/tandem mass spectrometry: Application to cytochrome P450 phenotyping studies. Rapid Communications in Mass Spectrometry. 2004;18(23):2921--33.
95. Bijleveld Y, de Haan T, Toersche J, Jorjani S, van der Lee J, Groenendaal F, et al. A simple quantitative method analysing amikacin, gentamicin, and vancomycin levels in human newborn plasma using ion-pair liquid chromatography/tandem mass spectrometry and its applicability to a clinical study. J Chromatogr B Analyt Technol Biomed Life Sci. 2014 Mar 1;951-952:110-8.
96. Drotleff B, Hallschmid M, Lammerhofer M. Quantification of steroid hormones in plasma using a surrogate calibrant approach and UHPLC-ESI-QTOF-MS/MS with SWATH-acquisition combined with untargeted profiling. Anal Chim Acta. 2018 Aug 31;1022:70-80.
97. Sanwald C, Robciuc A, Ruokonen SK, Wiedmer SK, Lammerhofer M. A combined targeted/untargeted LC-MS/MS-based screening approach for mammalian cell lines treated with ionic liquids: Toxicity correlates with metabolic profile. Talanta. 2019 May 15;197:472-81.
98. Subhedar NV, Shaw NJ. Dopamine versus dobutamine for hypotensive preterm infants. Cochrane Database Syst Rev. 2003(3):CD001242.
99. Mannan MA, Shahidulla M, Salam F, Alam MS, Hossain MA, Hossain M. Postnatal development of renal function in preterm and term neonates. Mymensingh Med J. 2012 Jan;21(1):103-8.
100. Bueva A, Guignard JP. Renal function in preterm neonates. Pediatr Res. 1994 Nov;36(5):572-7.
101. Xiao J, Shi J, Li R, Her L, Wang X, Li J, et al. Developing a SWATH capillary LC-MS/MS method for simultaneous therapeutic drug monitoring and untargeted metabolomics analysis of neonatal plasma. J Chromatogr B Analyt Technol Biomed Life Sci. 2021 Aug 1;1179:122865.
102. Carter BS, Brunkhorst J. Neonatal pain management. Semin Perinatol. 2017 Mar;41(2):111-6.
103. Anderson BJ, Larsson P. A maturation model for midazolam clearance. Paediatr Anaesth. 2011 Mar;21(3):302-8.
104. de Wildt SN, Kearns GL, Hop WC, Murry DJ, Abdel-Rahman SM, van den Anker JN. Pharmacokinetics and metabolism of oral midazolam in preterm infants. Br J Clin Pharmacol. 2002 Apr;53(4):390-2.
105. Gorski JC, Hall SD, Jones DR, VandenBranden M, Wrighton SA. Regioselective biotransformation of midazolam by members of the human cytochrome P450 3A (CYP3A) subfamily. Biochem Pharmacol. 1994 Apr 29;47(9):1643-53.
106. Prommer E. Midazolam: an essential palliative care drug. Palliat Care Soc Pract. 2020;14:2632352419895527.
107. van Groen BD, Nicolai J, Kuik AC, Van Cruchten S, van Peer E, Smits A, et al. Ontogeny of Hepatic Transporters and Drug-Metabolizing Enzymes in Humans and in Nonclinical Species. Pharmacol Rev. 2021 Apr;73(2):597-678.

108. Tod M, Jullien V, Pons G. Facilitation of drug evaluation in children by population methods and modelling. Clin Pharmacokinet. 2008;47(4):231-43.
109. Linday L, Dobkin JF, Wang TC, Butler VP, Jr., Saha JR, Lindenbaum J. Digoxin inactivation by the gut flora in infancy and childhood. Pediatrics. 1987 Apr;79(4):544-8.
110. De Cock RF, Piana C, Krekels EH, Danhof M, Allegaert K, Knibbe CA. The role of population PK-PD modelling in paediatric clinical research. Eur J Clin Pharmacol. 2011 May;67 Suppl 1:5-16.
111. Mahler C, Schmidt A, Verveur D. [The application of hydrocolloids in genital skin care of pre-term infants]. Pflege. 2004 Dec;17(6):395-401.
112. Voller S, Flint RB, Beggah F, Reiss I, Andriessen P, Zimmermann LJI, et al. Recently Registered Midazolam Doses for Preterm Neonates Do Not Lead to Equal Exposure: A Population Pharmacokinetic Model. J Clin Pharmacol. 2019 Oct;59(10):1300-8.
113. de Wildt SN, de Hoog M, Vinks AA, Joosten KF, van Dijk M, van den Anker JN. Pharmacodynamics of midazolam in pediatric intensive care patients. Ther Drug Monit. 2005 Feb;27(1):98-102.
114. Jacqz-Aigrain E, Daoud P, Burtin P, Desplanques L, Beaufils F. Placebo-controlled trial of midazolam sedation in mechanically ventilated newborn babies. Lancet. 1994 Sep 3;344(8923):646-50.
115. van Groen BD, Vaes WH, Park BK, Krekels EHJ, van Duijn E, Korgvee LT, et al. Dose-linearity of the pharmacokinetics of an intravenous [(14) C]midazolam microdose in children. Br J Clin Pharmacol. 2019 Oct;85(10):2332-40.
116. Zuppa AF, Benitez GR, Zane NR, Curley MAQ, Bradfield J, Hakonarson H, et al. Morphine Dose Optimization in Critically Ill Pediatric Patients With Acute Respiratory Failure: A Population Pharmacokinetic-Pharmacogenomic Study. Crit Care Med. 2019 Jun;47(6):e485-e94.
117. Ahsman MJ, Hanekamp M, Wildschut ED, Tibboel D, Mathot RA. Population pharmacokinetics of midazolam and its metabolites during venoarterial extracorporeal membrane oxygenation in neonates. Clin Pharmacokinet. 2010 Jun;49(6):407-19.
118. Burtin P, Jacqz-Aigrain E, Girard P, Lenclen R, Magny JF, Betremieux P, et al. Population pharmacokinetics of midazolam in neonates. Clin Pharmacol Ther. 1994 Dec;56(6 Pt 1):615-25.
119. Lee TC, Charles BG, Harte GJ, Gray PH, Steer PA, Flenady VJ. Population pharmacokinetic modeling in very premature infants receiving midazolam during mechanical ventilation: midazolam neonatal pharmacokinetics. Anesthesiology. 1999 Feb;90(2):451-7.
120. Zhu B, Bush D, Doss GA, Vincent S, Franklin RB, Xu S. Characterization of 1'-hydroxymidazolam glucuronidation in human liver microsomes. Drug Metab Dispos. 2008 Feb;36(2):331-8.
121. Davenport T, Kalakota R. The potential for artificial intelligence in healthcare. Future Healthc J. 2019 Jun;6(2):94-8.
122. Cooper GF, Aliferis CF, Ambrosino R, Aronis J, Buchanan BG, Caruana R, et al. An evaluation of machine-learning methods for predicting pneumonia mortality. Artif Intell Med. 1997 Feb;9(2):107-38.
123. Ahmed Z, Mohamed K, Zeeshan S, Dong X. Artificial intelligence with multi-functional machine learning platform development for better healthcare and precision medicine. Database (Oxford). 2020 Jan 1;2020.

124. Peiffer-Smadja N, Rawson TM, Ahmad R, Buchard A, Georgiou P, Lescure FX, et al. Machine learning for clinical decision support in infectious diseases: a narrative review of current applications. Clin Microbiol Infect. 2020 May;26(5):584-95.
125. Adlung L, Cohen Y, Mor U, Elinav E. Machine learning in clinical decision making. Med-Cambridge. 2021 Jun 11;2(6):642-65.
126. Hu Q, Whitney HM, Giger ML. A deep learning methodology for improved breast cancer diagnosis using multiparametric MRI. Sci Rep. 2020 Jun 29;10(1):10536.
127. Lee SI, Celik S, Logsdon BA, Lundberg SM, Martins TJ, Oehler VG, et al. A machine learning approach to integrate big data for precision medicine in acute myeloid leukemia. Nat Commun. 2018 Jan 3;9(1):42.
128. Krittanawong C, Zhang H, Wang Z, Aydar M, Kitai T. Artificial Intelligence in Precision Cardiovascular Medicine. J Am Coll Cardiol. 2017 May 30;69(21):2657-64.
129. Zou H, Banerjee P, Leung SSY, Yan X. Application of Pharmacokinetic-Pharmacodynamic Modeling in Drug Delivery: Development and Challenges. Front Pharmacol. 2020;11:997.
130. McComb M, Bies R, Ramanathan M. Machine learning in pharmacometrics: Opportunities and challenges. Br J Clin Pharmacol. 2022 Feb;88(4):1482-99.
131. Chaturvedula A, Calad-Thomson S, Liu C, Sale M, Gattu N, Goyal N. Artificial Intelligence and Pharmacometrics: Time to Embrace, Capitalize, and Advance? CPT Pharmacometrics Syst Pharmacol. 2019 Jul;8(7):440-3.
132. Qian T, Zhu S, Hoshida Y. Use of big data in drug development for precision medicine: an update. Expert Rev Precis Med Drug Dev. 2019;4(3):189-200.
133. Brier ME, Zurada JM, Aronoff GR. Neural network predicted peak and trough gentamicin concentrations. Pharm Res. 1995 Mar;12(3):406-12.
134. Chow HH, Tolle KM, Roe DJ, Elsberry V, Chen H. Application of neural networks to population pharmacokinetic data analysis. J Pharm Sci. 1997 Jul;86(7):840-5.
135. Yamamura S, Kawada K, Takehira R, Nishizawa K, Katayama S, Hirano M, et al. Artificial neural network modeling to predict the plasma concentration of aminoglycosides in burn patients. Biomed Pharmacother. 2004 May;58(4):239-44.
136. Tang J, Liu R, Zhang YL, Liu MZ, Hu YF, Shao MJ, et al. Application of Machine-Learning Models to Predict Tacrolimus Stable Dose in Renal Transplant Recipients. Sci Rep. 2017 Feb 8;7:42192.
137. Vamathevan J, Clark D, Czodrowski P, Dunham I, Ferran E, Lee G, et al. Applications of machine learning in drug discovery and development. Nat Rev Drug Discov. 2019 Jun;18(6):463-77.
138. Poynton MR, Choi BM, Kim YM, Park IS, Noh GJ, Hong SO, et al. Machine learning methods applied to pharmacokinetic modelling of remifentanil in healthy volunteers: a multi-method comparison. J Int Med Res. 2009 Nov-Dec;37(6):1680-91.
139. Hummel P, Puchalski M, Creech SD, Weiss MG. Clinical reliability and validity of the N-PASS: neonatal pain, agitation and sedation scale with prolonged pain. J Perinatol. 2008 Jan;28(1):55-60.
140. Liu Z, Yao L, Wang X, Monaghan JJM, Schaette R, He Z, et al. Generalizable Sample-Efficient Siamese Autoencoder for Tinnitus Diagnosis in Listeners With Subjective Tinnitus. IEEE Trans Neural Syst Rehabil Eng. 2021;29:1452-61.
141. Harden M, Friede T. Sample size calculation in multi-centre clinical trials. BMC Med Res Methodol. 2018 Nov 29;18(1):156.

142. Bailly S, Gautier-Veyret E, Le MP, Bouadma L, Andremont O, Neuville M, et al. Impact of Loading Dose of Caspofungin in Pharmacokinetic-Pharmacodynamic Target Attainment for Severe Candidiasis Infections in Patients in Intensive Care Units: the CASPOLOAD Study. Antimicrob Agents Chemother. 2020 Nov 17;64(12).
143. Leo J, Luhanga E, Michael K. Machine Learning Model for Imbalanced Cholera Dataset in Tanzania. ScientificWorldJournal. 2019;2019:9397578.
144. Mahmood I. Dosing in children: a critical review of the pharmacokinetic allometric scaling and modelling approaches in paediatric drug development and clinical settings. Clin Pharmacokinet. 2014 Apr;53(4):327-46.
145. Michelet R, Bocxlaer JV, Vermeulen A. PBPK in Preterm and Term Neonates: A Review. Curr Pharm Des. 2017;23(38):5943-54.
146. Anderson BJ, Allegaert K, Holford NH. Population clinical pharmacology of children: general principles. Eur J Pediatr. 2006 Nov;165(11):741-6.
147. Souza A, Jr., Santos D, Fonseca S, Medeiros M, Batista L, Turner M, et al. Toxic excipients in medications for neonates in Brazil. Eur J Pediatr. 2014 Jul;173(7):935-45.
148. Chu D, Park BH. Liquid biopsy: unlocking the potentials of cell-free DNA. Virchows Arch. 2017 Aug;471(2):147-54.
149. Wang J, Chang S, Li G, Sun Y. Application of liquid biopsy in precision medicine: opportunities and challenges. Front Med. 2017 Dec;11(4):522-7.
150. Shi J, Xiao J, Wang X, Jung SM, Bleske BE, Markowitz JS, et al. Plasma Carboxylesterase 1 Predicts Methylphenidate Exposure: A Proof-of-Concept Study Using Plasma Protein Biomarker for Hepatic Drug Metabolism. Clin Pharmacol Ther. 2022 Apr;111(4):878-85.
151. Zijlstra A, Di Vizio D. Size matters in nanoscale communication. Nat Cell Biol. 2018 Mar;20(3):228-30.
152. Zhang H, Freitas D, Kim HS, Fabijanic K, Li Z, Chen H, et al. Identification of distinct nanoparticles and subsets of extracellular vesicles by asymmetric flow field-flow fractionation. Nat Cell Biol. 2018 Mar;20(3):332-43.
153. Rodrigues D, Rowland A. From Endogenous Compounds as Biomarkers to Plasma-Derived Nanovesicles as Liquid Biopsy; Has the Golden Age of Translational Pharmacokinetics-Absorption, Distribution, Metabolism, Excretion-Drug-Drug Interaction Science Finally Arrived? Clin Pharmacol Ther. 2019 Jun;105(6):1407-20.
154. Rowland A, Ruanglertboon W, van Dyk M, Wijayakumara D, Wood LS, Meech R, et al. Plasma extracellular nanovesicle (exosome)-derived biomarkers for drug metabolism pathways: a novel approach to characterize variability in drug exposure. Br J Clin Pharmacol. 2019 Jan;85(1):216-26.
155. Gotanda K, Hirota T, Saito J, Fukae M, Egashira Y, Izumi N, et al. Circulating intestine-derived exosomal miR-328 in plasma, a possible biomarker for estimating BCRP function in the human intestines. Sci Rep. 2016 Aug 30;6:32299.